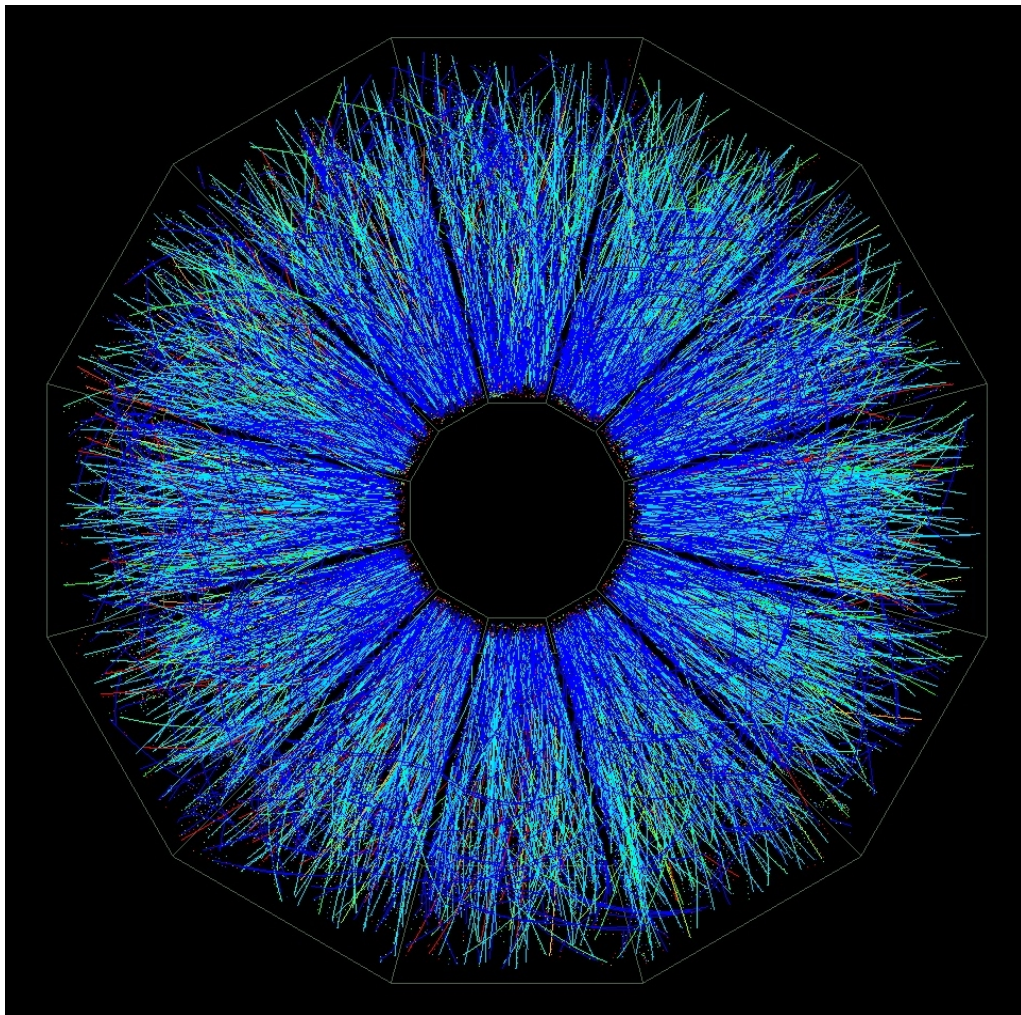


RHIC Beam Use Request For Runs 17 and 18

The STAR Collaboration



May 26, 2016

1 Executive Summary

In this Beam Use Request the STAR Collaboration presents four compelling and prioritized scientific programs for the 2017 and 2018 RHIC runs.

STAR's **highest scientific priority** is the first significant measurement of the sign change of the Sivers function, as compared to the value measured in semi-inclusive deep inelastic scattering experiments, through measurements of single spin asymmetries in $W^{+/-}$, Z, direct photon and Drell-Yan production in transversely polarized $\sqrt{s} = 500$ GeV p+p collisions. This measurement will also shed light on the size and nature of the evolution of these transverse momentum dependent distributions. The sign change measurement is a fundamental test of QCD and is being pursued by other experiments, making a timely measurement imperative. We therefore request **13 weeks of 500 GeV p+p running in Run17**.

STAR's **second scientific priority** is to clarify the interpretation of measurements related to the chiral magnetic effect, chiral magnetic wave and chiral vortical effect. We therefore request **two 3.5 week runs in Run 18** with collisions of isobaric nuclei, Ruthenium-96 (Ru+Ru) and Zirconium-96 (Zr+Zr). Ru nuclei have an atomic charge of 44 compared to 40 for Zr. Ru+Ru collisions will therefore generate a magnetic field approximately 10% larger than Zr+Zr collisions while all else remains virtually fixed. Comparisons of charge separation in Ru+Ru and Zr+Zr collisions will isolate the magnetic field dependence of the observed charge separation thereby determining what fraction of those measurements are related to the chiral magnetic effect. These results will greatly advance our understanding of the chiral magnetic effect and have fundamental impact beyond the field of high-temperature QCD.

Our **next scientific priorities** involve taking data at two beam energies that are lower than the nominal energies, but are not part of STAR's proposed Beam-Energy-Scan Phase-II (BES-II) program in 2019-2020 [1].

The first of these requests is driven by theoretical calculations suggesting that the partonic coupling to the medium is stronger when temperatures are close to the critical value. Results from Run 10 at 62.4 GeV provide tantalizing evidence that this is true, but the data are statistically limited. We therefore request a **4 weeks 62.4 GeV Au+Au run in Run 17** to significantly enhance the statistical precision of these results. Precise measurements of non-photonic electron v_2 will confirm that this enhanced coupling results in the partial thermalization of charmed quarks even at this low energy, while our semi-inclusive recoil jet studies will probe possible differences in the jet energy redistribution. Finally, measurements of direct (virtual) photons will improve our understanding of thermal photon production and their medium coupling.

The second request is derived from STAR's recent report of the observation of the *global* polarization of hyperons (GPH) in non-central Au+Au collisions at energies below 40GeV. This is the first direct probe of the plasma vorticity, a fundamental characteristic of any fluid that must be quantified in order to understand the physics in detail. It also provides a measure of the magnetic field present over the evolution of the QGP. In addition to being of fundamental interest on their own accounts, these measurements provide critical context for recent high-profile studies of exotic phenomenon. In particular, the Chiral Vortical Effect (CVE) and Chiral Magnetic Effect (CME) are among the RHIC program's most exciting and visible topics today. However, they are

nontrivial and require several conditions to be simultaneously met; “extraordinary claims require extraordinary evidence.” GPH has nothing “chiral” or exotic about it. In a theoretically well-grounded way, it measures the average vorticity (ω) and field (B). Hence, GPH must be understood first, to put more “extraordinary” claims on firmer ground. A solid understanding of GPH and the magnetic field, however, requires the increased statistics available with a 2-week run at 27 GeV. While similar high-statistics measurements of GPH will eventually be performed in BES-II, the scientific impact of getting firm measures of vorticity and B much sooner is high, given the current intensity of research and attention on CME and CVE.

Table 1.1 and Table 1.2 summarize the above requests, along with our scientific priorities and proposed running sequence. We have considered two scenarios:

Scenario 1: 19 cryo-weeks for Run 17 and 13 cryo-weeks for Run 18 (Table 1-1)

Scenario 2: 24 cryo-weeks for Run 17 and 13 cryo-weeks for Run 18 (Table 1-2)

In this document we first present highlights from papers published since the last PAC meeting and on-going analyses. Next we summarize the analysis status of data from STAR’s two recent upgrades, the Heavy Flavor Tracker (HFT) and the Muon Telescope Detector (MTD), and discuss the detector’s performance in Run 16. In Sections 4 and 5, we detail the STAR Collaboration’s compelling physics program driving our Run 17 and Run 18 beam-use request. Collection of these data will allow us to achieve our spin and relativistic heavy ion physics goals on a timescale consistent with the current intense international interest while utilizing RHIC beams effectively and taking full advantage of recent improvements in machine and detector capability. Finally, we outline the planned upgrades for Run 17 and 18 and the BES-II.

Run	Energy	Duration	System	Goals	priority	Seq
17	$\sqrt{s_{NN}}=500$ GeV	13-wk	Transverse p+p	A_N of W^\pm, γ , Drell-Yan, $\mathcal{L}=360$ pb $^{-1}$, 55% pol RHICf	1	1
		1-wk	p+p			2
		2-wk	CeC			
18	$\sqrt{s_{NN}}=200$ GeV	3.5-wk	Ru+Ru	1.2B MB	2	3
	$\sqrt{s_{NN}}=200$ GeV	3.5-wk	Zr+Zr	1.2B MB	2	4
	$\sqrt{s_{NN}}=27$ GeV	2-wk	Au+Au	500M MB	3	5

Table 1.1: Scenario I: 19 cryo-weeks for Run 17 and 13 cryo-weeks for Run 18. All luminosities requested are actual sampled luminosity. See text for details about pp500 run conditions and optimizations.

Run	Energy	Duration	System	Goals	priority	Seq
17	$\sqrt{s_{NN}}=500$ GeV	13-wk	Transverse p+p	A_N of W^\pm , γ , Drell-Yan, $\mathcal{L}=360$ pb $^{-1}$, 55% pol RHICf	1	1
		1-wk	p+p			2
		2-wk	CeC			
	$\sqrt{s_{NN}}=62.4$ GeV	4-wk	Au+Au	Jets, dileptons, NPE 1.5B MB	5	3
18	$\sqrt{s_{NN}}=200$ GeV	3.5-wk	Ru+Ru	1.2B MB	2	4
	$\sqrt{s_{NN}}=200$ GeV	3.5-wk	Zr+Zr	1.2B MB	2	5
	$\sqrt{s_{NN}}=27$ GeV	2-wk	Au+Au	500M MB	5	6

Table 1.2: Scenario 2: 24 cryo-weeks for Run 17 and 13 cryo-weeks for Run 18

1	EXECUTIVE SUMMARY	3
2	HIGHLIGHTS FROM STAR SCIENCE PROGRAMS	8
2.1	STAR HEAVY ION PROGRAM	8
2.1.1	HEAVY FLAVOR AND QUARKONIA	8
2.1.2	JET MODIFICATION IN THE MEDIUM	9
2.1.3	DILEPTONS AS A PROBE OF CHIRAL RESTORATION	10
2.1.4	HIGH P_T HADRON SUPPRESSION	12
2.1.5	FLOW AND FLUCTUATIONS	13
2.1.6	LAMBDA POLARIZATION	16
2.2	STAR SPIN PROGRAM	19
2.2.1	TRANSVERSE SPIN PROGRAM	19
2.2.2	LONGITUDINAL SPIN PROGRAM	21
2.3	REVIEW OF THE CHIRAL MAGNETIC /VORTICAL EFFECTS	23
2.3.1	CHIRAL MAGNETIC EFFECT	23
2.3.2	CHIRAL MAGNETIC WAVE	26
2.3.3	CHIRAL VORTICAL EFFECT	27
2.4	PROGRESS ON PHYSICS ANALYSES WITH THE HEAVY FLAVOR TRACKER	28
2.5	PROGRESS ON PHYSICS ANALYSES WITH THE MUON TELESCOPE DETECTOR	32
2.5.1	J/ψ PRODUCTION IN P+P AT 500 GeV	32
2.5.2	J/ψ PRODUCTION AND Υ STATES RATIOS IN AU+AU COLLISIONS AT 200 GeV	33
3	RUN 16 PERFORMANCE REPORT	37
3.1	THE HFT DATA PERFORMANCE AND PROJECTIONS	37
3.2	THE MTD DATA PERFORMANCE AND PROJECTIONS	38
4	RUN 17 REQUEST	40
4.1	POLARIZED P+P AT $\sqrt{s} = 500$ GeV	40
4.2	THE SIVERS FUNCTION	40
4.2.1	THE EFREMOV-TERYAEV-QIU-STERMAN FUNCTION	45
4.3	INTERFERENCE FRAGMENTATION, COLLINS, COLLINS-LIKE AND SIVERS FUNCTIONS	46
4.4	USING ULTRA PERIPHERAL COLLISIONS TO ACCESS THE GENERALIZED PARTON DISTRIBUTION FUNCTION, E_g:	48
4.5	GLUON FRAGMENTATION FUNCTIONS	49
4.6	PRECISE MEASUREMENT OF THE W-BOSON CROSS-SECTION RATIO	51
4.7	CENTRAL EXCLUSIVE PROCESS IN DIFFRACTIVE P+P VIA DOUBLE POMERON EXCHANGE	52
4.8	HEAVY FLAVOR CROSS-SECTION MEASUREMENTS IN $\sqrt{s} = 500$ GeV P+P COLLISIONS	55
4.9	AU+AU COLLISIONS AT 62.4 GeV	56
4.9.1	NON-PHOTONIC ELECTRON ELLIPTIC FLOW AND HIGH P_T SUPPRESSION	58
4.9.2	JET ENERGY LOSS MEASUREMENTS	59
4.9.3	DILEPTON AND DIRECT VIRTUAL PHOTON MEASUREMENTS	61
5	RUN 18 REQUEST	63
5.1	ISOBAR COLLISIONS (ZR+ZR, RU+RU) AT 200GeV	63
5.1.1	INITIAL MAGNETIC FIELD DEPENDENCE OF CHARGE SEPARATION	63
5.1.2	DILEPTON PRODUCTION IN ISOBARIC COLLISIONS	68
5.1.3	DI-ELECTRON MEASUREMENTS IN RU+RU AND ZR+ZR COLLISIONS	69
5.2	AU+AU COLLISIONS AT 27GeV	71

5.2.1	GLOBAL POLARIZATION MEASUREMENTS AT 27GeV	71
5.2.2	DILEPTON MEASUREMENTS AT 27 GeV	71
6	<u>CALIBRATION AND PRODUCTION PROJECTIONS FOR RUN 17 AND 18 REQUESTS</u>	73
7	<u>DETECTOR UPGRADES FOR RUN-17</u>	74
7.1	UPGRADES CRITICAL TO MEASURE DRELL-YAN A_N	74
7.1.1	PRESHOWER (FPS) PERFORMANCE IN RUN-15	74
7.1.2	A POSTSHOWER (FPOST) FOR THE FMS IN RUN 17	77
	POSTSHOWER DESIGN DETAILS:	79
7.1.3	FMS PERFORMANCE IN RUN15 AND FURTHER UPGRADES FOR RUN17	80
7.2	UPGRADES CRITICAL TO BES-II	82
7.2.1	STAR INNER TPC SECTOR UPGRADE (ITPC)	82
7.2.2	EVENT PLANE DETECTOR	83
7.2.3	ENDCAP TOF (CBM TOF)	84
8	<u>REFERENCES</u>	85

2 Highlights from STAR Science Programs

Since the last Beam Use Request and PAC meeting in June of 2015, STAR has published 17 scientific papers: Nature (1), Physics Review Letters (7), Physics Letters B (4) and others (5). We have also submitted 13 new papers for publication. Many new topics and preliminary results, including data from run 14 (Au+Au at 14.5 and 200GeV) and run 15 (p+p and p+Au collisions), have been presented at recent major conferences in the field: DIS2015, DIS2016, HP2015 and QM2015.

2.1 STAR Heavy Ion Program

2.1.1 Heavy Flavor and Quarkonia

STAR has launched a comprehensive heavy-flavor program with the two newly installed novel detectors: the Heavy-Flavor Tracker (HFT) for open heavy-flavor measurements and the Muon Telescope Detector (MTD) for quarkonia measurements. While data taken with these systems in Run 14 has already produced several high-impact preliminary results, STAR continues to successfully run, accumulate additional data and anticipate exciting new results from these detectors. Two progress reports from those upgrades and physics analyses are presented in sections 2.4 and 0. The reports show preliminary results since the last PAC meeting on $D^0 v_2$ and the nuclear modification factor, reconstructions of $D^\pm \rightarrow K^\mp \pi^\pm \pi^\pm$ and $D_s^\pm \rightarrow \phi (\rightarrow K^+ K^-) \pi^\pm$ channels from Run 14 data with the HFT, J/ψ production and its dependence on event activity, and Upsilon production through the dimuon decay channel from Run 14 and Run 15 data with the MTD.

There are several J/ψ production models (eg: Color Octet Model, Color Evaporation Model, Non- Relativistic QCD) that correctly describe the production yields in elementary particle collisions. However, the actual production mechanism is still unknown. STAR continues to carry out differential measurements to help distinguish between these models [2]. While many models can describe relatively well the experimental data on the J/ψ cross-section in p+p collisions, they have different predictions for the J/ψ polarization. Therefore, measurements of the J/ψ polarization allow for discrimination between different theories and provide unique insight into the J/ψ production mechanism. In general, NNLO* QCD predicts large negative [3] λ_θ while Lower-order QCD and NRQCD predict a positive value [4]. Figure 2-1 shows the J/ψ polarization parameter, λ_θ , as a function of $x_T = 2p_T/\sqrt{s}$ in the helicity frame at different collision energies. A trend towards strong negative values with increasing x_T values is observed.

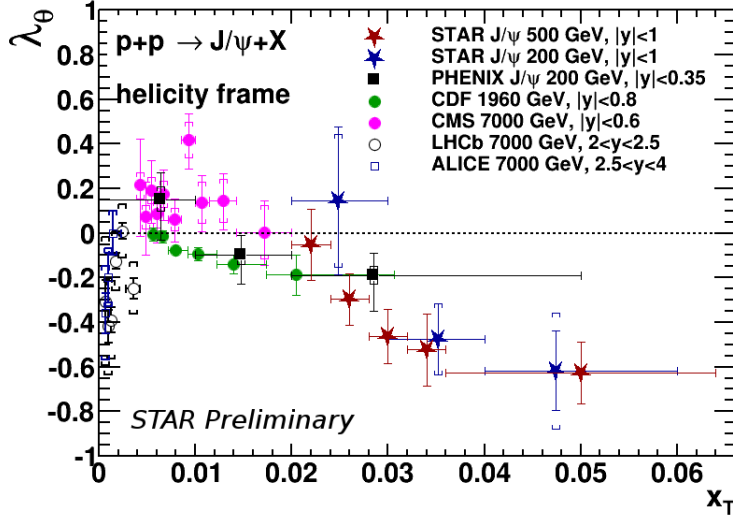


Figure 2-1 J/ψ polarization parameter in the helicity frame as a function of x_T .

2.1.2 Jet Modification in the Medium

Fully reconstructed jets are one of the main tools to constrain the medium transport parameters and it is therefore an active area of research for current and planned future experiments. Full jet reconstruction in Au+Au collisions at $\sqrt{s_{NN}} = 200$ GeV have been carried out at STAR using the anti- k_T algorithm ($R = 0.2$ to 0.5) with a low IR-cutoff ($p_T > 0.2$ GeV/c). To address the challenge posed by the large soft and inhomogeneous underlying event background in measuring jet yields STAR measures the semi-inclusive distributions of reconstructed charged particle jets recoiling from a high p_T trigger hadron

$$\frac{1}{N_{trig}^h} \frac{dN_{jet}}{dp_{T,jet}} = \frac{1}{\sigma^{AA \rightarrow h+X}} \frac{d\sigma^{AA \rightarrow h+jet+X}}{dp_{T,jet}}$$

where $\sigma^{AA \rightarrow h+X}$ is the cross-section to generate a trigger hadron, and $d\sigma^{AA \rightarrow h+jet+X}/dp_{T,jet}$ is the cross-section for coincidence production of a trigger hadron and a recoil jet. A mixed-event technique has been developed and used to treat the uncorrelated background. Figure 2-2 upper panels, show the fully corrected semi-inclusive recoil jet distributions for central and peripheral events after unfolding p_T -smearing and instrumental effects. Results for cone radii $R = 0.3$ and 0.5 are shown for $9.0 < p_{T,trig} < 30.0$ GeV/c. The ratios of recoil jet distributions in central to that in peripheral collisions, I_{CP} , in lower panels show a clear suppression of yields in central events for $p_{T,jet}^{ch} > 10$ GeV/c for both cone radii. Here $p_{T,jet}^{ch}$ is the transverse momentum of jets reconstructed from only charged particles. The horizontal shifts in the range where the I_{CP} is flat ($10 < p_{T,jet}^{ch} < 20$) are $-6.3 \pm 0.6 \pm 0.8$ GeV/c and $-3.8 \pm 0.5 \pm 1.8$ GeV/c for $R = 0.3$ and $R = 0.5$, respectively. The suppression and shift, and their

reduction for larger cones might indicate an out-of-cone energy transport. An open question is whether the medium is effectively continuous or composed of quasi-particles at these Q^2 . For this, STAR has also studied the azimuthal distribution of jet axes with respect to the recoil trigger hadron in search for evidence of large angle scattering, Molière scattering, whose presence would indicate hard scattering off quasi-particles. The study shows so far no evidence of Molière scattering with the current statistical precision.

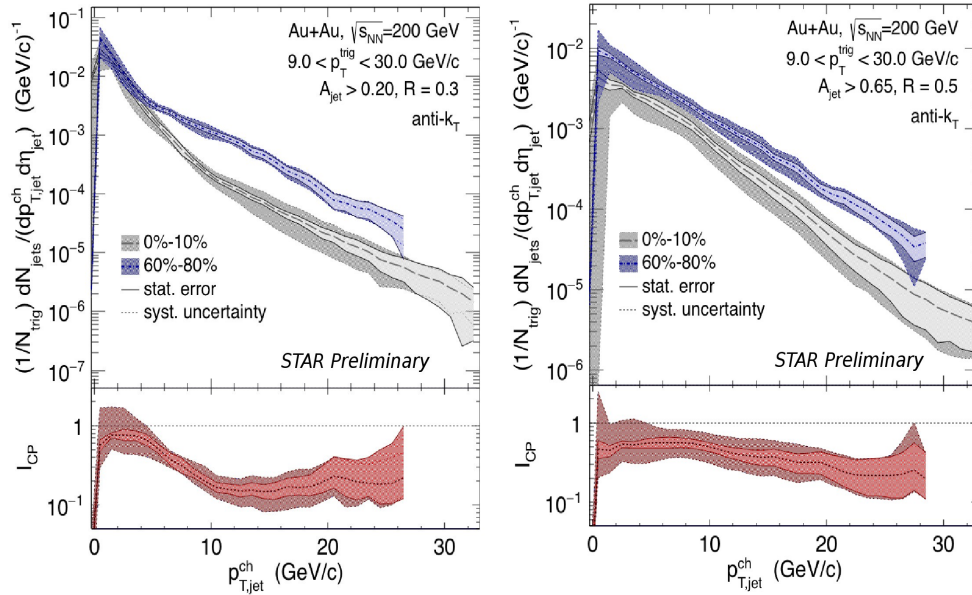


Figure 2-2 (Upper panels) Corrected recoil jet distributions for peripheral and central collisions (Lower panels) I_{CP} , the ratio of central to peripheral yields. (Left) Cone size $R = 0.3$. (Right) Cone size $R = 0.5$.

2.1.3 Dileptons as a Probe of Chiral Restoration

Dileptons are crucial probes for studying the properties of the strongly interacting, hot and dense matter, which is created in ultra-relativistic heavy-ion collisions at the Relativistic Heavy-Ion Collider (RHIC). STAR has continued to explore how dilepton measurements can be used as a sensitive probe of chiral symmetry restoration effects. STAR has been very fruitful in presenting and publishing the dilepton results in the last two years. The excess in the yields of di-leptons at low mass ($M_{ll} < 1 \text{ GeV}/c^2$) has been long linked to chiral dynamics in heavy-ion collisions. STAR has recently published its acceptance-corrected measurement of di-electron (e^+e^- pairs), production in Au+Au collisions at $\sqrt{s_{NN}} = 200$ and 19.6 GeV. New measurements of di-electron production in U+U at $\sqrt{s_{NN}} = 193$ GeV, a system with an expected 20% increase in energy density and consequently a longer lifetime, have been presented at Quark Matter 2015 [5]. Figure 2-3 left shows the acceptance-corrected excess di-electron invariant-mass spectra normalized by dN_{ch}/dy in minimum-bias Au+Au collisions at $\sqrt{s_{NN}} = 27, 39, 62.4$ and 200 GeV and U+U collisions at $\sqrt{s_{NN}} = 193$ GeV.

Models with collisional broadening of ρ -mesons describe the data across all energies, centralities, and p_T . Figure 2–3 right shows the integrated di-electron excess yields ($0.4 < M_{ll} < 0.75 \text{ GeV}/c^2$) normalized by and as function of dN_{ch}/dy . The yields show an increasing trend from peripheral to central collisions and from lower to higher energies, which is predicted to be the case if the emission is correlated with the medium lifetime. The measurements are also compared to theoretical calculations of medium lifetime.

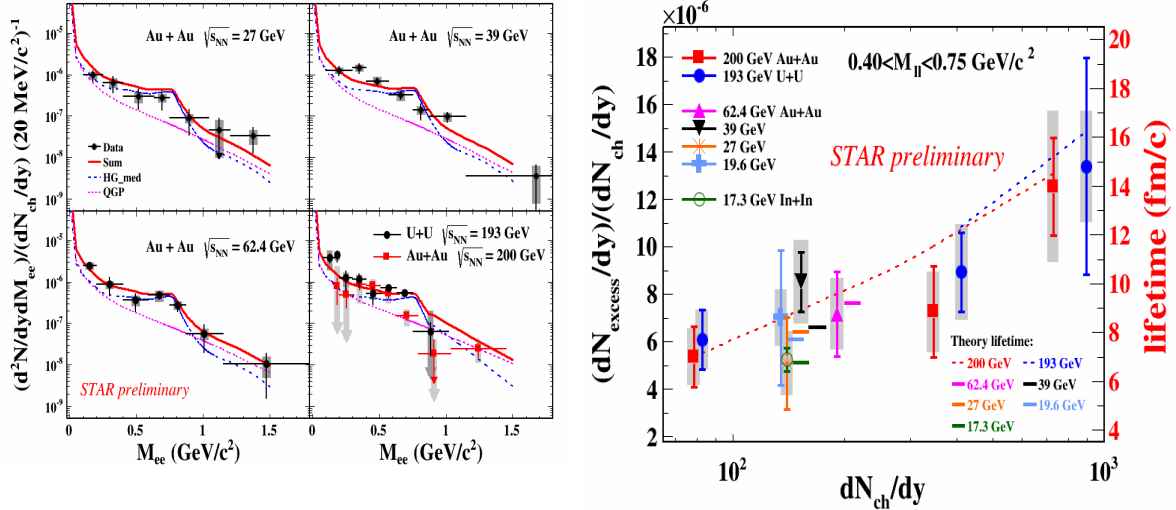


Figure 2–3 (Left) Acceptance-corrected di-electron excess invariant-mass spectra normalized by dN_{ch}/dy in minimum-bias Au+Au collisions at $\sqrt{s_{NN}} = 27$; 39; 62.4 and 200 GeV and U+U collisions at $\sqrt{s_{NN}} = 193$ GeV. Model calculations (red solid curves) with a broadened ρ spectral function, which is the sum of QGP radiation contribution and in hadronic medium broadening are shown. (Right) Integrated di-electron excess invariant-mass spectra ($0.4 < M_{ll} < 0.75 \text{ GeV}/c^2$) normalized by dN_{ch}/dy in different collision species and at different collision energies compared to the theoretical calculations of the fireball lifetimes.

In the energy range from 27 GeV up to 200 GeV, shown in the left panel of Fig. 2-3, the total baryon density remains fairly constant. For collision energies below 27 GeV the total baryon density will increase with decreasing collision energy. Model descriptions so far have been able to successfully describe the low-mass dielectron production for the energy range in which this baryon density remains constant. The same model descriptions expect that the low-mass production will scale with the total baryon density. While the first phase of the Beam Energy Scan provided for collision data below 19.6 GeV, the collected statistics have been too low to allow for meaningful results from dielectron measurements. However, in the context of the proposed BES-II, the collaboration will collect sufficient statistics to provide a meaningful extension of its low-mass measurements into the full BES energy range. Moreover, the proposed integral luminosities will allow for dielectron measurements in the intermediate mass range of $M_\phi < M_{ee} < M_{J/\psi}$. This invariant mass range is expected to offer a direct window to direct temperature measurements of the QCD medium and thus providing a complimentary picture of the evolution of the system towards lower center-of-mass energies.

The upcoming Runs 17 and 18 will see a significant reduction in the material budget by the removal of the HFT and reinstallation of the old beam pipe leading to an effective improvement of the signal-to-background ratio. The proposed integral luminosity would not only improve the existing uncertainties in the low mass range, but more importantly, would provide a first opportunity to do a statistically meaningful measurement in the intermediate range. We present in 4.9.3 and 5.2.2 the case for measurements at center-of-mass energies of $\sqrt{s_{NN}} = 27$ and 62.4 GeV.

2.1.4 High p_T Hadron Suppression

High- p_T hadron suppression is considered to be a key evidence of the formation of sQGP in heavy-ion collisions. It is only natural to study this observable in the BES to look for the onset energy at which the strong suppression starts to appear.

Figure 2–4 left shows the charged hadron R_{CP} at different BES-I energies. R_{CP} exhibits a smooth transition from strong suppression at high energies to enhancement at lower beam energies. It is well known, however, that the so-called Cronin Effect, which gives rise to an enhanced high p_T production, is more prominent at lower beam energies. This competing effect complicates the interpretation of this observation. The d+Au data from the current run may start to untangle the cold nuclear matter (CNM) enhancement and QGP suppression effects. The enhancement and suppression effects are proportional to centrality, so a study of the centrality dependence of the charged hadron yields is expected to bring insight into the interplay of these effects.

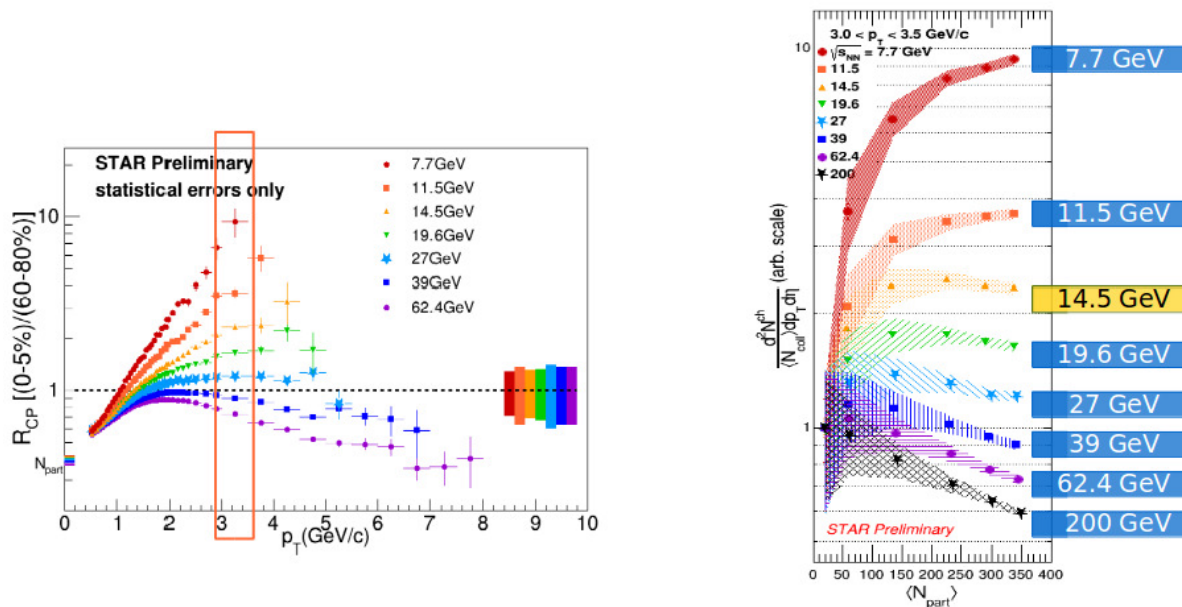


Figure 2–4 (Left) Charged hadron R_{CP} in Au+Au collisions at different energies. (Right) Integrated yields ($3 < p_T < 3.5$ GeV) per binary collision as a function of # of participants at different collision energies. The yields are normalized such that the yield in most peripheral bin is unity.

Figure 2–4 right shows integrated yields ($3 < p_T < 3.5$ GeV) per binary collision as a function of the number of participants at different collision energies. The yields are normalized such that the yield in the most peripheral bin is unity. It is observed that at high beam energies suppression effects quickly dominate. At lowest beam energies, however, the yields in most central collisions are highly enhanced compared to most peripheral collisions. At $\sqrt{s_{NN}} = 14.5$ GeV an approximate flat-ness across centralities is observed, an apparent equilibration of enhancement and suppression effects at this energy and in this p_T region. Theoretical calculations of the beam energy and impact parameter dependence could help understand the dynamics at play here and possibly uncover the suppression effects from data.

2.1.5 Flow and Fluctuations

Recently, we have begun to map v_n at mid and forward rapidities in Au+Au collision at 7.7, 11.5, 19.6, 27, 39, 62.4 and 200 GeV. Figure 2–5 shows that for a given beam energy, similar η dependencies are obtained for $v_{2,3,4}$ but with magnitudes which have a strong dependence on the harmonic number n .

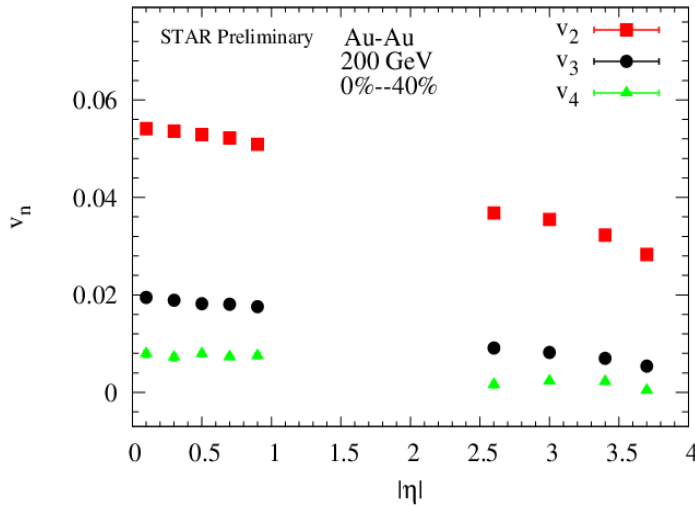


Figure 2–5 Pseudorapidity dependence of v_n in 0-40% central Au+Au collisions at 200 GeV.

Figure 2–6 compares the beam energy dependence of v_2 at mid (TPC) and forward rapidities (FTPC). A much steeper increase of v_2 with beam energy can be observed in Figure 2–7, indicating a similar monotonic increase of $v_{2,3,4}$ with beam energy, again with a strong dependence on the harmonic number.

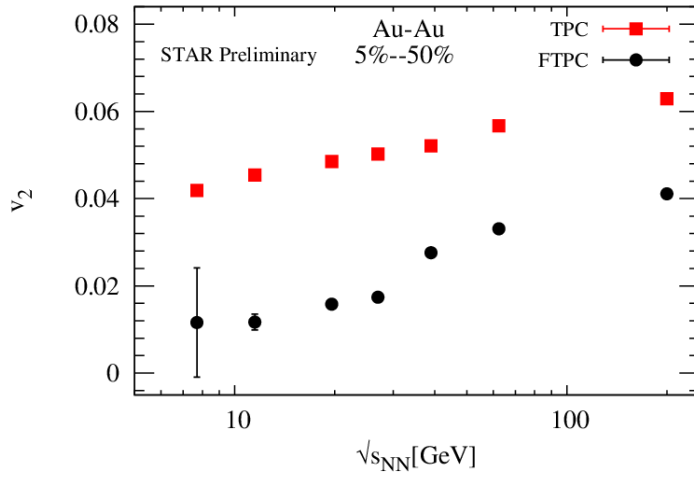


Figure 2-6 Energy dependence of v_2 for mid and forward rapidity selections of 0-40% central Au+Au collisions

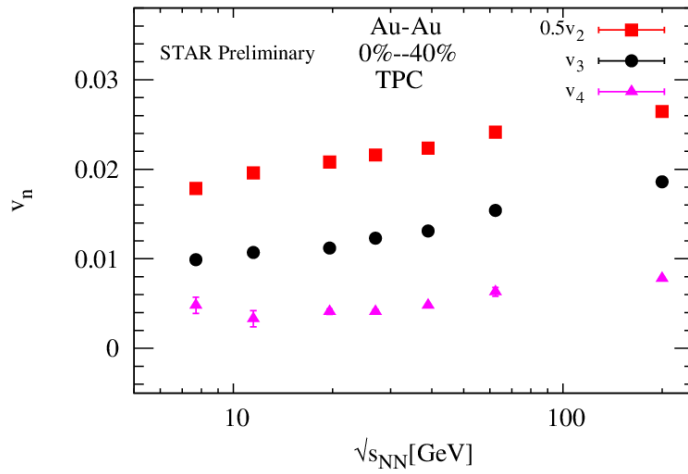


Figure 2-7 Energy dependence of v_n for 0-40% central Au+Au collisions.

Triangular flow is argued to be almost directly proportional to the duration of the low-viscosity phase in heavy ion collisions [46]. Figure 2-8 left shows STAR measurements of charged hadron v_3 in Au+Au collisions at $\sqrt{s_{NN}} = 7.7 - 200$ GeV. The data show a sizable v_3 in central to mid-central collisions that persists all the way down to the lowest beam energy inviting the question about the existence of a QGP phase even at those low energies. v_3 is consistent with zero in peripheral collisions for $\sqrt{s_{NN}} \leq 14.5$ GeV. Figure 2-8 right shows v_3 scaled by the multiplicity per participant pair ($n_{ch,PP} = dN_{ch}/dy/(N_{part}/2)$) as a function of collision energy, an observable that is proportional to the system energy density. The data exhibit a flat trend for $\sqrt{s_{NN}} = 7.7 - 20$ GeV, it is another open question whether this could be related to a softening of the Equation of State.

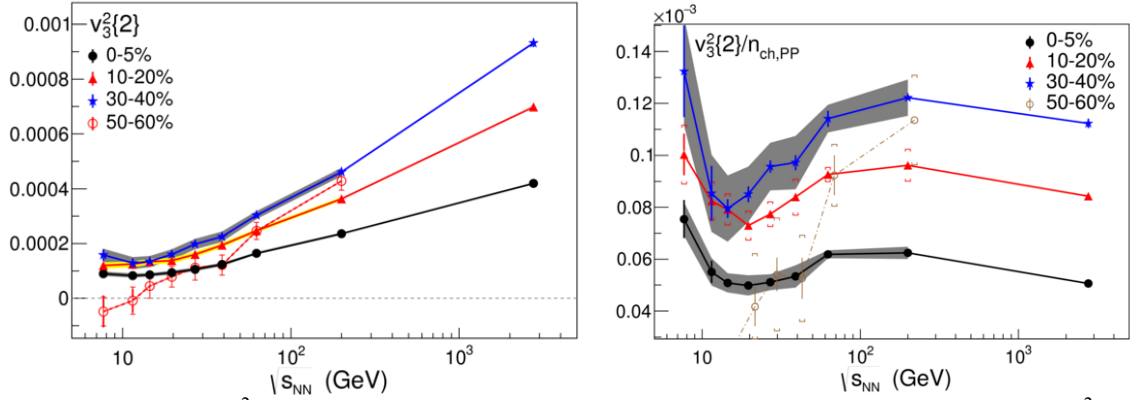


Figure 2-8: (Left) $v_3^2\{2\}$ as a function of beam energy for various centralities. (Right) $v_3^2\{2\}$ scaled by the multiplicity per participant.

The dip in STAR's mid-rapidity measurement of the directed flow net-proton slope [48], $dv_1/dy|_{y=0}$, is due to an interplay between hydrodynamics, baryon transport dynamics and baryon/anti-baryon annihilation. To date all models have failed to reproduce this dip structure indicating that a deeper understanding of these phenomena is necessary to determine if this observation reflects a first order phase transition. STAR has recently measured the directed flow of identified hadrons down to 14.5 GeV. The slopes of net-proton and net-kaon coincides with each other at energies above 14.5 GeV and then starkly split at the lowest two energies. More theoretical insight is needed to understand if this observation is related to the nature of the phase transition at these low energies.

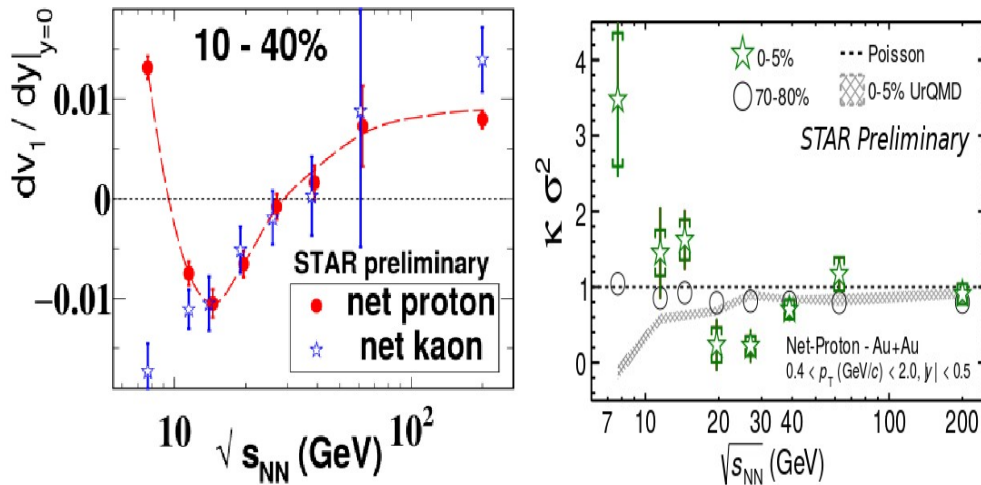


Figure 2-9: (Left) Net-proton and net-kaon $dv_1/dy|_{y=0}$ in Au+Au collisions at different collision energies. (Right) Net-protons $\kappa \sigma^2$ in Au+Au collisions as a function of collision energy compared to UrQMD calculations (hashed area) and Poisson predictions (dashed line) in 0-5% (stars) and 70-80% (circles) centralities.

Higher moments of conserved quantum numbers (charge, strangeness and baryon number) are expected to be sensitive to the proximity of the system to a critical point (see [1] and references therein). It is also expected that higher order moments are more sensitive to criticality. Figure 2–9 right shows net-proton $\kappa\sigma^2$ in most central and peripheral collisions compared to UrQMD and Poisson expectations. The measurement phase space has been recently extended from $0.4 < p_T < 0.8$ to $0.4 < p_T < 2.0$ GeV/c. The data in central collisions clearly show a non-monotonic behavior deviating from the Poisson expectation of unity that is absent from both the peripheral data and UrQMD expectations. More work is being carried out to check if this experimental observable is sufficient to establish the existence of a critical point, the role of the finite volume size in heavy-ion collisions and the system evolution path in the phase diagram [6]. It is currently agreed that more systematic studies of higher moments and their phase space evolution are needed from the experimental side. This is one of the measurements driving the BES-II. STAR’s inner TPC upgrade will extend its coverage from $|\eta| < 1$ to $|\eta| < 1.5$. In addition, an Event Plane Detector (EPD) upgrade at forward rapidities will provide more control on the measurement systematics by giving a TPC-independent measurement of centrality and reaction plane.

2.1.6 Lambda Polarization

STAR has recently discovered global hyperon polarization (GHP), in which the spin of Λ (and $\bar{\Lambda}$) hyperons are preferentially aligned in the direction of the net angular momentum of the QGP $J = b \times p_{beam}$. The Λ polarization (P_Λ) is determined by the Λ decay topology with the TPC, and b is estimated with the STAR BBCs at forward rapidity. Global polarization is distinct from the effect in p+p and p+A collisions, in which Λ are polarized relative to the production plane of the particle, spanned by $\mathbf{p}_{beam} \times \mathbf{p}_\Lambda$ [7][8]. The latter effect is found in the beam fragmentation region (i.e. at forward rapidity) and vanishes by symmetry at mid-rapidity as well as for averages in Λ azimuthal angle. GHP is expected to be driven by two physical effects: the vorticity of the plasma created in the collision and the magnetic field during the system evolution. Non-central collisions are characterized by large angular momentum ($\sim 10^{(4-5)}h$), a portion of which may be transferred to the QGP through QCD spin-orbit coupling [9,10,11] or initial-state viscous effects [12]. In three-dimensional hydrodynamic calculations, the initial shear structure of the flow field results in a vortical structure, in which the QGP would be the highest vorticity fluid ever observed in the laboratory. The vorticity is sensitive to the initial conditions, as well as the viscosity and temperature [13,14] of the fluid as it evolves. Vortical structure of the velocity field has also been recently reported in microscopic transport simulations of heavy ion collisions at RHIC [15].

Hyperon polarization may also arise due to a coupling of the hadronic magnetic dipole moment μ_H to the magnetic field B produced in a non-central heavy ion collision. Whereas the spin-orbit and vortical effects will generate a positive polarization for both Λ and $\bar{\Lambda}$, the magnetic coupling will generate a positive contribution for Λ and a negative one for $\bar{\Lambda}$.

STAR’s preliminary measurements of GHP from the BES-I data are shown together with higher-energy data in Figure 2–10. They utilize all minimum-bias data

recorded, and selected for 20-50% centrality, where the reaction-plane resolution is optimal. The number of good minimum-bias events at 39 GeV was 110M, twice the 63M minimum-bias events at 27 GeV; also, the hyperon yield is (slightly) higher at the higher energy. However, due to much worse reaction plane resolution at higher energy, the error bars for the 39 GeV points are larger than those at 27 GeV. While statistical error bars are substantial, Figure 2–10 clearly demonstrates a significant alignment of hyperon spin with the angular momentum of the system. Both Λ and $\bar{\Lambda}$ are polarized, suggesting dominant vortical polarizing processes. An additional magnetic process is suggested by the fact that $P_{\bar{\Lambda}}$ is consistently larger than P_{Λ} ; however, the difference at any given collision energy is not statistically significant.

For small polarizations, the two effects will add, for primary particles:

$$P_{\Lambda, \text{primary}} = P_V + P_M$$

$$P_{\bar{\Lambda}, \text{primary}} = P_V - P_M$$

Figure 2–10 shows preliminary results for the vortical and magnetic polarization components, after correcting for substantial feed down effects. The contributions of the fluid vorticity (ω) and magnetic field to the hyperon polarizations may be estimated in the nonrelativistic thermal equilibrium limit, in which Boltzmann factors determine the distribution [16]. In the case of spin $\frac{1}{2}$ particles, the corresponding thermal vorticity is of the order several percent, and therefore dominates the observed value. Thus, our results indicate that the QGP at RHIC is the highest-vorticity fluid ever created and observed in the laboratory.

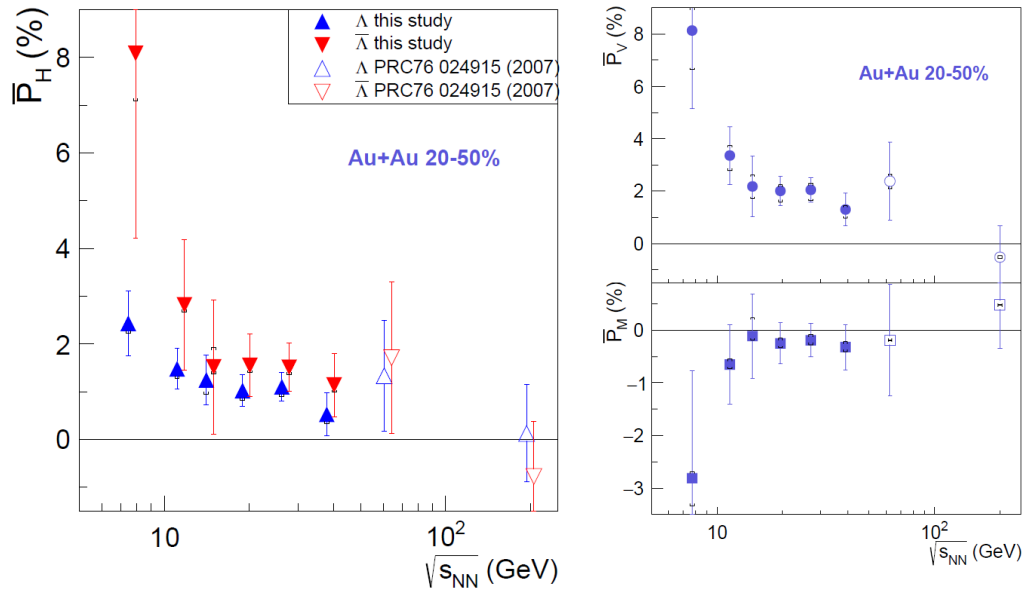


Figure 2–10 STAR Preliminary: (left) The average polarization of hyperons from 20-50% central Au+Au collisions is plotted as a function of collision energy. The results of the present study ($\sqrt{s_{NN}} < 40$ GeV) are shown together with those reported earlier for 62.4 and 200 GeV collisions. Small systematic errors are smaller than statistical ones and arise from residual correlations in the combinatorics background. (right) The vortical (top panel) and magnetic (bottom) contributions to primary Lambda. Systematic uncertainties are smaller than statistical ones in all cases and are shown by error-bar ends. These include effects of residual correlations in the combinatoric background (shown in left panel) as well as from varying the yields in the feed-down calculatons.

2.2 STAR Spin Program

The STAR spin physics program seeks to advance our understanding of the spin and flavor structure of the proton in terms of its constituent quarks and gluons, exploiting the unique capability of RHIC to provide longitudinally and transversely polarized p+p collisions at multiple collision energies. Using longitudinally polarized beams, one can probe the helicity preferences of the gluons and up and down (anti-)quarks, to determine the contribution of each to the total spin of the proton. With spins transverse to their momentum direction, the p+p collisions exhibit kinematic and dynamical effects that are directly sensitive to quark transversity and partonic motion within the proton. This program is complemented by studies of polarized p+p elastic scattering and central exclusive production, in which a far-forward proton is detected intact.

Since 2009 RHIC STAR has completed several very successful polarized p+p runs both at $\sqrt{s} = 200$ GeV and $\sqrt{s} = 510$ GeV. The STAR sampled luminosity and the average beam polarization as measured by the H-jet polarimeter are summarized in Table 2.1. These data sets formed the basis for papers and new preliminary results, which are highlighted in the following sections.

Year	\sqrt{s} (GeV)	Recorded Luminosity for Transverse p+p	Recorded Luminosity for Longitudinal p+p	$\langle P \rangle$ B / Y
2009	200		25 pb ⁻¹	55
	500		10 pb ⁻¹	39
2011	500	25 pb ⁻¹	12 pb ⁻¹	48
2012	200	22 pb ⁻¹	82 pb ⁻¹	61/56
	510			50/53
2013	510		300 pb ⁻¹	51/52
2015	200	52 pb ⁻¹	52 pb ⁻¹	53/57

Table 2.1: Sampled luminosity at STAR and average beam polarization from the H-jet polarimeter.

2.2.1 Transverse Spin Program

Since the last PAC the STAR spin-working group has published two transverse spin papers in Physical Review Letters. The first paper, also selected for a PRL Editor's Suggestion [17], is based on the transversely polarized data set collected during Run 11 at $\sqrt{s} = 500$ GeV. This analysis allowed STAR to make a first measurement to address the non-universality and the evolution of the Sivers function through a measurement of the transverse SSA, A_N for W^\pm and Z^0 bosons. Due to the large STAR acceptance it is possible to reconstruct the W boson kinematics from the recoil jet, a technique established at D0, CDF and the LHC experiments. Figure 2–11 shows the transverse single spin asymmetries A_N for W^\pm and Z^0 bosons, as functions of the boson rapidity y . The asymmetries have also been reconstructed as functions of the p_T of the W -bosons. For the Z^0 -boson the asymmetry could only be reconstructed in one y -bin due to the

currently limited statistics (25 pb^{-1}). A combined fit to the W^\pm asymmetries based on the theoretical predictions of the Kang-Qiu (KQ) model [18] favors a sign-change for the Sivers function relative to the Sivers function in SIDIS with $\chi^2/\text{ndf} = 7.4/6$ compared to $\chi^2/\text{ndf} = 19.6/6$ for no sign-change, if TMD evolution effects are small.

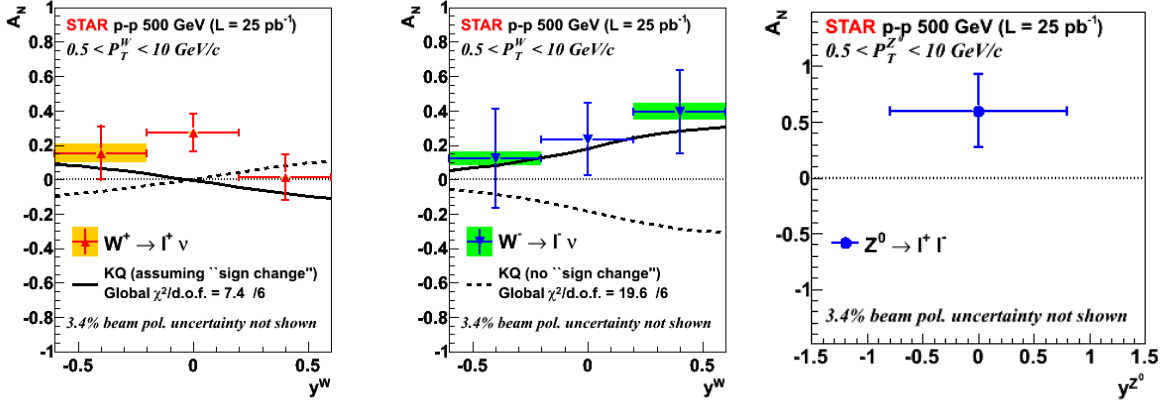


Figure 2–11: Transverse single-spin asymmetry amplitude for W^+ (left plot), W^- (middle plot) and Z^0 boson versus $y_{W/Z}$ measured by STAR in proton-proton collisions at $\sqrt{s} = 500 \text{ GeV}$. The W^\pm boson asymmetries are compared with the non TMD-evolved KQ [18] model, assuming (solid line) or excluding (dashed line) a sign change in the Sivers function.

The second paper [19] reports the first Interference Fragmentation Function (IFF) analysis completed at STAR. This paper is based on 1.8 pb^{-1} of $\sqrt{s} = 200 \text{ GeV}$ transversely polarized p+p data collected during Run 6. It reports signals in excess of five standard deviations at high transverse momentum and is the first transverse single spin asymmetry (A_{UT}) to ever show a significant transversity signal in hadronic collisions.

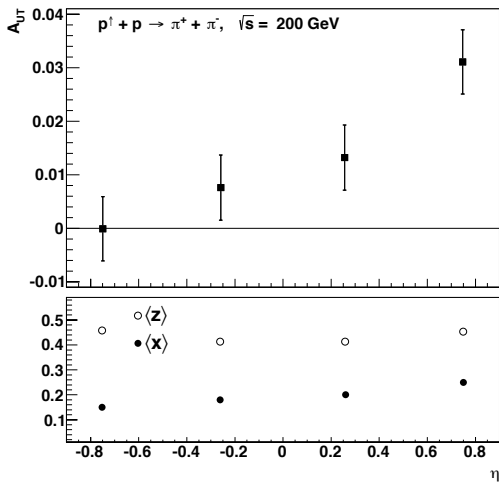


Figure 2–12: A_{UT} as a function of pseudorapidity η (upper) and corresponding partonic variables x and z (lower). The measured asymmetries rise with increasing η , reflecting the x -dependence of the valence quarks that contribute to the transversity signal.

STAR has also released preliminary single spin asymmetries of forward π^0 A_N in $p^\uparrow + \text{Au}$ and $p^\uparrow + p$ scattering data collected during Run 15. The nuclear dependence of

single spin asymmetries provides unique information about the dynamics of the strong interaction in nuclear collisions and may serve to distinguish between various theoretical predictions. For example, theoretical approaches based on color glass condensate physics (CGC) predict an inverse correlation between A_N and the size of the nuclear target [20], while frameworks based on pQCD factorization predict very little to no change with target species [21].

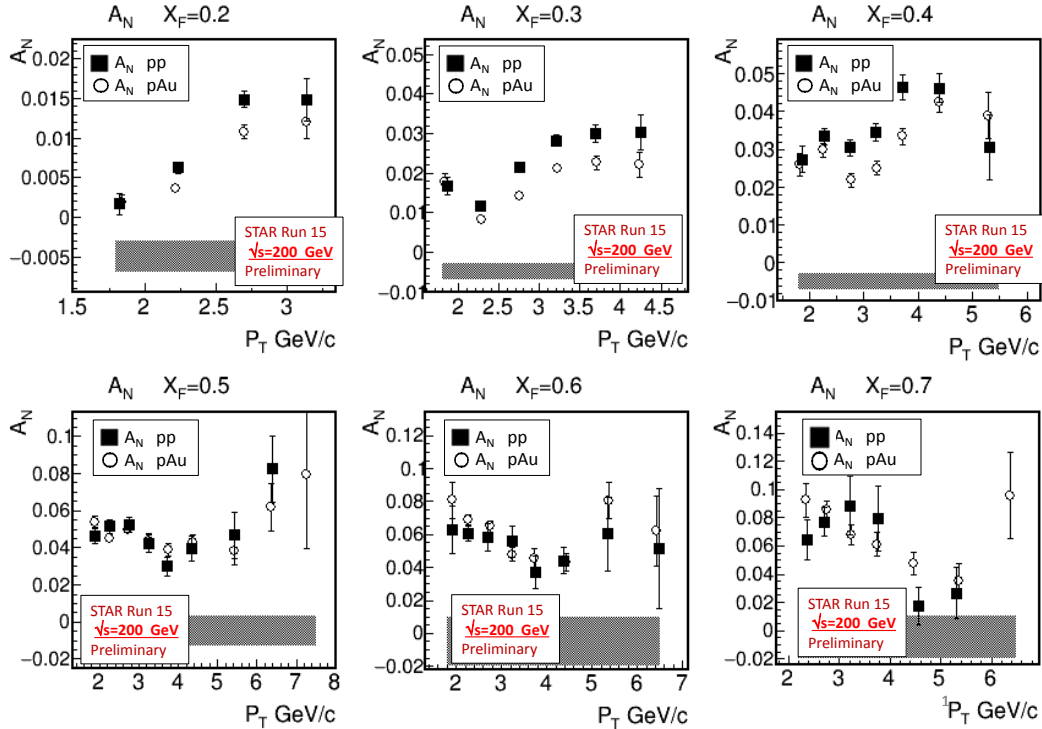


Figure 2–13: STAR π^0 A_N measured in the rapidity range $2.5 < \eta < 4.0$ as function of p_T and Feynman- x ($x_F = x_1 - x_2$) for transversely polarized p+p and p+Au collisions

Figure 2–13 shows the STAR π^0 A_N measured in the rapidity range $2.5 < \eta < 4.0$ as function of p_T and Feynman- x ($x_F = x_1 - x_2$) for transversely polarized p+p and p+Au collisions. This was released at the 7th International Workshop on Multiple Partonic Interactions at the LHC in the fall of 2016. The fact that strong suppression effects are not observed for A_N in p+Au collisions favors the pQCD interpretation. However, this conflicts with our current understanding that a significant fraction of the large transverse single spin asymmetries in the forward direction are not of $2 \rightarrow 2$ parton scattering processes. This result demonstrates the clear need for more data to understand the true physics origin for the large forward SSA and the missing nuclear dependence.

2.2.2 Longitudinal Spin Program

Since the last PAC the STAR spin-working group has published one longitudinal spin paper in Physical Review Letters. This paper, also chosen for an Editor’s Suggestion [22], presents the inclusive jet double spin asymmetry A_{LL} extracted from 20 pb^{-1} of $\sqrt{s} =$

200 GeV longitudinally polarized p+p collisions collected in Run 9. This analysis, shown in Figure 2–14, provided the first conclusive evidence of a significant gluon contribution to the proton spin.

STAR continues to provide new constraints on the gluon helicity distribution down to momentum fractions $x \sim 0.02$ through measurements of inclusive jet and dijet longitudinal double spin asymmetries (A_{LL}) at $\sqrt{s} = 510$ GeV. While inclusive channels maximize statistical power they do not permit event-by-event reconstruction of the underlying partonic kinematics in proton-proton collisions. Instead they sample an x range amounting to a fraction of the total integral $\Delta G(Q^2)$ and provide only coarse constraints on the functional form of the underlying shape of $\Delta g(x, Q^2)$, which in turn produces a large theoretical uncertainty in the determination of the total integral. The x dependence can be mapped via correlation measurements, such as dijets. At leading order it is possible to determine the kinematics, such as the momentum fraction of the colliding partons, from the invariant mass of the dijet pair (M_{inv}) and pseudorapidity of the individual jets.

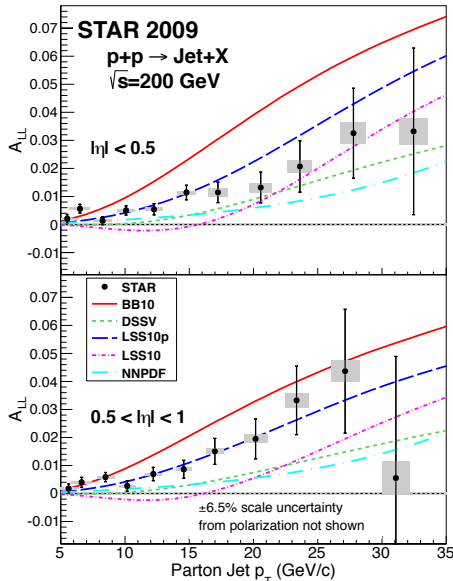


Figure 2–14 Inclusive jet A_{LL} versus the jet p_T corrected for hadronization and underlying event effects.

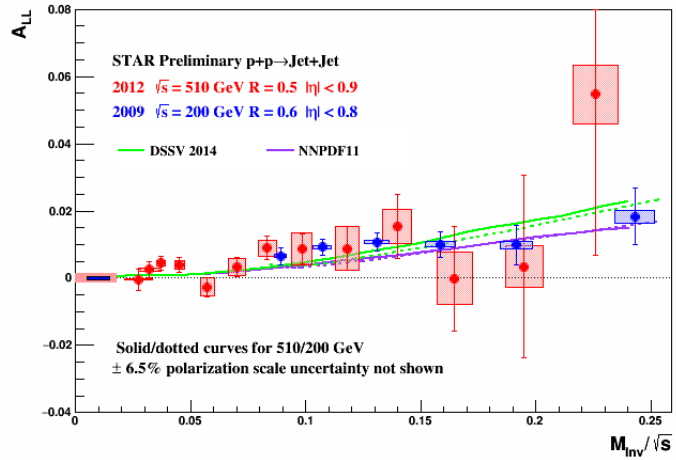


Figure 2–15 STAR preliminary measurements of the dijet A_{LL} versus M_{inv}/\sqrt{s} of the pair for mid-rapidity p+p collisions at $\sqrt{s} = 200$ (blue) GeV and $\sqrt{s} = 510$ (red) GeV, compared to predictions based on the DSSV14 and NNPDFpol1 global analyses.

Figure 2–15 shows the first measurement of the mid-rapidity dijet A_{LL} at $\sqrt{s} = 510$ GeV, released for the 24th International Workshop for Deep Inelastic Scattering in April of this year. A_{LL} is plotted as a function of the corrected M_{inv} divided by \sqrt{s} , a quantity related to the product of the momentum fractions carried by scattered partons, and one that facilitates the comparison of dijet asymmetries at different center of mass energies. The red (blue) markers represent the dijet A_{LL} at $\sqrt{s} = 510$ (200) GeV and the shaded boxes are the associated systematic errors. The two data sets demonstrate excellent agreement with theoretical predictions from global analyses performed by the DSSV and NNPDF groups,

as well as with each other in the region of overlap. The uncertainties will be reduced by a factor of approximately 1.7 after additional data recorded during 2013 (510 GeV) and 2015 (200 GeV) are included.

2.3 REVIEW OF THE CHIRAL MAGNETIC /VORTICAL EFFECTS

STAR has published five papers on the evidence of the chiral magnetic effect, and recently one on the search for the chiral magnetic wave (chosen for an Editor’s Suggestion). The first evidence of the chiral vortical effect was presented by STAR in the QM2014. The background contributions from conventional physics are being intensively investigated, which motivated the U+U collisions in 2012, and requires the isobaric collisions in the near future.

2.3.1 Chiral Magnetic Effect

Inside the QGP created at RHIC, vacuum transitions could occur in metastable domains of topologically twisted gluon fields, along with a violation of space and time reflection symmetry, like the chirality imbalance. The experimental search for this local parity violation in the strong interaction was greatly intensified once it was noticed [23, 24] that in non-central nuclear collisions it could lead to the asymmetry in the emission of positively and negatively charged particles along the direction of the angular momentum of the collision. Such a charge separation is the manifestation of the chirality imbalance of massless quarks with the help of the strong magnetic field (10^{15} T) of a non-central collision, and is known as the chiral magnetic effect (CME) [23, 25].

A three-point correlator, $\gamma \equiv \langle \cos(\varphi_\alpha + \varphi_\beta - 2\Psi_{RP}) \rangle$, sensitive to the CME was proposed [26], where φ is the azimuthal angle, the subscripts α and β denote the particle charge (positive or negative), and Ψ_{RP} is the angle of the reaction plane of a given event. The observable γ represents the difference between azimuthal correlations projected onto the desired direction of the magnetic field and correlations projected onto the collision event plane. The STAR measurements of this correlator for Au+Au collisions at 200 GeV [27,28,29] shown in Figure 2–16(b) demonstrate the “expected” ordering of the opposite charge (γ_{OS}) and the same charge (γ_{SS}) correlations. This is consistent with the formation of deconfined and chirally-symmetric matter in high-energy heavy-ion collisions. The signal is robust to various ways of determination of the reaction plane, and persists when the collision system changes to Cu+Cu, Pb+Pb or U+U. No known event generators can reproduce the experimental signal.

Figure 2–16 presents γ_{OS} and γ_{SS} correlators for Au+Au collisions at $\sqrt{s_{NN}} = 7.7$ -200 GeV as a function of centrality [30]. In addition, the ALICE measurements for 2.76 TeV Pb+Pb collisions are also shown [31]. The ordering of γ_{OS} and γ_{SS} is present at higher energies. This is consistent with extra charge-separation fluctuations along the magnetic field due to the CME. At lower beam energies, both γ_{OS} and γ_{SS} tend to rise for peripheral

collisions. This feature seems to be charge independent, and can be explained by momentum conservation and elliptic flow [29].

An ambiguity in the interpretation of experimental results comes from possible background correlations not related to the CME. The background sources, if coupled with collective flow, will contribute to γ . In order to separate the signal associated with the CME from that due to the background contributions, we can express the experimental observables in the following forms, where the unknown parameter κ is of the order of unity [32].

$$\gamma \equiv \langle \cos(\varphi_\alpha + \varphi_\beta - 2\Psi_{RP}) \rangle = \kappa v_2 F - H \quad (1)$$

$$\delta \equiv \langle \cos(\varphi_\alpha - \varphi_\beta) \rangle = F + H, \quad (2)$$

where H and F are the CME and background contributions, respectively. For the STAR acceptance, we estimate that $\kappa \approx 1.3$ – 1.4 due to transverse momentum conservation. Figure 2–17 shows $(H_{SS} - H_{OS})$ as a function of beam energy for three centrality bins in Au+Au collisions [30]. The default values (dotted curves) are from $H^{\kappa=1}$, and the solid curves are obtained with $\kappa = 1.5$. For comparison, the results for 10 – 60% Pb+Pb collisions at 2.76 TeV are also shown [31]. For both κ values, H demonstrates a weak energy dependence above 19.6 GeV, and approaches zero at the lowest beam energy, although the statistical errors are large for 7.7 GeV. Recent STAR preliminary H results for 14.5 GeV collisions further confirm the trend established by other beam energies. This trend may be explained by the probable dominance of hadronic interactions over partonic ones at the lowest energies. The energy for which $\Delta H = 0$ will be determined quantitatively with higher statistics in the BES-II.

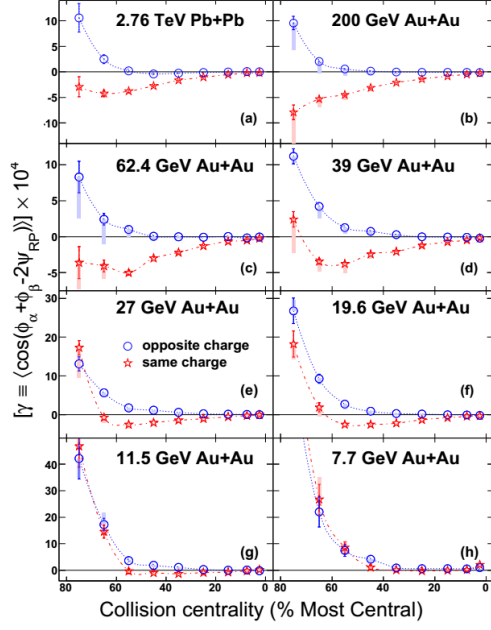


Figure 2–16: The three-point correlator as a function of centrality for Au+Au collisions at 7.7–200 GeV [27–31]. Note that the vertical scales are different for different rows. The systematic errors (filled boxes) reflect the extra conditions of $p_T > 0.15$ GeV/c and $\eta > 0.15$ to suppress HBT+Coulomb effects.

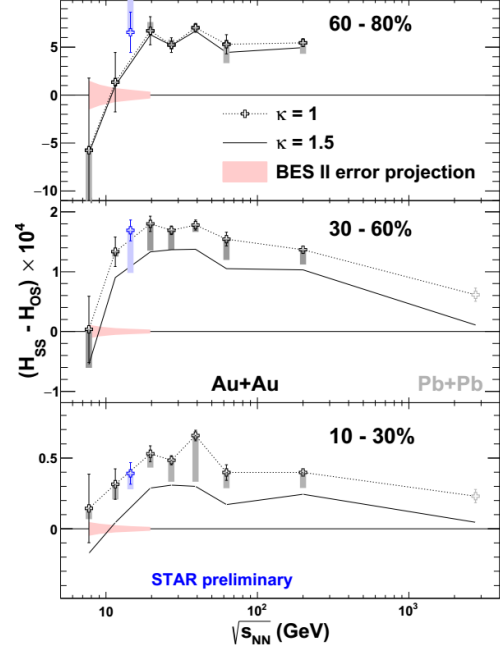


Figure 2–17: $(H_{SS} - H_{OS})$ vs beam energy for three centrality bins [30]. The default values (dotted curves) are $H^{\kappa=1}$, and the solid curves are obtained with $\kappa = 1.5$. For comparison, the results for Pb+Pb collisions at 2.76 TeV are also shown [31]. The systematic errors have the same meaning as in Figure 2–16.

Part of the motivation for the U+U run at RHIC in 2012 was to study CME in central collisions where the magnetic field was thought to be small while v_2 would remain large. Subsequent studies suggest that the square of the magnetic field is not small however because of fluctuations. STAR showed that in very central collisions the number of produced particles does not depend as strongly on the configuration of the collisions as anticipated in the two component multiplicity model which leaves the experiments with a significantly reduced ability to independently manipulate the flow and the magnetic field [33]. Figure 2–18 (left) shows measurements of $\gamma_{OS} - \gamma_{SS}$ vs v_2 for different centralities in 193 GeV U+U and Figure 2–18 (right) for 200 GeV Au+Au collisions [34]. In both U+U and Au+Au collisions, the signal increases roughly with v_2 . This observation may at first suggest that the charge separation is dominated by a v_2 dependence. This interpretation is contradicted however by the observation that charge separation goes to zero while v_2 is still large in central Au+Au and central U+U collisions in a manner that is consistent with expectations of CME. More sophisticated model calculations show that the quantity relevant to charge separation $\langle (eB/m_\pi)^2 \cos[2(\Psi_B - \Psi_{RP})] \rangle$ exhibits the same trend as a function of eccentricity as the charge separation does as a function of v_2 . In the models this can be traced to the fact that while $\langle B^2 \rangle$ remains large due to fluctuations, $\langle \cos[2(\Psi_B - \Psi_{RP})] \rangle$ goes to zero as Ψ_B and Ψ_{RP} become de-correlated in very central collisions. So while fluctuations in central collisions force the participant eccentricity (a positive-definite quantity) away from zero, the de-correlation of Ψ_B and Ψ_{RP} drives

$\langle (eB/m_r)^2 \cos[2(\Psi_B - \Psi_{RP})] \rangle$ to zero [34]. The central U+U and Au+Au data appear to contradict a flow background interpretation and favor a CME interpretation.

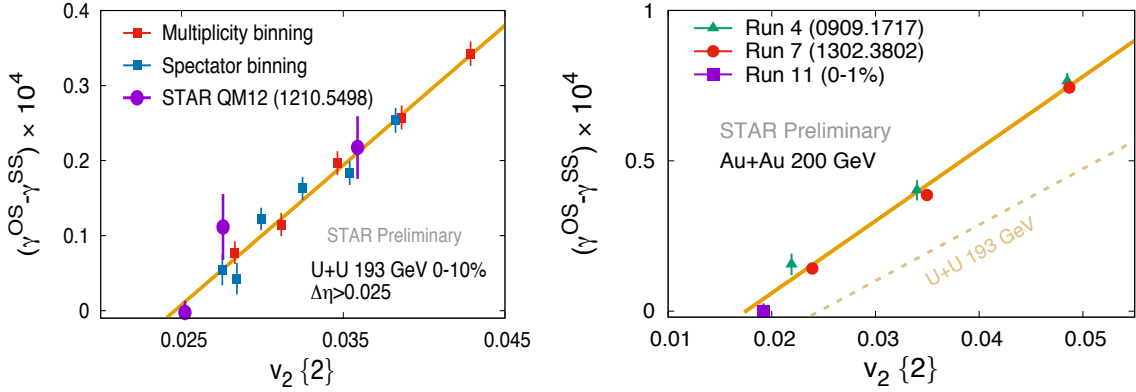


Figure 2–18: $\gamma_{OS}\text{-}\gamma_{SS}$ vs v_2 for different centralities in 193 GeV U+U collisions (left) and 200 GeV Au+Au collisions (right).[34]

2.3.2 Chiral Magnetic Wave

Besides the chiral magnetic effect, the chiral separation effect (CSE) has also been proposed. The CSE refers to the separation of chiral charge along the axis of the magnetic field at finite density of vector charge (e.g. electric charge) [35, 36]. In a chirally-symmetric phase, the CME and CSE form a collective excitation, a chiral magnetic wave (CMW), a long-wavelength hydrodynamic mode of chiral charge densities [37]. The CMW is a signature of the chiral symmetry restoration in the QGP, and manifests itself in a finite electric quadrupole moment of the collision system, where the “poles” (“equator”) of the produced fireball acquire additional positive (negative) charge. This effect, if it exists, will be reflected in the measurement of charge-dependent elliptic flow. Taking pions as an example, on top of the baseline $v_2^{\text{base}}(\pi^\pm)$, the CMW will lead to [37] $v_2(\pi^\pm) = v_2^{\text{base}}(\pi^\pm) \mp (q_e/\rho_e)A_{\text{ch}}$, where q_e , ρ_e and $A_{\text{ch}} = (N_+ - N_-)/(N_+ + N_-)$ are the quadrupole moment, the net charge density and the charge asymmetry of the collision event, respectively. The baseline v_2 may be different for π^+ and π^- because of several other physics mechanisms, so it is less ambiguous to study the CMW via the A_{ch} dependence of pion v_2 .

Taking 30–40% 200 GeV Au+Au as an example, the pion v_2 is shown as a function of A_{ch} in panel (a) of Figure 2–19. The π^- v_2 increases with A_{ch} while the π^+ v_2 decreases with a similar magnitude of slope. The v_2 difference between π^- and π^+ is fitted with a straight line in panel (b). The slope parameter r , or presumably $2q_e/\rho_e$ from Eq. 3, is positive and qualitatively consistent with the expectation of the CMW picture. We retrieve the slope parameter r for all centrality bins as shown in Figure 2–20. The slopes are consistent with zero for the most central and most peripheral collisions, and are positive and reach a maximum in mid-central/mid-peripheral collisions. For Au+Au collisions at 200 GeV, the slopes extracted from UrQMD events [38] are consistent with zero for the 10-70% centrality range, where the signal from the real data is prominent. Similarly, the AMPT event generator [39] also yields slopes consistent with zero (not shown here). On the other hand, simplified CMW calculations demonstrate a similar centrality dependence of the slope parameter [40]. At 200 GeV, STAR preliminary results with kaons

instead of pions, with U+U instead of Au+Au collisions and with v_3 instead of v_2 , all favor the CMW interpretation [41].

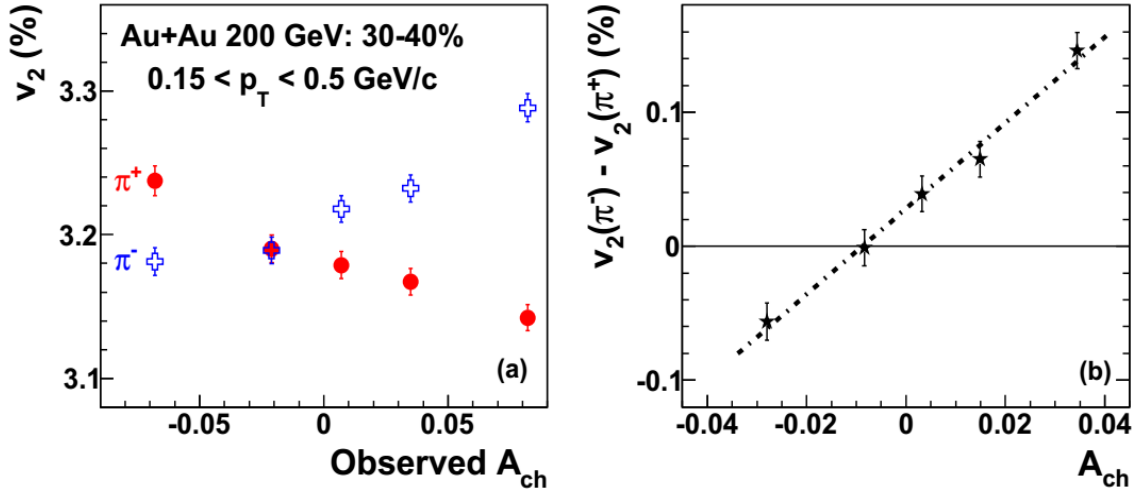


Figure 2–19 (a) pion v_2 as a function of observed charge asymmetry and (b) v_2 difference between π^- and π^+ as a function of charge asymmetry with the tracking efficiency correction, for 30-40% Au+Au collisions at 200 GeV.

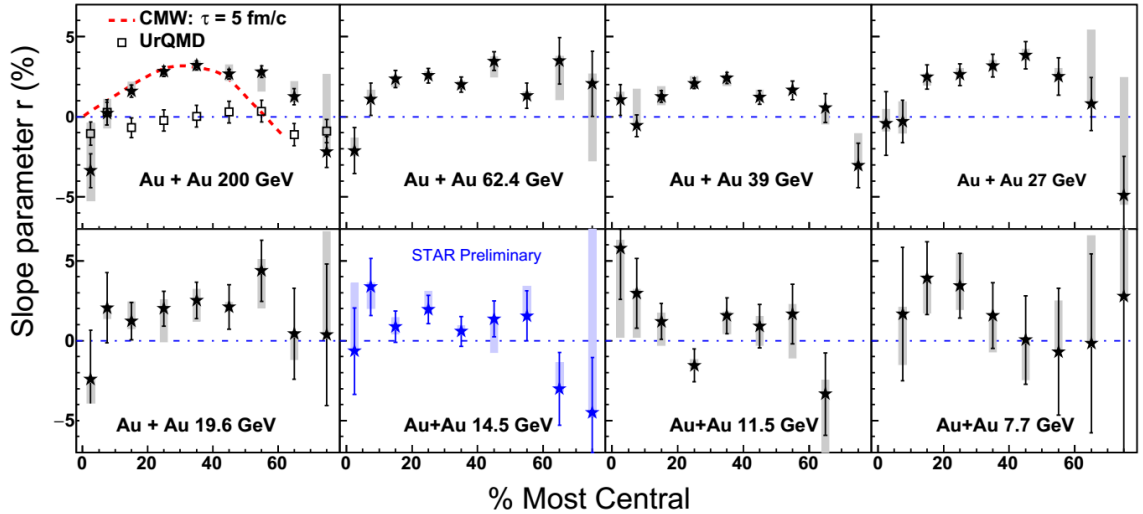


Figure 2–20 The slope parameter r as a function of centrality for all the collision systems under study. For comparison, we also show the UrQMD calculations [38] and the calculations with CMW with the duration time $\tau = 5$ fm/C [40]. The gray bands include the systematic errors due to the DCA cut, the tracking efficiency and the p_T range of particles involved in the event plane determination.

STAR results show a similar trend and magnitude of the slopes for Au+Au collisions from 200 GeV to 19.6 GeV, below which the statistical errors become too large to draw a firm conclusion. With the proposed numbers of events for the BES-II, we will be able to reduce the statistical errors, and further search for the CMW at lower energies. The possible disappearance of the CMW at lower energies would signify chiral symmetry breaking.

2.3.3 Chiral Vortical Effect

In addition to the chiral magnetic effect, a chiral vortical effect (CVE) has also been predicted [42]. In this case, the role of the magnetic field is played by vorticity coupled with a baryon chemical potential (μ_B), and the resultant electric charge separation will be replaced with the baryonic charge separation. Vorticity in heavy-ion collisions is a natural consequence of angular momentum conservation, and there is always a finite μ_B at RHIC energies. The CVE can be searched for via γ correlations between two baryons, one of which is preferably charge neutral to avoid the complication by the CME. Indeed, STAR preliminary results for Λ -proton correlations [43] in Figure 2–219 show the separation between opposite- and same-baryon number correlators (γ) in Au+Au collisions at 200 GeV. The statistics requested for BES-II will enable such an analysis at lower energies, where the relative importance of baryon number separation increases with decreased beam energy of collisions where μ_B is larger.

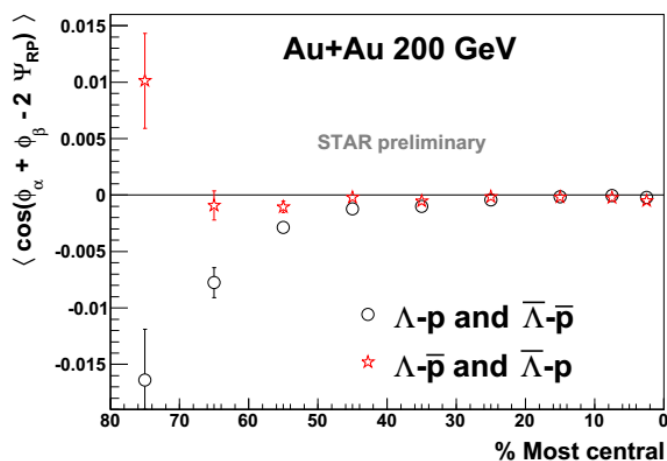


Figure 2–21 γ -correlation of Λ - p (Λ - \bar{p}) and Λ - \bar{p} (Λ - p) vs centrality in Au+Au collisions at 200 GeV.

2.4 Progress on Physics Analyses with the Heavy Flavor Tracker

During Run 14 the HFT was fully commissioned and participated in the Au-Au 200 GeV physics data taking. Around 1.2B MB events were recorded with both the PXL and IST sub-detectors. Preliminary physics results extracted from $\sim 65\%$ of this data sample were presented at the QM2015 conference by three contributed presentations, as well as highlighted in the STAR overview talk.

We are in the process of finalizing our open charm measurements made via the hadronic channels. Improvements in both the statistical and systematic uncertainties are expected. In particular, a significant reduction on the statistical uncertainty is expected due to the improved PXL matching efficiency in offline data reconstruction after fixing a decoder bug. Studies with both data and detector simulations are also underway to understand the HFT acceptance, efficiency and resolution, and reconstruction effects at lower p_T and in peripheral Au+Au collisions. The full 2014 Au+Au data sample should

also allow us to measure separately charm- and bottom-decay electrons. While the focus is currently on the 2014 Au+Au data, preliminary analyses have begun on the p+p and p+Au data taken in 2015.

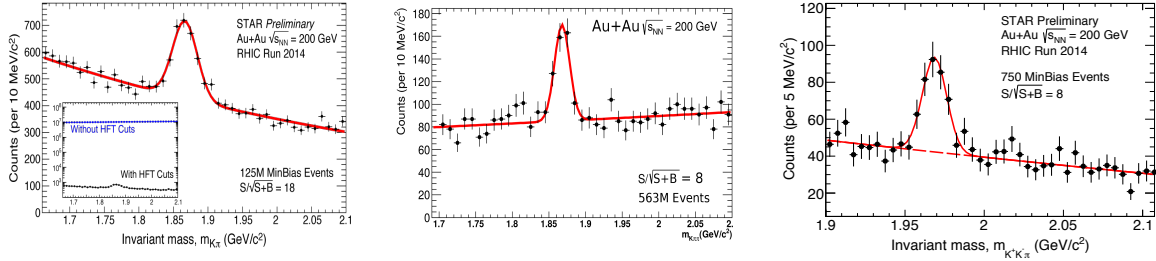


Figure 2–22 from left to right: Example invariant mass spectra for $D^0 \rightarrow K^- \pi^+$, $D^\pm \rightarrow K^\mp \pi^\pm \pi^\pm$ and $D_s^\pm \rightarrow \phi(\rightarrow K^+ K^-) \pi^\pm$ channels respectively, from Run 14 Au+Au 200 GeV data.

Shown in Figure 2–22 are example invariant mass spectra for D^0 , D^\pm and D_s candidates via the $D^0 \rightarrow K^- \pi^+$, $D^\pm \rightarrow K^\mp \pi^\pm \pi^\pm$ and $D_s^\pm \rightarrow \phi(\rightarrow K^+ K^-) \pi^\pm$ channels, respectively. Here charged Kaons and pions were identified by the TPC and TOF. Topological cuts were applied on the DCA's among Kaons, pions and the primary vertex that were precisely determined by the HFT, thanks to its excellent resolution. These topological cuts successfully suppress the combinatorial background contribution due to primary Kaons and pions, greatly enhancing the D meson signal significances.

Detailed below are the preliminary 200 GeV Au+Au D^0 results shown at QM2015. Also presented at this conference but not shown here were R_{AA} and v_2 results for D^\pm and D_s mesons. Measurements with much better precision are expected from the full Run 14+16 data with the improvements described in Section 2.4.

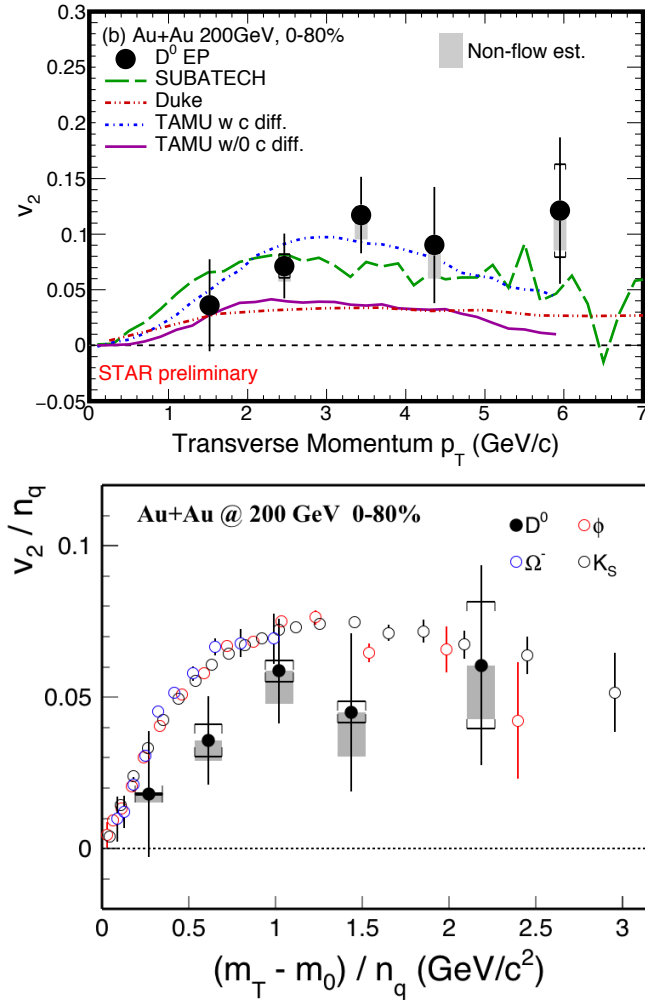


Figure 2-23 (Top) Measured D^0 v_2 compared to different model calculations. (Bottom) Measured D^0 v_2 compared to light hadron v_2 .

Figure 2-23 shows the the first experimental verification of charmed hadron elliptic flow in Au+Au collisions at RHIC. The measured D^0 v_2 is in better agreement with the theoretical prediction by the TAMU group including charm quark diffusion than that without diffusion. As can be seen in the right panel, the measured D^0 v_2 is systematically lower than light hadron v_2 , suggesting that the charm quark is not fully thermalized at RHIC energies.

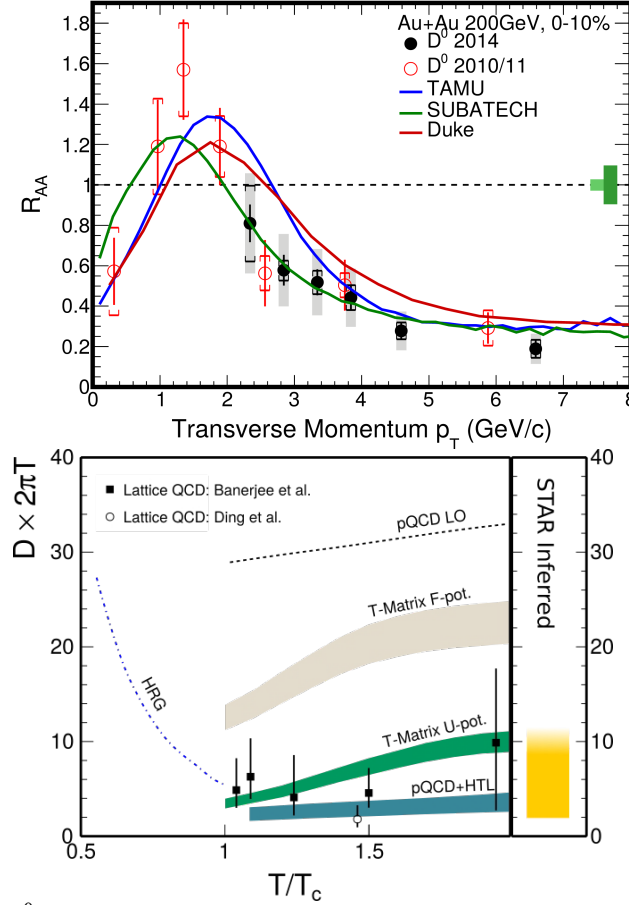


Figure 2–24 (Left) $D^0 R_{AA}$ in 0-10% most central Au+Au 200 GeV collisions measured by STAR and from theoretical model calculations. (Right) Charm quark diffusion constant $D \times 2\pi T$ inferred from STAR $D^0 v_2$ data and compared to Lattice QCD calculations.

This partial data set was also used to determine the nuclear modification factor of D^0 mesons with $2 < p_T < 8$ GeV/c in the 0-10% most central Au+Au collisions. A data-driven approach was used to obtain and correct for the HFT acceptance, efficiency and resolution effects. The result is shown in the left panel of Figure 2–24 and compared to the previously published STAR result from 1.1 B MB events taken in 2010 and 2011 prior to the installation of the HFT. Despite using a smaller data sample, the new 2014 result has significantly smaller statistical uncertainties thanks to the precision vertexing of the HFT. As for the v_2 measurement, the R_{AA} of D^0 mesons can be reasonably described by theoretical model calculations including charm quark diffusion, left panel of Figure 2–24. The current data suggest a charm quark diffusion, $D \times 2\pi T$, that ranges between 2–11. This inferred range of $D \times 2\pi T$ is consistent with those calculated by Lattice QCD calculations (see the right panel of Figure 2–24).

2.5 Progress on Physics Analyses with the Muon Telescope Detector

Since 2013 the full MTD has been operational in STAR. Hence MTD data is available for the following systems at 200 GeV Au+Au, $^3\text{He}+\text{Au}$, p+p, p+Au, and p+Al. Data from p+p at 500 GeV (Run 13) has also been recorded. Three MTD triggers were successfully implemented including a single-muon, dimuon, and μ -e trigger and all ran smoothly. In total STAR recorded: 11 nb^{-1} , 120 pb^{-1} , and 400 nb^{-1} effective luminosity with the dimuon trigger for Au+Au (Run 14), p+p (Run 15) and p+Au (Run 15) collisions respectively. These triggered datasets will be used for quarkonium analyses.

We have completed calibrations for 500 GeV p+p collisions, 200 GeV Au+Au collisions from Run 14, and 200 GeV p+p collisions from Run 15. The full datasets for 500 GeV p+p collisions in Run 13 and 200 GeV Au+Au collisions in Run 14 have been produced and the data production for 200 GeV Au+Au collisions in Run 14 was completed in Mar. 2016. To date, 1/8 of the full 200 GeV p+p data in Run 15 has been produced. The efficiency correction procedure has been established with simulations and cosmic ray data samples and has been successfully applied to the 500 GeV p+p and 200 GeV Au+Au (Run 14) data.

Below we present new preliminary physics results from 500 GeV p+p collisions and the Run 14 200 GeV Au+Au collisions

2.5.1 J/ψ Production in p+p at 500 GeV

A clear $J/\psi \rightarrow \mu^+ \mu^-$ signal in Run 13 p+p at 500 GeV has been obtained, as shown in the left panel of Figure 2–25. The efficiency and acceptance corrected invariant yield of $J/\psi \rightarrow \mu^+ \mu^-$ as a function of transverse momentum is shown in the right panel of Figure 2–25. Our measurements are consistent with model calculations based on NRQCD and CGC. Also shown are STAR's high p_T $J/\psi \rightarrow e^+ e^-$ measurements. In the overlapped p_T region the measurements from the dimuon and di-electron decay channels are consistent. We plan to release this result this summer at the SQM2016 conference.

In Figure 2–26, we show the J/ψ production yield ($N_{J/\psi}$) in different p_T ranges as a function of the TofMult multiplicity. TofMult is defined as the number of reconstructed TPC tracks that can be projected and matched to a ToF hit. Both $N_{J/\psi}$ and TofMult are normalized by their average values in minimum bias p+p events. One can see that $N_{J/\psi}$ increases faster than TofMult. This result was first shown at Hard Probes 2015 and will help improve our understanding of J/ψ production mechanisms.

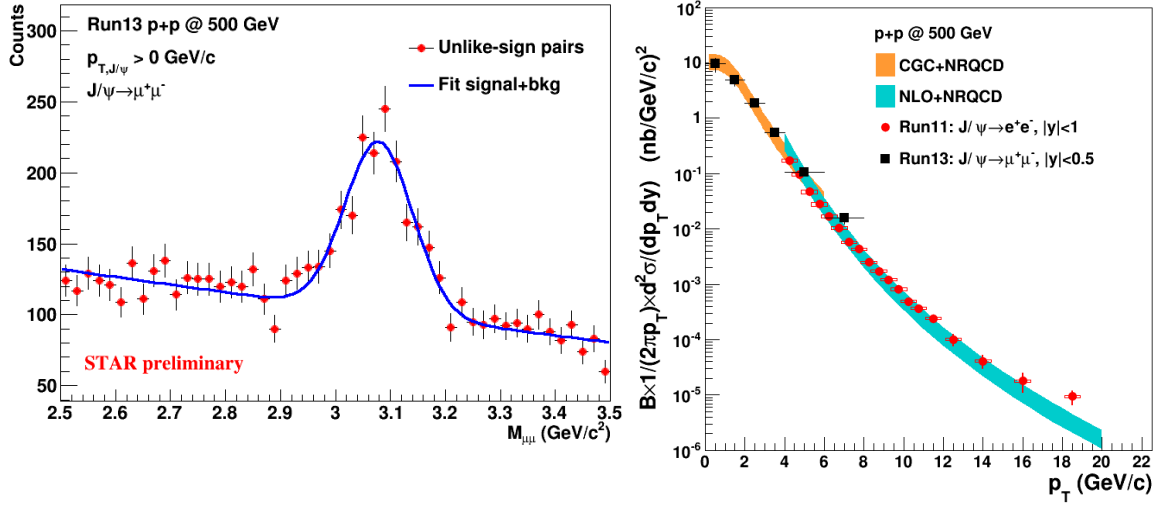


Figure 2–25: $J/\psi \rightarrow \mu^+ \mu^-$ signals in Run 13 p+p at 500 GeV (left) and the invariant yield of $J/\psi \rightarrow \mu^+ \mu^-$ as a function of transverse momentum compared to $J/\psi \rightarrow e^+ e^-$ measurements at higher p_T and theoretical calculations (right).

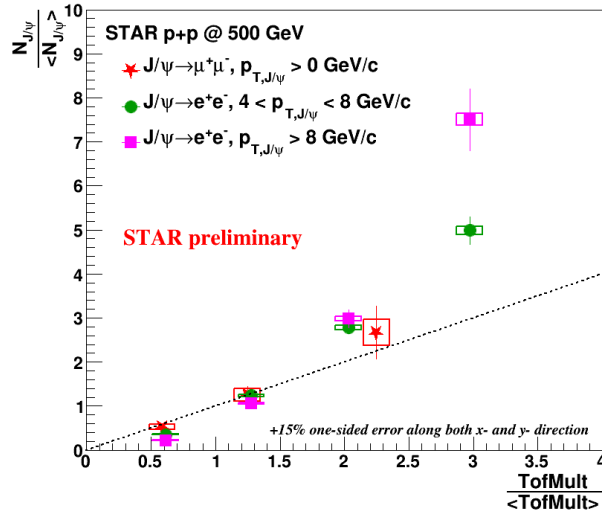


Figure 2–26: The J/ψ production yield ($N_{J/\psi}$) in different p_T ranges as a function of TofMult (see text for definitions).

2.5.2 J/ψ Production and Υ states Ratios in Au+Au Collisions at 200 GeV

Preliminary MTD results on $J/\psi \rightarrow \mu^+ \mu^-$ invariant spectra, nuclear modification factors and v_2 as a function of p_T using only only 30% of the full Run 14 dimuon data sample were shown at Quark Matter 2015. With the full data production completed in March 2016, we expect to present updated measurements utilizing the the full statistics on all three of these analyses at SQM2016.

Figure 2–27 shows $J/\psi \rightarrow \mu^+ \mu^-$ invariant mass signals for several p_T bins for $1 \text{ GeV}/c < p_T < 10 \text{ GeV}/c$. These strong signals were corrected for efficiency and acceptance and the resulting invariant yields compared STAR’s published results from the di-electron channel, as shown in the left panel of Figure 2–28. Good consistency is observed. Using STAR’s published p+p baseline, we proceeded to extract the J/ψ nuclear modification factor R_{AA} shown in right panel of Figure 2–28. Our dimuon data confirms the rising trend of J/ψ R_{AA} as a function p_T . Figure 2–29 shows the $J/\psi \rightarrow \mu^+ \mu^-$ v_2 together with results from the di-electron decay channel shown at QM2015. More precise R_{AA} and v_2 measurements from the full Run 14 data will help understand the interplay of dissociation and recombination for J/ψ production in heavy ion collisions.

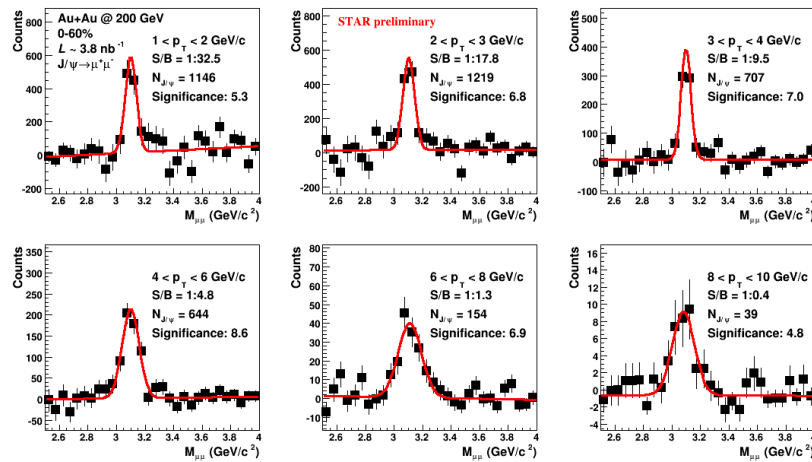


Figure 2–27: shows $J/\psi \rightarrow \mu^+ \mu^-$ signals for several p_T bins for $1 \text{ GeV}/c < p_T < 10 \text{ GeV}/c$ in Run 14 Au+Au at 200 GeV.

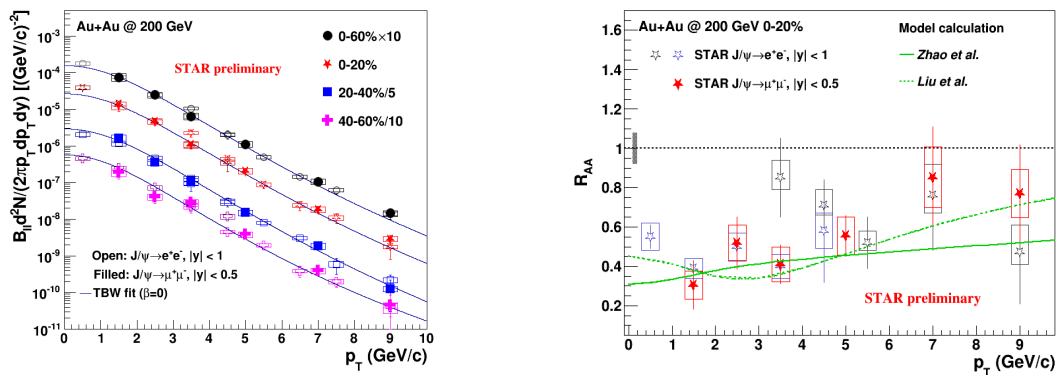


Figure 2–28: The invariant yield (left) and nuclear modification factor (right) of $J/\psi \rightarrow \mu^+ \mu^-$ as a function of transverse momentum in Au+Au collisions.

Figure 2–30 shows the $\mu^+ \mu^-$ mass distribution after combinatorial background subtraction. A clear Υ signal was observed from 30% of the full Run 14 dimuon data

sample and the result was presented at Quark Matter 2015. Again we expect to present the results with full statistics from Run 14 at SQM2016, aiming for obtaining different Upsilon states ratio in Au+Au collisions at 200 GeV. The measurements will help constrain the temperature parameter of the QGP.

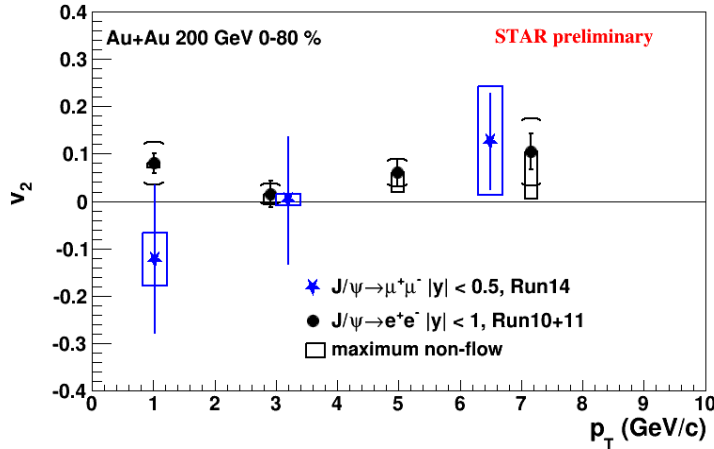


Figure 2-29: The $J/\psi \rightarrow \mu^+\mu^-$ v_2 together with results from the di-electron decay channel from Run 14 Au+Au at 200 GeV

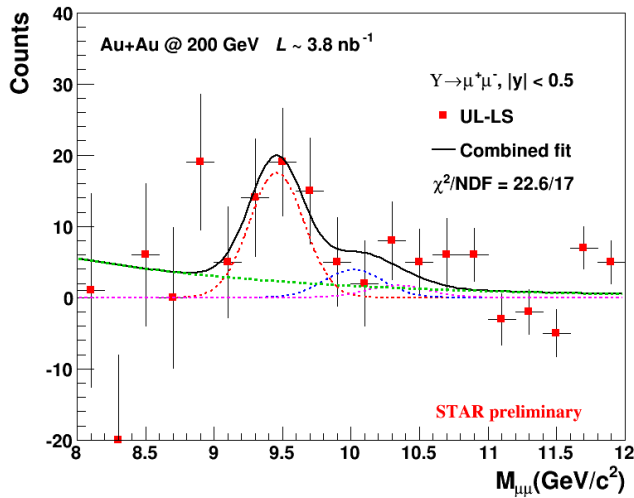


Figure 2-30: The $\mu^+\mu^-$ mass distribution after combinatorial background subtraction in the Y mass region from 30% of the full Run 14 dimuon data sample.

The Run 2015 200 GeV p+p data production is on-going. With 1/8 of the mtd triggered data produced, clear ω , ϕ , and J/ψ signals were observed in the dimuon mass distribution, as shown in Figure 2-31. A few analyses will be carried out in p+p collisions at 200 GeV including J/ψ cross section, J/ψ -h correlation, and event-activity. In addition, jet measurement might be possible with a J/ψ trigger but need more exploration.

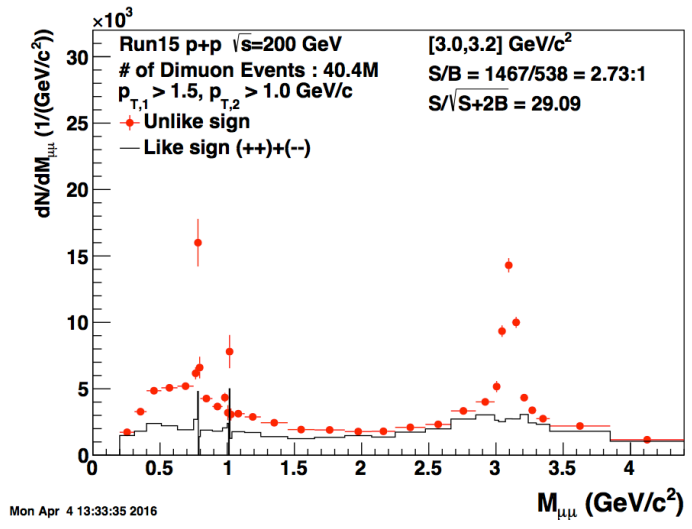


Figure 2–31: Dimuon mass distribution in Run 15 p+p collisions at 200 GeV. Clear ω , ϕ , and J/ψ signals were observed.

3 Run 16 Performance Report

3.1 The HFT Data Performance and Projections

The goal for Run 16 Au+Au 200 GeV run was to collect 2B minimum bias “good” events and $> 1 \text{ nb}^{-1}$ sampled luminosity with EMC HT and di-muon triggers within the HFT acceptance ($|V_z| < 6 \text{ cm}$), aiming for measurements of Λ_c and bottom hadrons through J/Ψ and semi-leptonic decay channels. The HFT sub-detectors of the IST and SSD were prepared for Run 16 in the fall of 2015. For the IST, more than 95% of the sensors were active throughout the Run16 data taking. This was slightly better than that in Run 15 after fixing a few problematic readout modules. For the SSD, an online common-mode noise subtraction algorithm was implemented in the firmware, allowing a major reduction in the readout noise level. The PXL detector was installed in January 2016. The PXL detector was the Run 15 refurbished detector with Aluminum cable ladders on the inner layer for improved pointing resolution over that in Run 14. Minimum bias data were taken with all the 3 HFT sub-detectors, while HT and di-muon data within the HFT acceptance taken with the PXL and IST.

A number of efforts were made to maximize the data taking efficiency in Run 16:

1. The online vertex selection scheme was optimized, improving the online vertex selection efficiency by 17% over that in Run 14 since March 16, 2016.
2. The pile-up protection for the minimum bias trigger was optimized resulting in a 30% reduced data volume and an increase in the data taking efficiency of 10%.
3. The time to bring up detectors at RHIC flattop and ramp down at beam dump was shortened from 9 and 11 minutes in Run 14 to 7 and 5 minutes in Run 16, respectively.
4. TPC ASIC and RDO were re-populated, DAQ software, online disk and network were optimized, achieving +50% faster readout speed and reduced dead time.

Due to a few setbacks, the actual number of recorded “good” minimum bias events was 1.5B, and the sampled luminosity with EMC HT and di-muon triggers was 0.8 nb^{-1} (see Figure 3–1):

1. The commissioning of the above mentioned online vertex selection scheme was later than it was originally planned.
2. A version of PXL readout firmware with reduced efficiency was used in the first 3 weeks of data taking.

The left panel of Figure 3–2 shows the estimated statistical errors with the targeted Run 16 data on the Λ_c/D^0 enhancement factor ($R_{\text{cp}}(\Lambda_c)/R_{\text{cp}}(D^0)$) for two scenarios: no enhancement and the same enhancement as Λ/K_s . With these datasets, we will be able to distinguish these two scenarios with a significance of more than 3σ . We would also be able to make the first measurement of displaced J/Ψ from bottom decays over a broad p_T region. The right panel of Figure 3–2 shows the projection on the non-

prompt J/Ψ R_{AA} with the combined Run 14 and Run 16 Au+Au data. This will offer us the first measurement of the bottom suppression factor through this channel with approximately 3σ distinguishing power from unity.

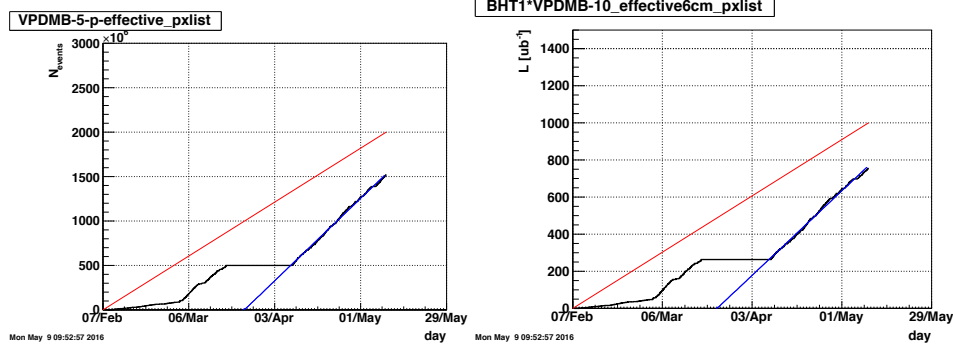


Figure 3–1: (left) Number of minimum bias events and (right) sampled luminosity with EMC HT triggers with HFT readout in Run 16 Au+Au 200 GeV run.

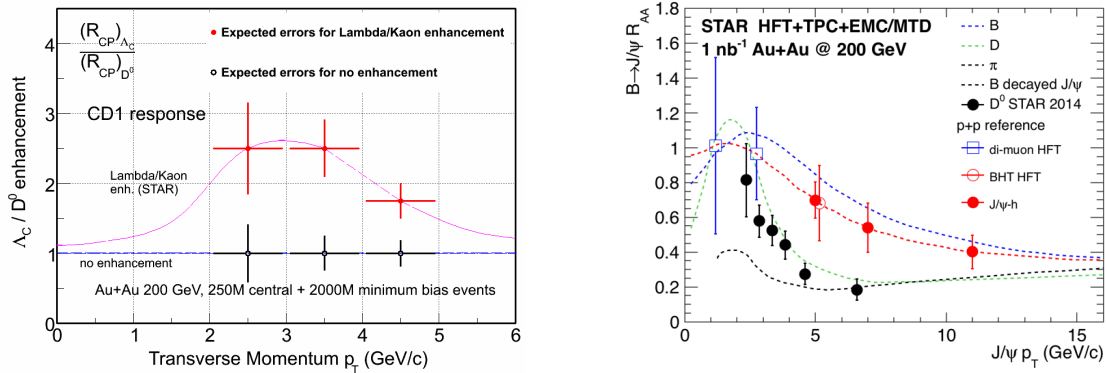


Figure 3–2: (Left) Statistical error estimation on the Λ_c/D^0 enhancement factor ($R_{CP}(\Lambda_c)/R_{CP}(D^0)$) measurement for two scenarios: no enhancement and the same enhancement as Λ/K with 2B minimum bias events and additional 250M central triggered events in Au+Au 200 GeV. (Right) Statistical error estimation on R_{AA} of displaced J/Ψ from the combined Run 14+Run 16 Au+Au data.

3.2 The MTD Data Performance and Projections

Figure 3–3 shows the accumulated effective luminosity (shown by the black curve) sampled by dimuon trigger for quarkonium versus time for 200 GeV Au+Au collisions in Run 16. For this run STAR requested CAD to reduce the luminosity and provide a modest luminosity profile as a function of time in each fill, in order to complete the physics goals with the Heavy Flavor Tracker. In addition, a 10-week run was approved for 200 GeV Au+Au instead of a 13-week run requested by STAR. By the end of the Au+Au 200 GeV run, 9 nb^{-1} effective luminosity was sampled by the MTD, which is 1 nb^{-1} less than the goal, as indicated by the red curve. In addition, a high-level

trigger (HLT) was applied during data taking of Run 2016 to select data with a possible quarkonium candidate. About 10% of the full dimuon triggered data were saved into this quarkonium HLT data stream, which will enable a fast data analysis for quarkonium physics. The plan is to present the $\Upsilon(2S+3S)/\Upsilon(1S)$ ratio with the combined Run 14 and Run 16 data at Quark Matter 2017.

Figure 3–4 shows the $\Upsilon(2S+3S)/\Upsilon(1S)$ ratio measured from 30% of the full Run 14 dimuon data sample. The precision projection with the combined Run 14 and Run 16 data is also shown.

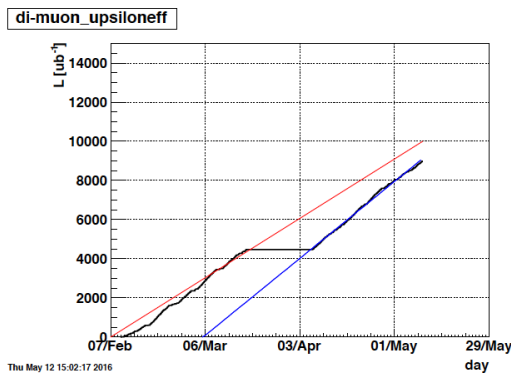


Figure 3–3: The accumulated effective luminosity (shown by the black curve) sampled by dimuon trigger for quarkonium versus time for 200 GeV Au+Au collisions in Run 16. The red curve indicates the goal.

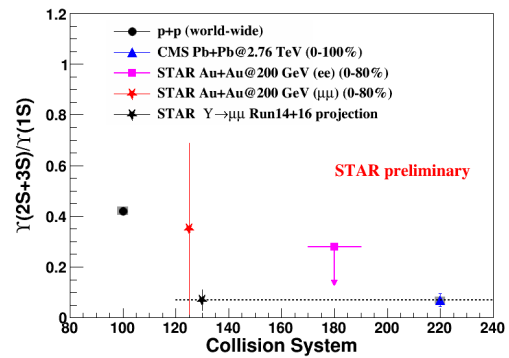


Figure 3–4: The $\Upsilon(2S+3S)/\Upsilon(1S)$ ratio measured from 30% of the full Run 14 dimuon data sample. The precision projection with the combined Run 14 and Run 16 data is also shown.

4 Run 17 Request

4.1 Polarized p+p at $\sqrt{s} = 500$ GeV

Much of our present knowledge of nucleon structure comes from deep-inelastic lepton-nucleon scattering (DIS) experiments, with a great wealth of data on the unpolarized structure of the proton available from HERA [44]. From HERA, we have learned that quarks carry 50% of the momentum of the proton, with the other half carried by gluons, which dominate for $x < 0.1$. Despite all that has been learned through DIS measurements, studying nucleon structure in a wide variety of reactions is essential in order to piece together a complete picture. Hadron-hadron interactions offer several advantages. Direct access to gluons is possible through parton-parton scattering, making the measurement of the spin contribution of the gluon to the spin of the proton a key component of the RHIC program. W-Boson production and the Drell-Yan process are both golden probes to cleanly access antiquark distributions in hadron-hadron collisions. Drell-Yan processes will become an increasingly important part of the future RHIC p+p and p+A program. Comparing observations from DIS and hadronic interactions also allows us to test the assumptions of universality across processes in describing hadron structure and hadronization within the framework of perturbative QCD (pQCD). At high energy, there remain two fundamental aspects of the nucleon partonic structure, which are rather poorly determined by experiment. One is the nature of the nucleon spin; the other is to go beyond our current simple one-dimensional picture of nucleons by correlating the information on the individual parton contribution to the spin of the nucleon with its transverse momentum and spatial distribution inside the nucleon.

4.2 The Sivers Function

A natural next step in the investigation of nucleon structure is an expansion of our current picture of the nucleon by imaging the proton in both momentum and impact parameter space. At the same time we need to further our understanding of color interactions and how they manifest themselves in different processes. In the new theoretical framework of transverse momentum dependent (TMD) parton distributions we can obtain an image in both transverse and in longitudinal momentum space (2+1 dimensions). To achieve this, one has to go beyond the conventional collinear parton picture in the hard processes. Two theoretical formalisms have been proposed to explain sizable SSAs in the QCD framework. For a spin dependence in the initial state these are: transverse momentum dependent parton distributions functions, such as the Sivers functions and transverse-momentum integrated (collinear) quark-gluon-quark correlations, which are twist-3 distributions in the initial state proton such as the Efremov-Teryaev-Qiu-Sterman (ETQS) function [45], the Twist-3 analog to the Sivers function.

The Sivers function, f_{1T}^{\perp} , describes the correlation of the parton transverse momentum with the transverse spin of the nucleon. A non-vanishing f_{1T}^{\perp} means that the parton distribution will be azimuthally asymmetric in the transverse momentum space

relative to the nucleon spin direction. The Sivers function, f_{1T}^\perp , is correlated with the ETQS functions, $T_{q,F}$, through the following relation:

$$T_{q,F}(x, x) = - \int d^2 k_\perp \frac{|k_\perp|^2}{M} f_{1T}^{\perp q}(x, k_\perp^2)|_{SIDIS}$$

In this sense, a measurement constraining the ETQS function indirectly also constrains the Sivers function. An important aspect of the Sivers effect, which has emerged from theory, is its process dependence and the color gauge invariance. In SIDIS, the quark Sivers function is manifested in association with a final state effect from the exchange of (any number of) gluons between the struck quark and the remnants of the target nucleon. On the other hand, for the virtual photon production in the Drell-Yan process, the Sivers asymmetry appears as an initial state interaction effect. As a consequence, the quark Sivers functions are of opposite sign in these two processes and this non-universality is a fundamental prediction from the gauge invariance of QCD. The experimental test of this sign change is one of the open questions in hadronic physics (NSAC performance measure HP13) and will provide a direct verification of QCD factorization. The COMPASS experiment at CERN is pursuing this sign change through Drell-Yan processes using a pion beam and new initiatives have been proposed e.g. at FNAL.

While the required background suppression for a meaningful measurement of asymmetries in Drell-Yan (DY) production are challenging, other channels can be exploited in p+p collisions, which are equally sensitive to the predicted sign change. These include prompt photons, W^\pm and Z bosons, and inclusive jets. These are already accessible with the existing STAR detector, but require continued polarized beam operations to obtain statistical significant samples at $\sqrt{s}=500$ GeV.

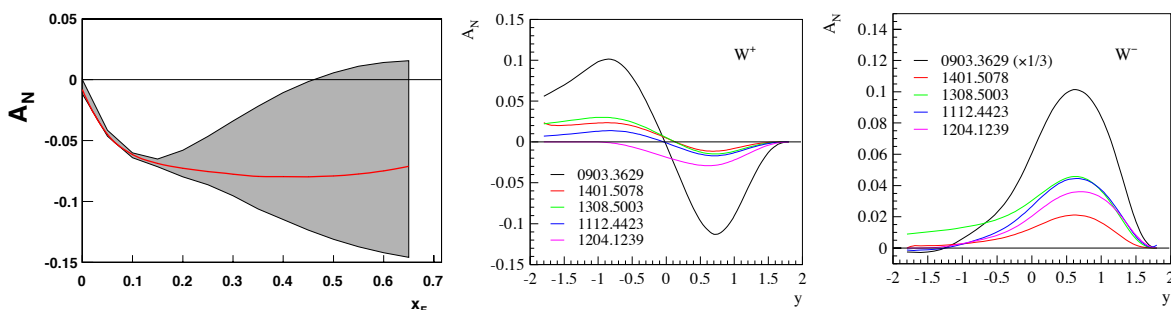


Figure 4–1: (left) Prediction for Sivers asymmetry A_N for DY lepton pair production at $\sqrt{s}=500$ GeV, for the invariant mass $4 < Q < 8$ GeV and transverse momenta $0 < q_T < 1$ GeV [46] **before any TMD evolution is applied**. (middle and right) A_N as a function of W^\pm boson rapidity at $\sqrt{s}=500$ GeV, **both are before and after TMD evolution is applied**.

Figure 4–1 shows the predicted A_N for DY (left) [47] and W^\pm (middle and right) **before and after TMD evolution is taken into account**. At this point, we must discuss a very recent theory development. The equation describing the evolution of TMDs with the hard scale of the process is well known, but it involves an evolution kernel that is itself non-perturbative in the region relevant for small transverse parton momenta. The form of the

kernel must hence be determined itself by experiment. Recent analyses of unpolarized data [48,49] have shown that the previously assumed form of the evolution kernel is most likely inadequate. This also brings into question the reliability of currently available theoretical predictions for the transverse single spin asymmetries for DY, W^\pm and Z^0 bosons including TMD-evolution, for examples see [50,51,52] and references therein. In all cases the asymmetries have been significantly reduced. We are thus currently left with large uncertainties in the prediction for the DY, W^\pm and Z^0 SSA, which can only be addressed by future measurements. Since the hard scale in typical DY events is very different from the one in W and Z production, their combination would provide an ideal setting for studying evolution effects. An indication of the magnitude of evolution effects in asymmetry measurements, where part of the effect might cancel in the ratio of the polarized over the unpolarized cross-section, can be taken from recent STAR results on the Collins effect (see Figure 4–2). Intriguingly virtually no reduction of the asymmetry is observed between measurements at $\sqrt{s}=200$ and $\sqrt{s}=500$ GeV and results are consistent with theory calculations using only collinear evolution effects [53]. The calculations are based on the transversity distributions extracted from the world SIDIS data and the extraction of the Collins FF from e+e- data [54].

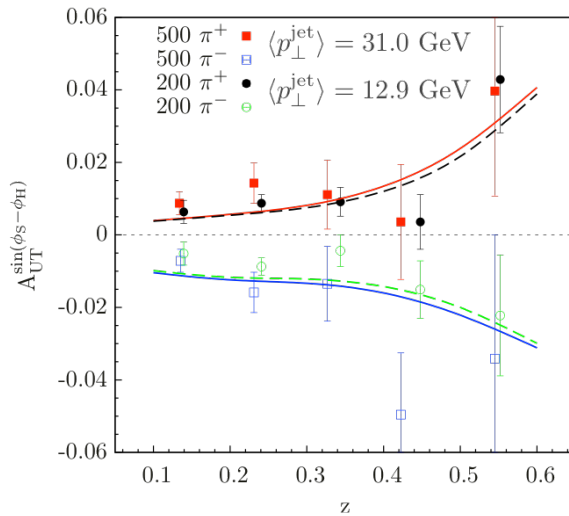


Figure 4–2 Collins $A_{UT}^{\sin(\phi_S - \phi_H)}$ as function of z for $\sqrt{s} = 200$ (blue) and 500 (red) GeV p+p collisions. The jet p_T ranges have been chosen to sample the same parton x values for both beam energies. The angular cuts, characterized by the minimum distance of the charged pion from the jet thrust axis, have been chosen to sample the same j_T values ($\sim \Delta R \times z \times p_T^{\text{jet}}$), with $\Delta R_{\text{MIN}} \times \langle p_T^{\text{jet}} \rangle = 1.3$ GeV/c.

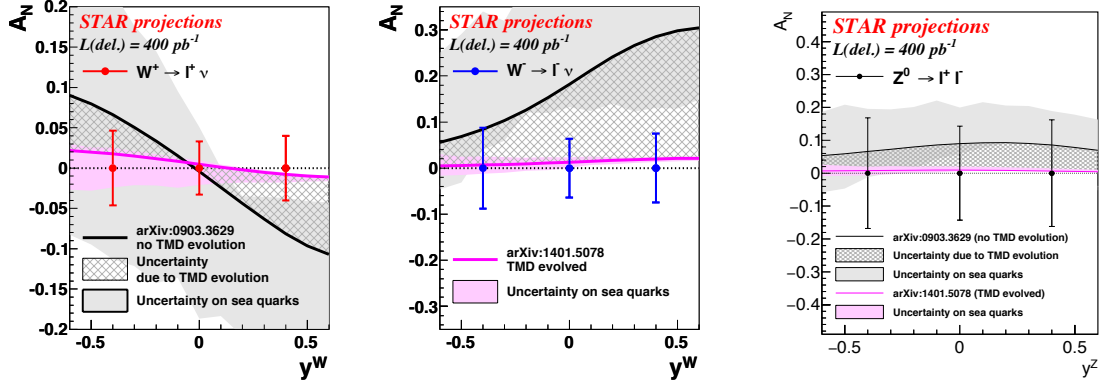


Figure 4–3: The projected uncertainties for transverse single spin asymmetries of W-bosons as a function of rapidity for a delivered integrated luminosity of 400 pb⁻¹ and an average beam polarisation of 55%. The solid light gray and pink bands represent the uncertainty on the KQ [18] and EIKV [52] results, respectively, due to the unknown sea-quark Sivvers function. The crosshatched dark grey region indicates the current uncertainty in the theoretical predictions due to TMD evolution.

W^\pm boson production is also the ideal tool to study the spin-flavor structure of sea quarks inside the proton. Such a measurement of the transverse single-spin asymmetry will provide the very first constraint on the sea quark Sivvers function in an x -range where the measured asymmetry in the \bar{u} and \bar{d} unpolarized sea quark distribution functions, as measured by E866 [55], can only be explained by strong non-pQCD contributions. At the same time, this measurement is also able to access the sign change of the Sivvers function, **if the effect due to TMD evolution on the asymmetries is in the order of a factor of 5 reduction**. Figure 4–3 shows the projected uncertainties for transverse single-spin asymmetries of W^\pm and Z^0 bosons as a function of rapidity for a delivered integrated luminosity of 400pb⁻¹ and an average beam polarization of 55%. The solid light gray and pink bands represent the uncertainty on the KQ [18] and EIKV [52] results, due to the unknown sea-quark Sivvers function. The crosshatched dark grey region indicates the current uncertainty in the theoretical predictions due to TMD evolution.

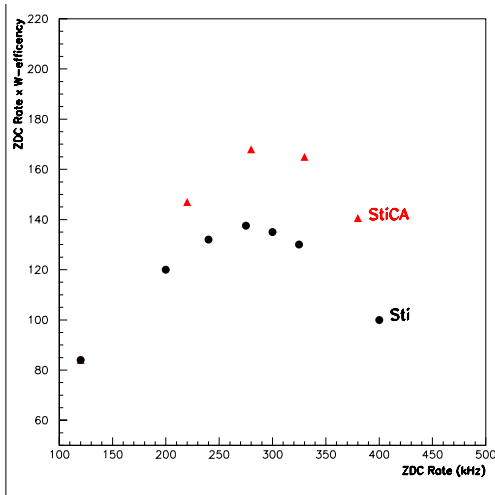


Figure 4–4: The FoM to reconstruct W-bosons in STAR as function of the ZDC raw rate. The W-boson reconstruction efficiency was obtained from the data measured in 2011 to 2013. The highest FoM is reached at a ZDC rate of 330 kHz corresponding to a luminosity of $1.5 \times 10^{32} \text{ cm}^{-2} \text{ s}^{-1}$.

In order to optimize the figure-of-merit for the W-reconstruction the luminosity throughout the fill needs to be held at a roughly constant ZDC-rate of $330 \pm 10\%$ kHz, corresponding to a RHIC p+p luminosity of $1.5 \times 10^{32} \text{ cm}^{-2}\text{s}^{-1}$. These parameters have been determined from the W-reconstruction efficiencies as function of the raw ZDC rate from the data taken in the run of the 2011 – 2013. An integrated delivered luminosity of 400 pb^{-1} corresponds to a RHIC run of 13 cryo-weeks, if the concept of a dynamic β^* squeeze through the duration of a RHIC fill is utilized. As STAR is the only running experiment in 2017 the burn of rate will be reduced due to running with a bigger β^* and having only one collision point. Therefore 3 beta squeezes throughout the fill should be sufficient to keep the luminosity in $\pm 10\%$ of $1.5 \times 10^{32} \text{ cm}^{-2}\text{s}^{-1}$.

The preferred center of mass energy for the 2017 run is $\sqrt{s} = 500 \text{ GeV}$ instead of the $\sqrt{s} = 510 \text{ GeV}$ energy used in runs 12 and 13. Analysis has shown that running the collider at 510 GeV results in non-zero tilt angles, $\varphi_{\text{pC}} = 16^\circ$ for blue and $\varphi_{\text{pC}} = 9^\circ$ for yellow, at IP12. STAR chose to run with longitudinally polarized collisions during those years and was able to remove these offsets by adjusting the spin rotators. In run 17 the spin rotators will be off as STAR plans to collide transversely polarized beams, so any residual spin tilts would result in systematic effects. For reasons that are not fully understood by CAD these significant spin tilt angles were not observed in the run 9 or 11 500 GeV collisions. As a result STAR and CAD have agreed to return to 500 GeV running for run 17.

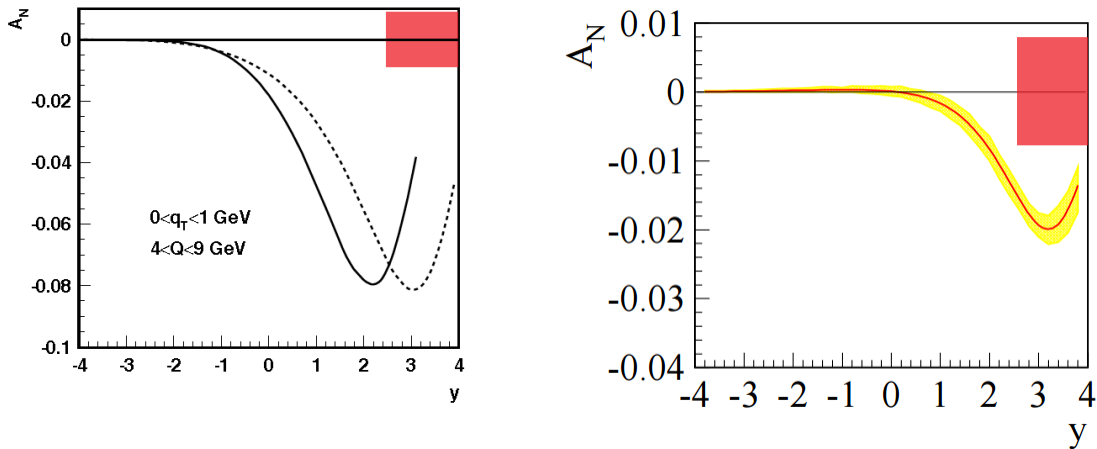


Figure 4–5: The orange square indicates the achievable statistical precision measuring one point in the rapidity-range $2.5 < \eta < 4.0$ for the asymmetry for a delivered integrated luminosity of 400 pb^{-1} in comparison to the theoretical prediction for the Sivers asymmetry A_N as a function of DY lepton-pair rapidity at $\sqrt{s} = 500 \text{ GeV}$ [56] **before any TMD evolution is applied** (left). Theoretical predictions from reference [52] for DY for $0 \text{ GeV} < p_T < 1 \text{ GeV}$ and $4 \text{ GeV} < Q < 9 \text{ GeV}$ **after** TMD evolution is applied (right). The yellow bands represent the uncertainties for the asymmetry.

The ultimate test for the TMD evolution and the sign change of the Sivers function would be to measure A_N for W^\pm , Z^0 boson and DY production simultaneously. To obtain a significant measurement of A_N for DY production, the DY leptons need to be detected between rapidities 2 and 4 for a lepton pair mass of 4 GeV and bigger (see Figure 4–5). This is a highly non-trivial measurement, as backgrounds mainly due to QCD $2 \rightarrow 2$ processes need to be suppressed by a factor of $\sim 10^7$ - 10^5 . STAR proposes a

measurement of A_N for DY during RHIC Run 17, using the FMS, its preshower and a post-shower (for details of the simulation see section 7). Figure 4–5 shows the achievable statistical precision measuring one point in the rapidity-range $2.5 < \eta < 4.0$ for the asymmetry for a delivered integrated luminosity of 400 pb^{-1} in comparison to the theoretical predicted asymmetry with and without taking TMD evolution into account.

4.2.1 The Efremov-Teryaev-Qiu-Sterman Function

Transverse single spin asymmetries in direct photon production provide a different path to access this sign change through the formalism utilizing the Twist-3 parton correlation functions. For the 2015 polarized $p+p$ run STAR installed a preshower in front of the forward electromagnetic calorimeters the FMS. This upgrade enabled a measurement of the SSA for direct photons up to $x_F \sim 0.7$ in Run 15 at $\sqrt{s} = 200 \text{ GeV}$. Figure 4–6 shows theoretical predictions and statistical and systematic uncertainties for a direct photon SSA at $\sqrt{s} = 500 \text{ GeV}$. The theoretical predictions represent a calculation based on Twist-3 parton correlation functions, $T_{q,F}$, constrained by the Siverson function obtained from a fit to the world SIDIS data [57]. At $\sqrt{s} = 500 \text{ GeV}$ the theoretical asymmetries are reduced by a factor 2 due to evolution effects compared to the one at $\sqrt{s} = 200 \text{ GeV}$. These evolution effects are currently only based on the well know evolution effects following DGLAP. The comparison of the 200 GeV and 500 GeV results can reveal if also in the case of the Twist-3 formalism evolution effects there are additional evolution effects as for TMDs. Due to the electromagnetic nature of the process the individual parton densities are weighted with the respective quark charge e_q^2 , therefore the direct photon asymmetries are mainly sensitive to the u -quark Twist-3 correlation functions (in analogy to Drell-Yan, which is mainly sensitive to the up quark Siverson function).

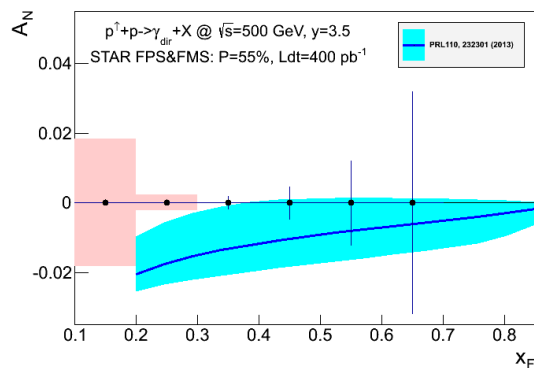


Figure 4–6: Statistical and systematic uncertainties for the direct photon A_N after background subtraction compared to theoretical predictions from Ref. [57] for $\sqrt{s} = 500 \text{ GeV}$ as measured by STAR. If the correlation between the Twist-3 correlation functions and the Siverson function as described in [Eq.2-1] would be violated the asymmetries would have the same magnitude but being positive.

The ultimate test for the TMD factorization, evolution and the relation between the Siverson function and the Twist-3 correlation function is to measure A_N for W^\pm , Z^0 boson, DY production and direct photons. Table 4.1 summarizes the different observables and their sensitivity to the following main questions to be addressed with the transversely polarized $p+p$ run in 2017:

- Can the sign change of the Sivers function between SIDIS and DY-production be experimentally verified?
- What are the effects on A_N due to TMD evolution?
- Do sea quarks have significant Sivers and Twist-3 ETQS functions?
- Can the relation between the Sivers function and the Twist-3 ETQS distribution function be experimentally verified?
- Can the evolution of the Twist-3 ETQS distribution functions be experimentally constrained?

It is especially noted that answers to these questions are critical for the effective planning of the physics program of an electron-ion-collider.

	$A_N(W^{+/-}, Z^0)$	$A_N(DY)$	$A_N(\gamma)$
Sensitive to Sivers effect non-universality through TMDs	Yes	Yes	No
Sensitive to Sivers effect non-universality through Twist-3 $T_{q,F}(x,x)$	No	No	Yes
Sensitive to TMD or Twist-3 evolution	Yes	Yes	Yes
Sensitive to sea quark Sivers or ETQS function	Yes	Yes ($\times 10^{-3}$)	No
Detector upgrade needed	No	Yes FMS post-shower	No
Biggest experimental challenge	Integrated luminosity	Background suppression Integrated luminosity	----

Table 4.1: Summary of all the processes accessible in STAR to measure access the sign change of the Sivers function.

4.3 Interference Fragmentation, Collins, Collins-like and Sivers Functions

STAR has collected 2.4 times as much transversely polarized data at 200 GeV in the 2015 RHIC run compared to the 2012 RHIC run, and will record over an order of magnitude more data at 500 GeV in 2017 than in 2011. This will enable far more detailed, multi-dimensional examination of the asymmetries probing different combinations of several transverse momentum dependent PDFs and FFs, i.e., transversity x Collins, transversity x interference fragmentation functions (IFF) and linearly polarized gluons. As discussed in Section 4.2, preliminary STAR Collins asymmetries at 200 and 500 GeV are consistent with x_T scaling and with model calculations based on SIDIS and e^+e^- , assuming robust TMD factorization in p+p. Thus, precision measurements of

Collins asymmetries may provide an experimental test of TMD factorization-breaking and universality.

Significant asymmetries have been measured in the Interference Fragmentation and Collins Function channel in the Run 11 $\sqrt{s} = 500$ GeV data. Asymmetries sensitive to the gluon Sivers function and gluon linear polarization (Collins-like) have also been measured for the first time in hadronic collisions. The transverse data in Run 11 (25 pb^{-1}) were initially recorded to estimate the systematic uncertainties in the helicity asymmetries from residual transverse components of the polarization and A_{TT} . A high luminosity run at $\sqrt{s} = 500$ GeV will provide the opportunity to increase the precision of the measurements in all of these channels and to make a high precision measurement of the Twist-3 ETQS function for gluons through A_N for inclusive jets. Given that the same relation between the Twist-3 ETQS function and the Sivers function for quarks exists also for gluons, a measurement constraining the ETQS function for gluons also constrains the gluon Sivers function (for more details see [58]). It is noted that a high precision measurement of the gluon Sivers function in the Twist-3 formalism through A_N for inclusive jets at mid-rapidity will be complementary to the results by the A_{NDY} collaboration done at $\sqrt{s}=500$ GeV for $\eta>3$ [59]. The uncertainties for all these measurements will shrink by a factor 4 with the proposed Run 17 (see Figure 4–7 and Figure 4–8). It is noted that for some of these observables Run 15 will provide the first statistical significant enough data set at $\sqrt{s} = 200$ GeV.

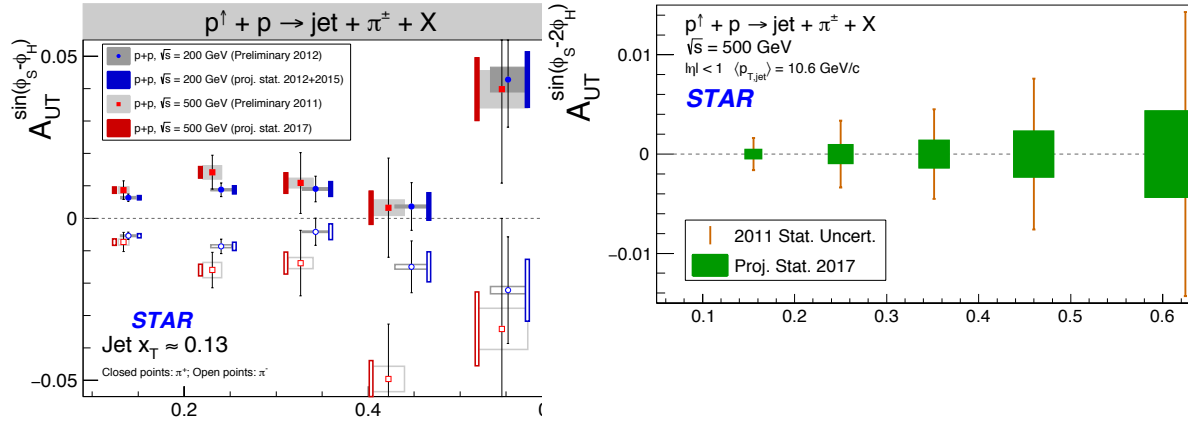


Figure 4–7: The improved statistical uncertainties for $A_{UT}^{\sin(\phi_s - \phi_h)}$ sensitive to the Collins effect and quark transversity (left) and $A_{UT}^{\sin(\phi_s - 2\phi_h)}$ sensitive to gluon linear polarization (right), as function of z for charged pions in jets at $0 < \eta < 1$ measured in STAR for transversely polarized p+p collisions at $\sqrt{s} = 200$ GeV (Run 12 to Run 15) and 500 GeV (Run 11 to Run 17), respectively.

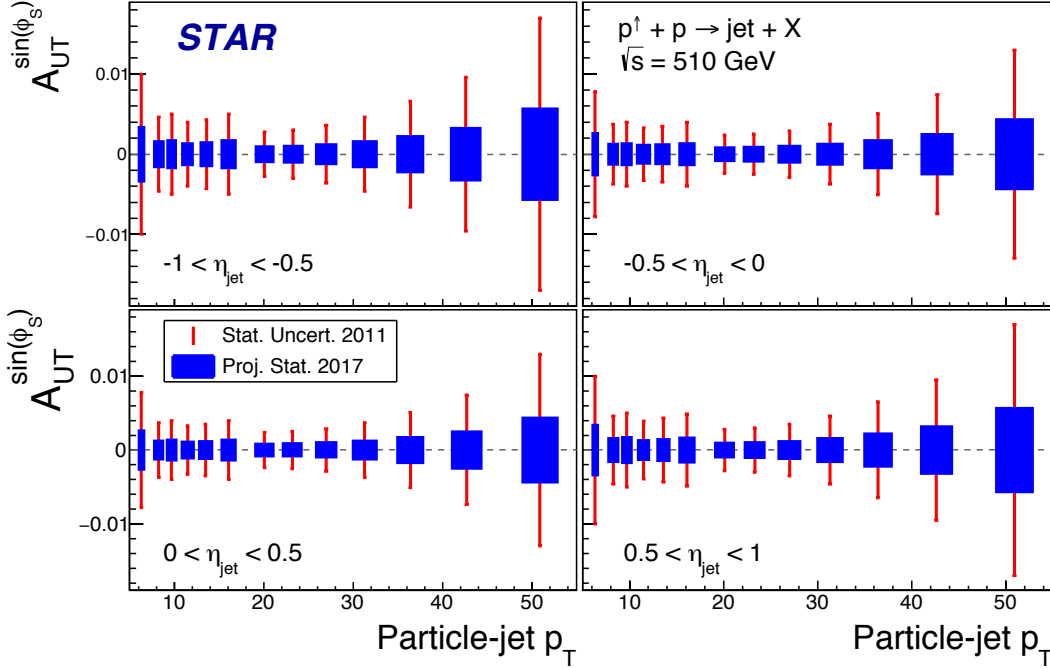


Figure 4–8: The improved statistical uncertainties for $A_{UT}^{\sin(\phi_s)}$ sensitive to the Twist-3 ETQS function for gluons, as function of particle-jet p_T for 4 bins in rapidity measured in STAR for transversely polarized $p+p$ collisions at 500 GeV (Run 11 to Run 17)

4.4 Using Ultra Peripheral Collisions to Access the Generalized Parton Distribution Function, E_g :

The formalism of generalized parton distributions provides a theoretical framework, which allows some answers to the above questions [60]. Exclusive reactions in DIS, i.e., deeply virtual Compton scattering, have been mainly used to constrain GPDs. RHIC, with its capability to collide transversely polarized protons at $\sqrt{s}=500$ GeV, has the unique opportunity to measure A_N for exclusive J/ψ in ultra-peripheral $p^\dagger+p$ collisions (UPC) [61]. The measurement is at a fixed Q^2 of 9 GeV^2 and $10^{-4} < x < 10^{-1}$. A nonzero asymmetry would be the first signature of a nonzero GPD E for gluons, which is sensitive to spin-orbit correlations and is intimately connected with the orbital angular momentum carried by partons in the nucleon and thus with the proton spin puzzle. Detecting one of the scattered polarized protons in “Roman Pots” (RP) ensures an elastic process. The event generator SARTRE [62], which also describes well the STAR results for ρ^0 production in UPC in Au+Au collisions, has been used to simulate exclusive J/ψ production in $p^\dagger+p$ UPC. The acceptance of the STAR RP PHASE-II* system in t , the momentum transfer between the incoming and outgoing proton, matches well the t spectrum in UPC collisions (see Figure 4–9). To select the J/ψ in UPC, at least one of the two protons are required in the STAR RPs. The J/ψ is reconstructed from its decay electrons, in the STAR EMCals between $-1 < \eta < 2$. Accounting for all trigger and reconstruction efficiencies the total number of J/ψ 's for a delivered luminosity of 400 pb^{-1}

¹ is $\sim 11k$ in Run 17. This will result in 3 bins of equal statistics in A_{UT} as a function of t and a ΔA_{UT} of $\pm 4\%$ in all three bins.

This first measurement was done during 2015 pA run. Here the Au emits the virtual photon which scatters off the p^\uparrow , providing an advantage in rate enhanced by Z^2 compared to ultra-peripheral $p^\uparrow+p$ collisions at the same $\sqrt{s}=200$ GeV. The process where the p^\uparrow emits the virtual photon can be suppressed by requiring a hit in the RP in the proton direction. The total number of J/ψ 's in run 2015 is $\sim 3k$ for the Au as photon source with a background of $\sim 1.3k$ for the p^\uparrow as photon source.

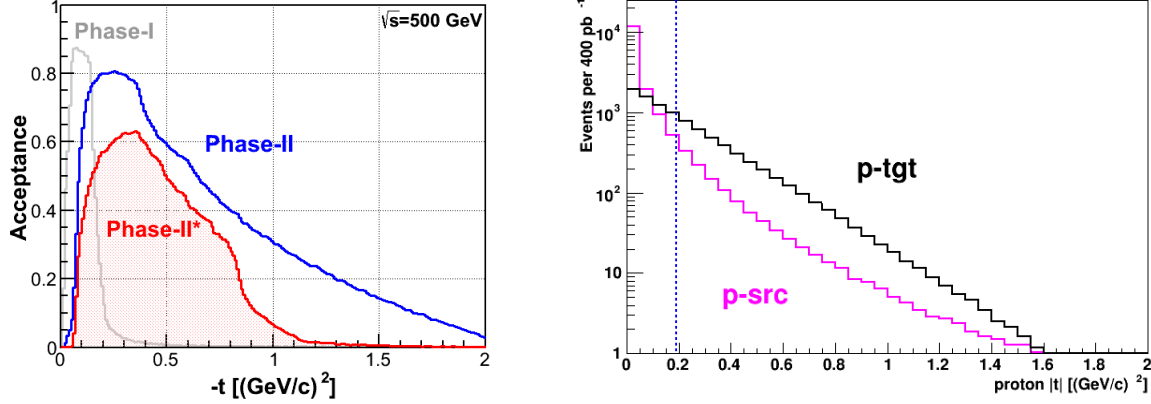


Figure 4–9: (left) Acceptance of protons in exclusive p+p scattering at $\sqrt{s} = 500$ GeV as function of t for a possible future upgrade (blue) and the STAR set up since 2015 (PHASE-II*) (red) configuration. The acceptance for the original STAR Phase-I setup is also shown (grey). (right) The t spectrum of the proton emitting the photon (pink) as well as the one from the scattered proton (black).

4.5 Gluon Fragmentation Functions

In spite of the remarkable phenomenological successes of QCD, a quantitative understanding of the hadronization process is still one of the great challenges for the theory. Hadronization describes the transition of a quark or gluon into a final state hadron. It is a poorly understood process even in elementary collisions. Often, the hadronization process is characterized in terms of fragmentation functions. For many years, fragmentation functions were extracted from analyses of hadron yields in e^+e^- collisions [63]. More recently, they have been extracted from global analyses of hadron yields in e^+e^- , SIDIS, and pp data [64,66]. In addition to their fundamental importance, fragmentation functions play a central role, for example, in the extraction of helicity PDFs and TMDs and studies of medium modifications of hadron production at RHIC and the LHC. The relative uncertainties on $D_g^{\pi^+}$ at $Q^2 = 10$ GeV² in the most recent global analysis are about 25% up to $z \sim 0.5$ and quickly increase toward larger z values [66]. This comes about because the e^+e^- and SIDIS data only provide indirect constraints on the gluon fragmentation and a tension exists between the high- p_T inclusive π^0 cross section measurements from PHENIX and ALICE.

Measurements of hadron distributions within jets in 500 GeV pp collisions provide an excellent opportunity to enhance our knowledge of gluon fragmentation functions. About half of the mid-rapidity jets with $p_T < 10$ GeV/c arise from gluon-gluon scattering, and less than 10% arise from quark-quark scattering. It has long been recognized that the hadron distributions within jets produced in pp collisions are closely related to the fragmentation functions that have typically been measured in e^+e^- collisions and SIDIS. But only within the past year [65] has the quantitative relationship been derived in a form that enables measurements of identified hadrons in jets in pp collisions to be included in fragmentation function fits on an equal footing. The key feature of this type of observable, in comparison to the inclusive pion yields that have been used in recent global analyses [64, 66], is the possibility to determine the relevant momentum fraction z experimentally as the ratio of the hadron to the jet transverse momentum.

This development motivated STAR to initiate a program of identified particle fragmentation function measurements using mid-rapidity pp jet data at 200 and 500 GeV that were recorded in 2011, 2012, and 2015. Measurements of low- p_T (~ 7 GeV/c) jets in 500 GeV collisions will provide constraints utilizing the most gluon-rich probes available at RHIC. The comparison between measurements of higher- p_T jets in 500 GeV collisions and low- p_T jets in 200 GeV collisions will probe the fragmentation functions at the same x_T but different Q^2 . The 200 GeV results will then extend the sensitivity to higher x_T , and also provide a baseline to look for changes in the hadronization process between pp and $p+Au$ collisions. These measurements require large volumes of minimum bias events (to avoid trigger bias) in the region $|\eta_{\text{jet}}| < 0.4$, where STAR has excellent high- p_T particle identification over the entire jet cone from the combination of TPC dE/dx and TOF. Unfortunately, the only suitable 500 GeV data set available to date is from the short 2011 run because very little bandwidth was devoted to minbias events during the long 510 GeV runs in 2012 and 2013.

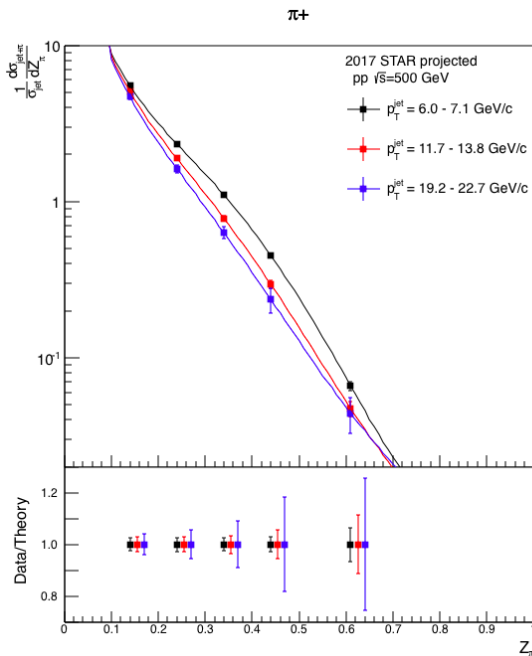


Figure 4–10: Anticipated Run 17 precision for identified π^+ within jets at $|\eta_{\text{jet}}| < 0.4$ in 500 GeV pp collisions for three representative jet p_T bins. The data points are plotted on theoretical predictions based on the DSS14 pion fragmentation functions [66]. π^- will be measured with similar precision, while kaons and (anti)protons will also be measured, over the range from $z < 0.5$ at low jet p_T to $z < 0.2$ at high jet p_T , with uncertainties a factor of ~ 3 larger than those for pions.

STAR proposes to record over an order of magnitude more minbias-triggered jets in 500 GeV pp collisions during Run 17 than we recorded during 2011. Figure 4–10 shows the precision that is anticipated for identified π^+ for three representative jet p_T bins with the Run 17 data. (We expect to measure the pion yields for 8 different jet p_T bins overall.) Similar precision will be achieved for identified π^- in jets. Identified kaon and (anti)proton yields will also be obtained, with uncertainties that will be larger than those for pions by a factor of ~ 3 , for $z < 0.5$ at low jet p_T to $z < 0.2$ at high jet p_T . Identified hadron yields will also be measured multi-dimensionally vs. j_T , z , and jet p_T , which will provide important input for unpolarized TMD fits.

4.6 Precise measurement of the W-boson cross-section ratio

The STAR experiment has previously measured the production cross-sections for Z^0 , W^+ , and W^- bosons at $\sqrt{s} = 500$ GeV, as well as the ratio $R_W = \sigma_{W^+}/\sigma_{W^-}$. [67]. The ratio is sensitive to the flavor asymmetry of the antiquark sea in the Bjorken- x range $0.1 < x < 0.3$ probed in these measurements. Drell-Yan measurements have measured a large asymmetry in this x -region. Precision measurement of R_W at STAR can provide independent constraints on the flavor asymmetry that are free from the assumption of charge symmetry in the interpretation of the Drell-Yan measurements. Complementary measurements of R_W at the LHC are sensitive to considerably smaller Bjorken- x values, because of the considerably higher center-of-mass energies. Since the initial publication, STAR has recorded additional data in RHIC runs in 2011, 2012, and 2013. Figure 4–11 shows preliminary results from the analysis of 2011 and 2012 data, corresponding to an integrated luminosity of 102 pb^{-1} . The results are limited by the statistical uncertainties. Data obtained in the RHIC run in 2013 amount to approximately 300 pb^{-1} . The measurement of the single-spin asymmetry A_N for W bosons for the RHIC run in 2017 requires that new data, corresponding 400 pb^{-1} , be acquired. Combined analysis of these samples for the spin-independent ratio R_W is anticipated to yield results with statistical uncertainties that are a factor three better than those in Figure 4–11, to the level where the statistical and systematic uncertainties will have similar sizes. At this level of accuracy, the results provide impactful constraints as seen by comparison with the theoretical predictions and their uncertainties shown in Figure 4–11.

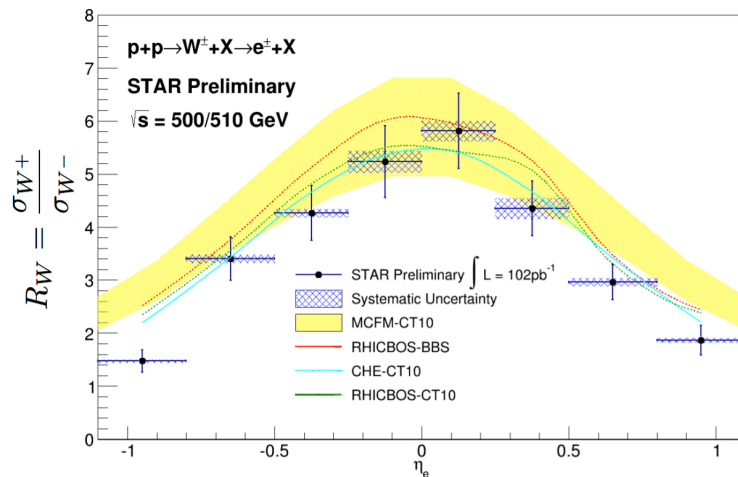


Figure 4–11 Preliminary results on the ratio R_W in the production of W bosons versus electron pseudorapidity. The data were obtained in RHIC runs in 2011 and 2012 from a sample corresponding to an integrated luminosity of 102 pb^{-1} .

4.7 Central Exclusive Process in Diffractive p+p via Double Pomeron Exchange

The start of data taking at Hall-D@JLab, the flow of new results from LHC-b and the expected start of data taking at Belle-II in 2018 constitute an extremely vibrant world-wide effort to search for exotic states, i.e. tetraquarks, pentaquarks and glueballs. STAR has the unique opportunity to join this effort by tagging on diffractive processes at high energies. These diffractive events are believed to be mediated by exchange of a color singlet object, historically referred to as Pomeron. In the context of QCD, Pomeron exchange can be interpreted as the exchange of a system of gluons. The double Pomeron exchange (DPE) process has been regarded as one of the potential channels of glueball production. It is predicted that two of the gluons in the DPE process could merge into a mesonic bound state without a constituent quark, resulting in a glueball in the central diffractive production.

Lattice QCD calculations[68] have predicted the lowest-lying scalar glueball state in the mass range of 1500-1700 MeV/ c^2 , and tensor and pseudoscalar glueballs in the 2000-2500 MeV/ c^2 range. Unfortunately the width of these states is difficult to predict, making quantitative sensitivity studies difficult to perform. Experimentally measured glueball candidates for the scalar glueball states are the $f_0(1500)$ and the $f_0(1710)$ in central production as well as other gluon-rich reactions such as $p\bar{p}$ annihilation, and radiative J/Ψ decay [69]. The glueballs are expected to be intrinsically unstable and decay in diverse ways, yielding typically two or more mesons. The $f_0(1710)$ dominantly decays into K^+K^- and $f_0(1500)$ into $\pi^+\pi^-\pi^+\pi^-$. One of the challenges in identifying a glueball state unambiguously lies in the difficulty of isolating a glueball state from the conventional meson state that shares the same quantum numbers. To identify that the process is from DPE process rather than Reggeon exchange requires observing suppression of ρ meson in the process, since ρ cannot be formed from two states with $J^{PC} = 0^{++}$. The other filter for enhancing gluon-gluon channel in DPE process is the δp_T -“filter” [70], in which small momentum transfer processes enhance gluon-gluon kinematic configurations since the gluons can flow directly into the final state in the process with small momentum transfer t .

The Roman Pot (RP) system is the main detector system used to identify and characterize diffractive process at STAR through a detection of the forward protons, which stay intact after the collision took place. The RP system at STAR was utilized for successful data taking in Run 9 and then reconfigured and moved to a new location, closer to the interaction region between DX and D0 magnets, to allow concurrent running with the rest of the RHIC program. To accomplish that a new vacuum chamber at that new location had been designed and fabricated to accommodate the RP system. The new system has been successfully commissioned in Run 15 and used for data taking. This gave the STAR experiment the unique opportunity to detect the protons scattered at small angles in the elastic scattering process and a diffractive Central Exclusive Production (CEP) process $p+p \rightarrow p+M_X+p$, where the system M_X is identified and measured in the TPC and ToF. Tagging on those protons, detected in the Roman Pots, selects processes in which the protons stay intact and the exchange has the

quantum numbers of the color singlet, thus enhancing the probability of measuring reactions where colorless gluonic matter dominates the exchange.

Given this new RP system, it was possible to acquire large data samples of central production events. The new RP system has been used to collect over 800M triggers including 600M central diffraction trigger events in $p+p$ at $\sqrt{s} = 200$ GeV in Run 15. The data sample is expected to yield a first measurement of exclusive centrally produced system at the RHIC energies. The preliminary study shows clearly identified scalar and tensor f mesons in the CEP process in the $\pi^+\pi^-$ and K^+K^- as shown in the invariant mass distribution as shown in Figure 4–13, confirming the detector system and triggers performed as expected.

At the higher energies, Reggeon(R)-Reggeon and Reggeon-Pomeron(P) contributions are expected to be more suppressed while Pomeron-Pomeron contribution remains constant since the expected cross-sections in the central diffractive processes are $\sigma(RR)\sim s^{-1}$, $\sigma(RP)\sim s^{-0.5}$, $\sigma(PP)\sim s^{-0.1}$. The t range measured in the RP system is limited by the beam aperture in the machine and also kinematics. Running at $\sqrt{s} = 510$ GeV will extend t range significantly by ~ 6.5 since $t\sim p^2$ as shown in Figure 4–12. The wider t ranges give more dynamic range for PP coupling dynamics and also better access to the higher mass region due to more phase-space availability, which both are important additional benefits in studying dynamics of particle production in CEP.

At $\sqrt{s} = 510$ GeV in Run 17, 500M central diffractive trigger data is proposed to be collected, which can be accumulated at 150 Hz data taking rate for 13 weeks of $p+p$ running. More stringent trigger condition to veto non-diffractive events and a proposed higher data collection rate will give more statistics for final CEP data sample in wider kinematic range than Run 15 at $\sqrt{s} = 200$ GeV. The data set can add a significant statistics especially at higher mass region. The contamination of rapidity gap by in the non-diffractive events in the same bunch crossing is significantly increasing due to the projected high luminosity: at $L \sim 1.5 \times 10^{32} \text{ cm}^{-2} \text{ s}^{-1}$ the expected contamination is ~ 0.95 , and with the condition, the central diffraction trigger is expected to run with a pre-scale of $\sim 1-2$ at the luminosity. The inefficiency due to pile-up events can be accurately estimated and corrected using zero-bias events as done for the data taken in Run 15 at $\sqrt{s} = 200$ GeV.

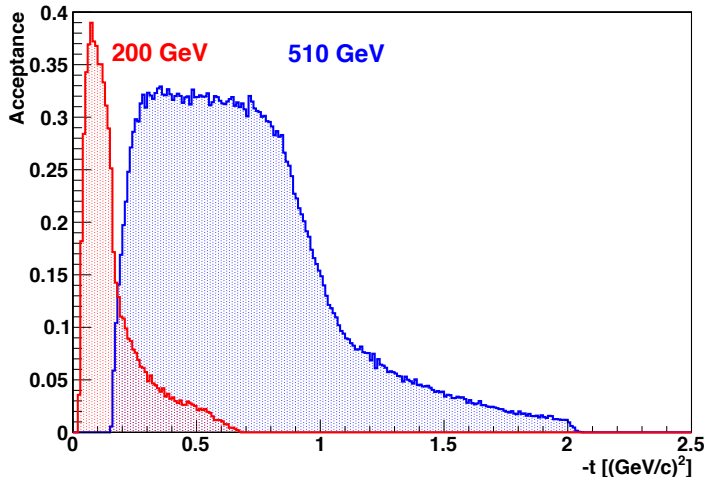


Figure 4–12: Acceptance of protons from double Pomeron exchange processes in $p+p$ at $\sqrt{s} = 200$ and 510 GeV as function of squared four momentum transfer t .

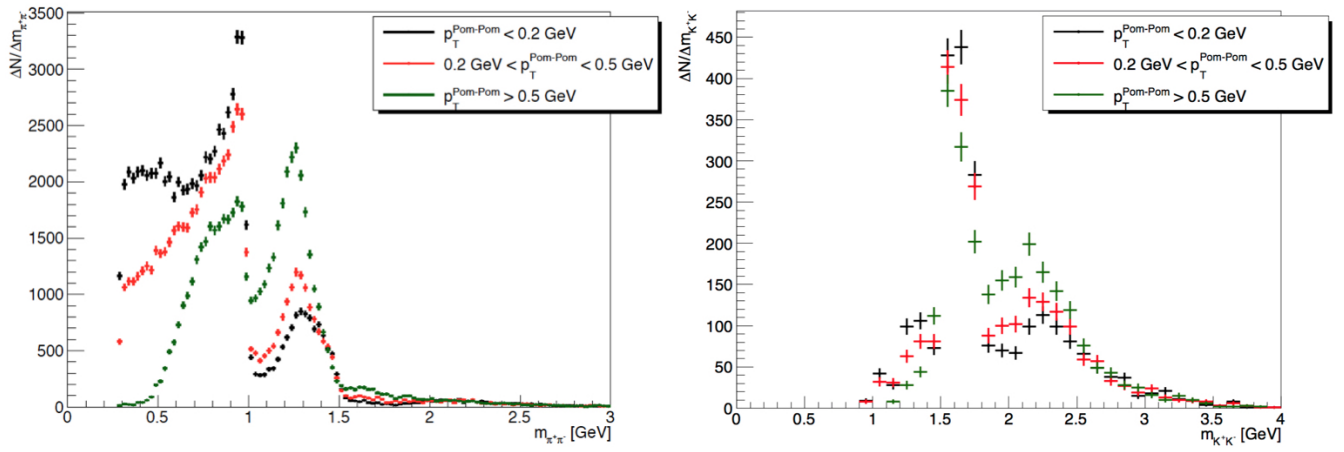


Figure 4–13 Invariant mass distributions of $\pi^+\pi^-$ (left) and K^+K^- (right) as function of a sum of the exchanged momentum (Pomeron) of two protons in CEP at $\sqrt{s} = 200$ GeV.

4.8 Heavy Flavor cross-section measurements in $\sqrt{s} = 500$ GeV p+p Collisions

A high statistics p+p 500 GeV dataset will allow us to perform high precision measurements of heavy flavor hadron production and confront these with results pQCD calculations. In the meantime, these measurements can be extrapolated to 200 GeV and be used as precision references for heavy ion collisions, e.g. high p_T D-mesons, high p_T J/Ψ and Y etc.

In the Run 11 STAR accumulated 22 pb^{-1} luminosity of data with the BHT1 trigger (DSM threshold=18, $E_T \sim 4.2$ GeV) for p+p collisions at 500 GeV. Based on this sample, we have extended the D-meson and J/Ψ measurements up to 18-20 GeV/c, and have studied heavy-flavor triggered correlations (D-h, J/Ψ -h), $\Psi(2S)$ production cross-section and J/Ψ polarization. A sample of significantly more statistics in year 2017 will greatly improve the precision of all these measurements.

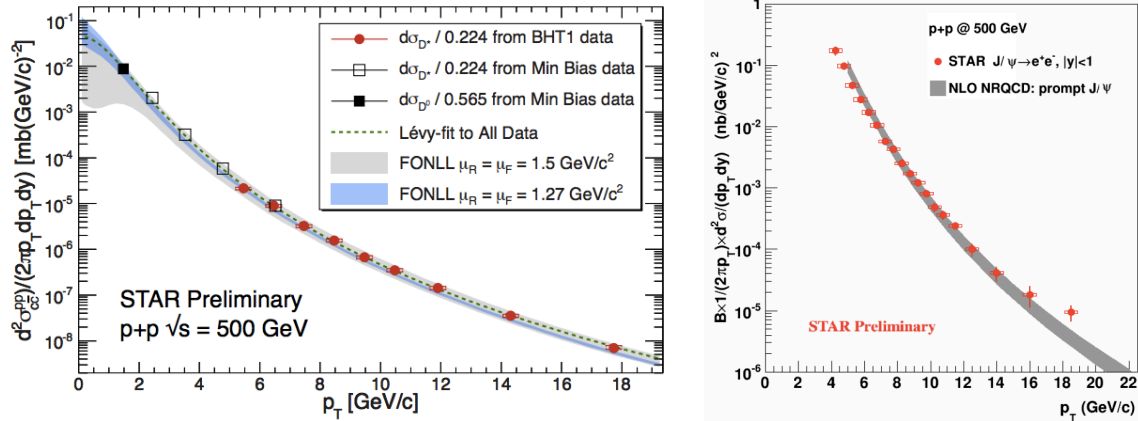


Figure 4-14: (left) Measured charmed hadron production and (right) inclusive J/ψ production cross-section compared to pQCD calculations in p+p 500 GeV collisions.

The rate of the lower level high tower trigger without vertex cuts will be too high to accommodate in the high luminosity 2017 runs. Consequently, we will rely on a high tower trigger with an $E_T \sim 5.6$ GeV threshold to sample the full delivered luminosity. In year 2013 the mid-rapidity bandwidth was prioritized to the W and jet physics program, resulting in a highly pre-scaled BHT2 and only 10 pb^{-1} sampled luminosity. In Run 17 we would like to run the BHT2 trigger with no prescale and sample ~ 300 pb^{-1} luminosity.

In addition, with the full MTD system, we would like to measure different Y states [$Y(1S)$, $Y(2S)$, $Y(3S)$] through dimuon decays in 500 GeV p+p collisions. The goal is to obtain different Y states ratio in this system since a higher collision energy is beneficial for Y measurements due to a higher luminosity and a higher production cross section. About 1100 $Y(1S+2S+3S)$ will be observed with 360 pb^{-1} sampled effective luminosity. A tighter trigger time window cut might be implemented with allocated 150-200 Hz data acquisition rate for the MTD triggers. This will result in lower trigger efficiency for Y .

4.9 Au+Au Collisions at 62.4 GeV

Au+Au collisions $\sqrt{s_{NN}} = 62$ GeV should produce a medium where the initial energy densities and temperatures are closer to the critical values than those created at higher collision energies. Theoretical calculations suggest that systems sitting near the transition temperature result in a stronger early-time coupling, see for example Figure 4–15. Sensitivity to this coupling should therefore be enhanced at 62.4 GeV relative to top RHIC and LHC energies, even though they result in initially hotter fireball temperatures potentially providing key new information on how partons interact with the QGP. Jet measurements could be used to extend the study of the temperature to values much lower than those achievable at top RHIC and LHC energies. As can be seen in Figure 4–15 in the lever arm of the 62.4 GeV measurements, combined with results from top RHIC energies and from the LHC, will provide crucial insight into the physics of jet-medium interactions. In addition the very steep initial p_T spectrum of charm quarks at this energy is predicted to make heavy flavor partons especially sensitive to flow effects.

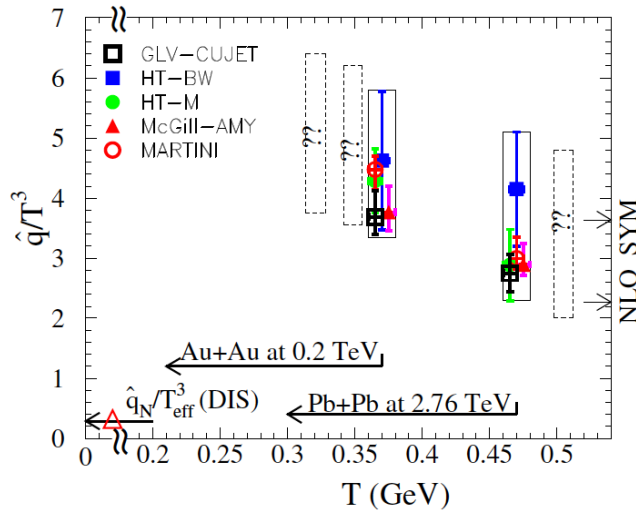


Figure 4–15: \hat{q}/T^3 as a function of the temperature T for initial quark jets with energy $E = 10$ GeV⁷¹. The dashed boxes show the expected values for $\sqrt{s_{NN}} = 63, 130,$ and 5500 GeV.

Taken in combination the existing data from Au+Au collisions at 62.4 GeV data provide strong evidence of the formation of the QGP also at this lower beam energy. For instance, the flow of light flavor hadrons is significant with centrality and p_T trends similar to that at $\sqrt{s_{NN}} = 200$ GeV and the measured nuclear modification of high p_T light hadrons is also similar to that at top energies. However for p_T below ~ 6 GeV/c there is a distinct mass dependence of the measured R_{cp} , as shown in Figure 4–16. This is believed to be due to the so-called Cronin enhancement effect competing with the energy loss of partons to the medium. Cronin enhancement was first observed in p+A collisions at lower beam energies, and has also been reported in d+Au collisions at RHIC energies for many particle species including electrons from heavy-flavor decays. This enhancement grows with both increasing particle mass and decreasing collision energies. Our measured R_{cp} of electrons from heavy flavor hadron decays (so called non-photonically electrons, NPE) also appears to reveal an enhancement for $p_T < 5$ GeV/c, see Figure 4–17, in agreement with the previously described mass dependence. These results most likely

emerge from an intricate interplay of energy loss, thermalization, the Cronin effect, and other initial state effects.

The measured large elliptic flow of NPE in Au+Au collisions at 200 GeV⁷² is similar to that of the light quarks. However, the analysis of the Run 10 NPE v_2 Au+Au collisions at $\sqrt{s_{NN}} = 62.4$ GeV reveals a difference. The STAR preliminary measurements at 62.4 GeV, shown in Figure 4–18, indicate that the NPE v_2 is small and consistent with zero. These results, and those of the NPE R_{CP} , are consistent with those published by PHENIX[73]. However, the NPE data from both experiments suffer from large statistical uncertainties. It is therefore imperative that we collect higher precision data in order to allow for a detailed exploration of these various interactions. In particular it has been proposed that the heavy-flavor coupling to the medium is strongest in the pseudocritical region [74].

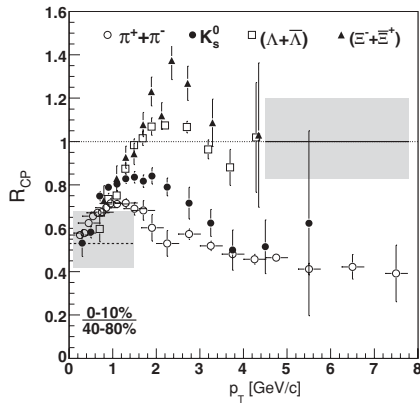


Figure 4–16: R_{CP} for various particles at 62.4 GeV [75].

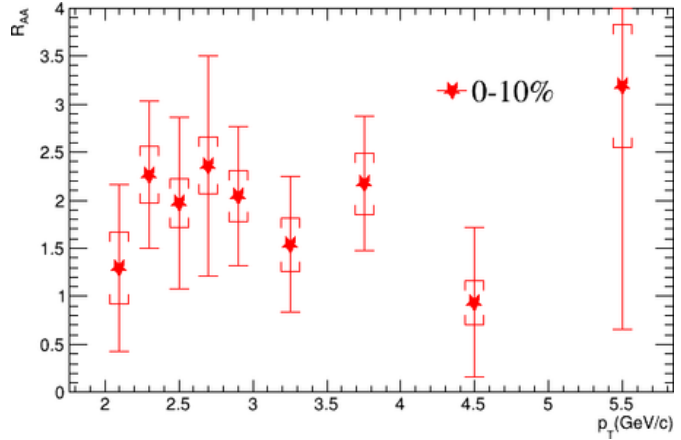


Figure 4–17: Preliminary NPE R_{AA} for 0-10% Au+Au $\sqrt{s_{NN}} = 62.4$ GeV.

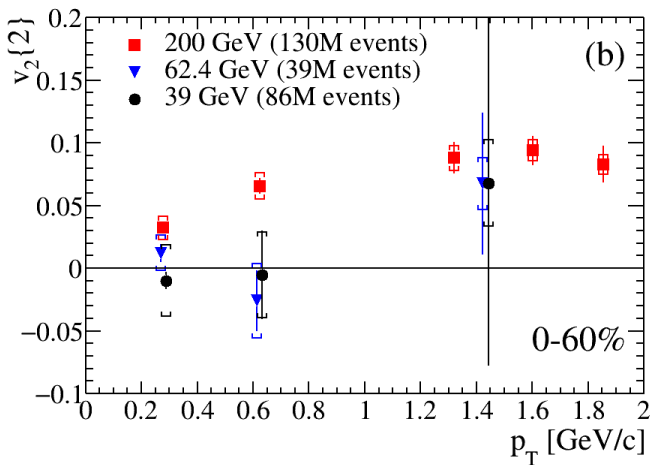


Figure 4–18: Preliminary Au+Au measurements of NPE in 39, 62.4 ; 200 GeV.

4.9.1 Non-photonic Electron Elliptic flow and High p_T Suppression

With 4 weeks for Au+Au physics beams we expect to collect 1B minimum-bias events within the TPC acceptance. For comparison during run 10 STAR recorded only 67.3M good minimum bias (0-80%) events. Although the charm cross-section drops significantly with decreasing energy and is a factor of 5 lower at 62.4 GeV than at 200 GeV, 1B events should allow significant improvement on the existing measurements. With the removal of the HFT and reinstallation of the old beam-pipe after Run 15, the material budget and NPE measurement efficiency will be returned to that of Run 10. We therefore expect a factor 4 improvement in statistical errors alone for our NPE measurements.

Figure 4–19 shows the projections for NPE v_2 from 1B minimum bias events. We will be able to measure elliptic flow with sufficient precision up to $p_T=3-4$ GeV/c range.

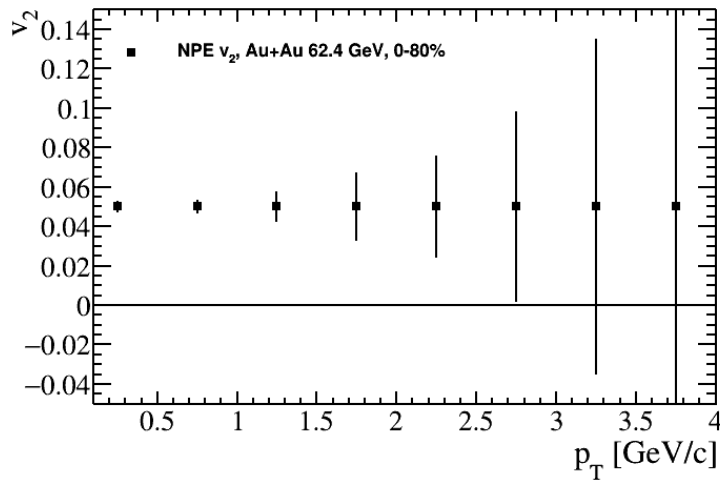


Figure 4–19: Statistical projection on NPE $v_2(0-80\%)$ measurements in $|\eta|<1$ with 1B minimum bias.

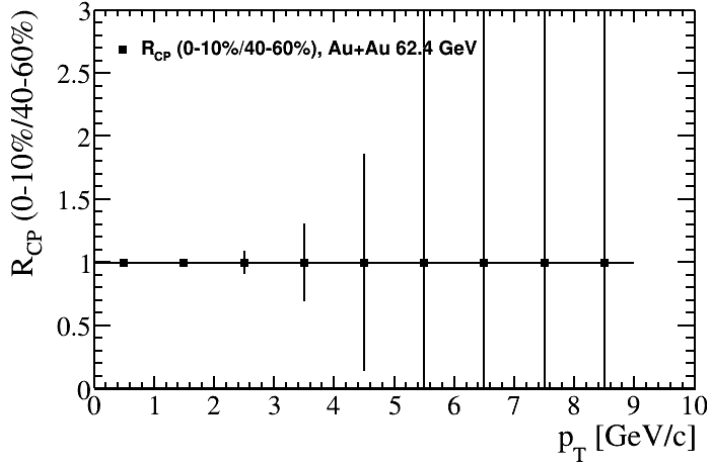


Figure 4–20: Statistical projection on NPE R_{CP} (0-10%/40-60%) measurements in $|\eta|<1$ with 1B minimum bias Au+Au 62.4 GeV.

While the precise measurement of the NPE R_{AA} at 62.4 GeV is hindered by the lack of a high quality p+p baseline, a R_{CP} measurement can be made utilizing the peripheral data as shown in Figure 4–20. The figure shows projections for NPE R_{CP} (0-10%/40-60%) for 1B MB events based on pQCD predictions for NPE production at $\sqrt{s_{NN}} = 62.4$ GeV and assuming binary scaling [76].

4.9.2 Jet Energy Loss Measurements

STAR’s development of a mixed event subtraction technique allows us to precisely subtract the combinatorial jet contribution from the measured recoil jets down to low p_T . Recoil jets, which have been widely used in jet quenching studies, are jets reconstructed on the opposite hemisphere in azimuth relative to the trigger jet/hadron. Without this mixed-event subtraction the underlying background, due to particles arising from soft (low Q^2 processes), in heavy-ion collisions overwhelms the signal jets. At lower collision energies this background is especially dominant due to the steepness of the jet spectrum. Our hadron triggered recoil jet analysis has the added advantages of no selection bias on the recoil jet’s fragmentation pattern, the ability to extend to large jet radii (currently up to $R=0.5$), all over a broad kinematic coverage including low transverse momenta.

A preliminary high p_T (6-20 GeV/c) hadron-triggered recoil jet analysis has been performed on the Run 10 Au+Au data at $\sqrt{s_{NN}} = 62.4$ GeV utilizing the anti- k_T jet finding algorithm for charged jets with $R=0.3$. Figure 4–21 (left) shows the measured recoil jet spectrum corrected for the average background energy density ρ in mid-central (30%-50%) collisions (red points). The mixed event distribution is shown as the gray shaded area. A significant signal above the mixed event is seen for $p_T > 5$ GeV/c. A comparison of the background subtracted distribution to a smeared PYTHIA calculation (\sim p+p \otimes heavy-ion fluctuations) is shown on the right hand side of Figure 4–21. An average suppression of 0.24 is observed. On both plots an extrapolation to higher jet p_T

values is shown, using PYTHIA with an assumed suppression factor of 9 (left) and an exponential fit to data (right). The orange shaded areas show the expected statistical error bars for charged jets with 1B minimum bias events which can be collected by STAR in a 4 week data taking period. The kinematic reach in charged jet energy for this dataset is about 20 GeV. STAR's EMCAL can be utilized to provide the neutral energy information and work on incorporating this information is underway. Note also that this range corresponds to the jet spectrum without the unfolding corrections, which account for the smearing introduced from underlying fluctuations, applied. This analysis will enable the precise study of jet energy loss in a region of significant overlap with measurements at higher collision energies.

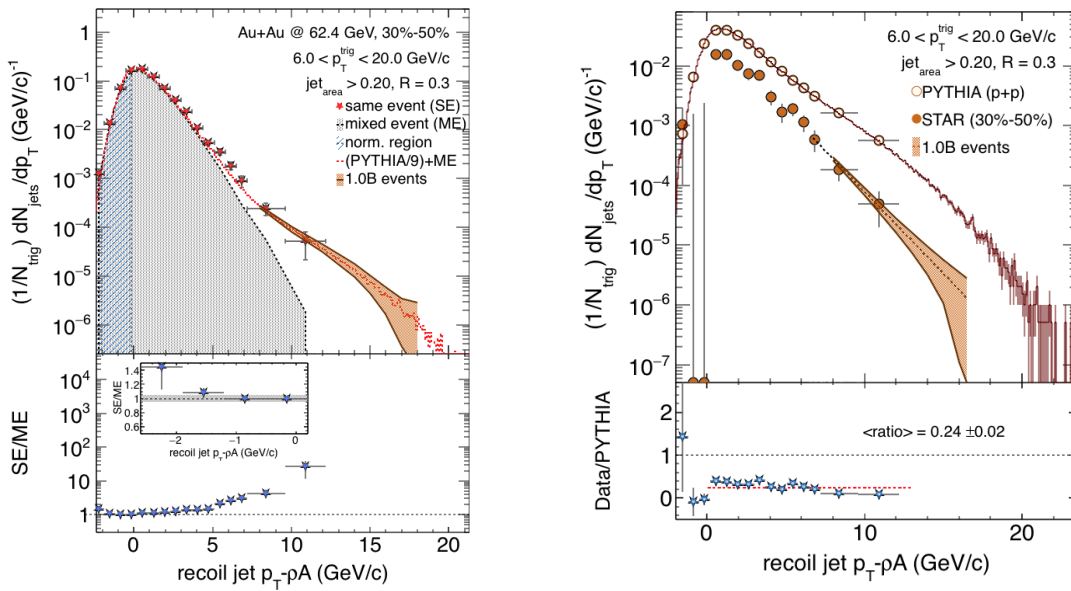


Figure 4–21:(left) Recoil jet spectrum for $R=0.3$ in mid-central (30%-50%) Au+Au collisions at $\sqrt{s_{NN}} = 62.4$ GeV corrected for the average background energy density ρ , with a charged hadron trigger with $p_T > 6$ GeV/c. The gray shaded area depicts the mixed-event distribution, which represents the combinatorial background (see text for details). (right) Background subtracted recoil jet spectrum. In both figures a comparison to PYTHIA calculations is shown and an extrapolation to higher jet p_T values with increased statistics. A suppression factor of 9 was assumed on the left plot for PYTHIA .

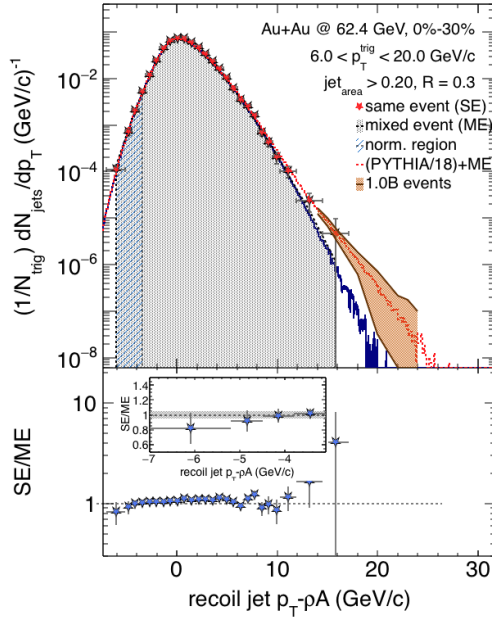


Figure 4–22: Recoil jet spectrum for $R=0.3$, in the 30% most central Au+Au collisions at $\sqrt{s_{NN}} = 62.4$ GeV. The gray shaded area and blue histogram depict the mixed event distribution. The red histogram shows a PYTHIA calculation with an assumed jet suppression of 18, which fits the data in the whole p_T range. The orange shaded area is showing the expected statistical error bars for 1B recorded MB events.

Figure 4–22 shows the preliminary recoil jet spectrum for 0-30% most central Au+Au collisions at $\sqrt{s_{NN}} = 62.4$ GeV. The statistics of the current dataset are too limited to extract a significant signal. Nevertheless, the central values of the data hint at a significantly larger suppression than at higher energies. With 1B MB events we can extend the p_T range for most central collisions to about 25 GeV/c in charged jet energy. The expected statistical errors for 1B events are shown as an orange shaded band using PYTHIA with a suppression of 18 to estimate the recoil jet spectrum at higher p_T . If the picture of very strong jet suppression persists, the requested dataset will make constrained measurements at the highest p_T , and provide significant upper limits at lower p_T .

4.9.3 Dilepton and Direct Virtual Photon Measurements

The removal of the HFT for the proposed dataset of Au+Au at 62.4 GeV allows us to project significant improvements in our di-electron measurements, which will have an important impact in the intermediate invariant mass range. Assuming STAR collects between 1-1.5B minimum-bias events, and applying the same conservative presumptions as before, we expect 400M or 600M events to be available for this measurement. As a result, the projected uncertainties, Figure 4–23 Left, on our measurements will reduce by a factor of 2.5 or 3.0, respectively. The improvements below di-electron masses of 2 GeV/c² allow for STAR’s measurements to reach statistical uncertainties that are comparable to the current systematic uncertainties.

Additionally, as is shown in Figure 4–23 Right, a 1.5B minimum-bias sample would enable a first measurement from STAR of direct (virtual) photons at this center-of-mass energy. This can be of particular interest in improving our understanding of thermal photon production vis-a-vis its elliptic flow for which at top RHIC energies of 200GeV several efforts exist to reconcile both into one consistent theoretical framework. Calculations [77] predict such effects to be stronger if the early QGP phase is closer to the critical temperature, e.g. initial conditions with lower center-of-mass energies. At low p_T , the projected systematic (boxes) and statistical (bars) uncertainties permit measurements of T_{slope} within ~ 40 MeV.

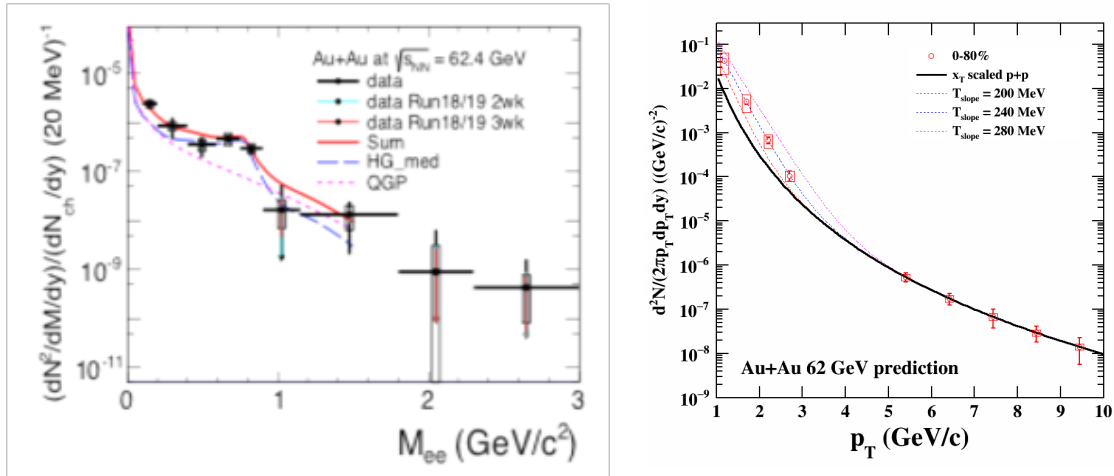


Figure 4–23: (left) STAR preliminary measurement of the acceptance-corrected di-electron invariant mass spectrum for $\sqrt{s_{NN}} = 62.4$ GeV. The hadron cocktail has been subtracted. The dashed and striped curves depict calculations that include a hadron gas (HG) and quark-gluon plasma (QGP) by Rapp et al. The magenta and red vertical bars indicate the improved statistical uncertainties in the case of a 1B or 1.5B scenarios, respectively. (right) The projected direct virtual photon measurements based on a 1.5B scenario. The black line corresponds to an x_T -scaled p+p measurement [77], while the colored striped lines show theory predictions for different T_{slope} values.

5 Run 18 Request

5.1 Isobar collisions (Zr+Zr, Ru+Ru) at 200GeV

STAR has been searching for evidence of chiral magnetic/vortical effects for more than a decade, and so far the experimental observables support the pictures of the chiral magnetic effect, the chiral magnetic wave and the chiral vortical effect. To draw a firm conclusion, an effective way is needed to disentangle the signal and the background contributions, the latter of which is intertwined with collective flow. Collisions of isobaric nuclei, i.e. $^{96}_{44}\text{Ru}+^{96}_{44}\text{Ru}$ and $^{96}_{40}\text{Zr}+^{96}_{40}\text{Zr}$, present a unique opportunity to vary the initial magnetic field by a significant amount while keeping everything else almost the same. With 1.2B events for each collision system at 200 GeV, we will be able to determine the CME signal with a significance better than 5σ , assuming that the background contribution is less than 80%. As a by-product, the flow measurements will ascertain the deformation information of the Zr and Ru nuclei, while such uncertainties will not pose a difficulty to the CME analysis for the centrality range of interest.

5.1.1 Initial Magnetic Field Dependence of Charge Separation

To disentangle the possible CME signal and the flow-related background, we can either vary the background with the signal fixed, or vary the signal with the background fixed. The former approach was carried out by utilizing the prolate shape of the uranium nuclei ($\beta_2 = 0.29$) [78]. In RHIC run 2012, we collected 0–1% most central events from U+U collisions at 197 GeV, where the charge-separation signal is dominated by the background since the CME should be greatly suppressed under the condition of the minimal magnetic field. One of the findings from that data set is that multiplicity production is far less dependent on the number of binary collisions than expected, so it is harder to isolate tip-tip collisions (small v_2) from body-body collisions (large v_2). This significantly reduces the lever-arm available to manipulate v_2 in order to disentangle v_2 backgrounds from the CME. STAR preliminary results [34] in Figure 2–21 show a charge-separation signal highly consistent with zero, while v_2 ($\approx 2.5\%$) is still sizable. This is consistent with the picture of the CME for very central collisions, and demonstrates the smallness of the flow-related background in those events. However, for more peripheral collisions where the CME signal is more prominent, a model-dependent extrapolation has to be employed to estimate the background contributions. So far it remains elusive to effectively distinguish U+U and Au+Au collisions if they are mid-central/mid-peripheral events.

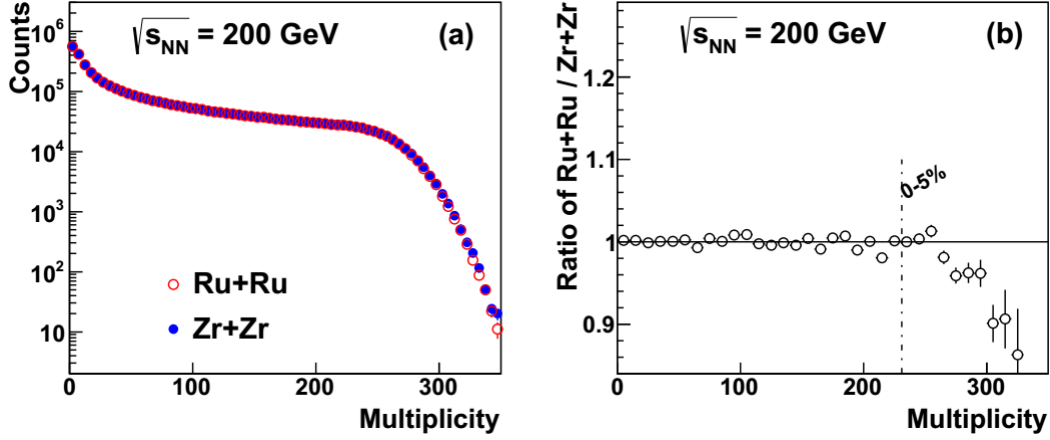


Figure 5-1: The Monte Carlo Glauber simulation of multiplicity for $^{96}_{44}\text{Ru}+^{96}_{44}\text{Ru}$ and $^{96}_{40}\text{Zr}+^{96}_{40}\text{Zr}$ at 200 GeV (a) and the ratio (b).

The latter approach (with the background fixed) can be realized, especially for mid-central/mid-peripheral events, with collisions of isobaric nuclei, such as $^{96}_{44}\text{Ru}$ and $^{96}_{40}\text{Zr}$ [78]. Ru+Ru and Zr+Zr collisions at the same beam energy are almost identical in terms of particle production, which is illustrated with the Monte Carlo Glauber [79] simulation in **Error! Reference source not found.** The ratio of the multiplicity distributions from the two collision systems is consistent with unity almost everywhere, except in 0 – 5% most central collisions, where the slightly larger radius of Ru ($R_0 = 5.085$ fm) plays a role against the smaller radius of Zr ($R_0 = 5.02$ fm). For the CME analysis, we will focus on the centrality range of 20–60%, so that the background contribution due to the multiplicity is negligible. The nucleus deformity, β_2 , does not noticeably influence the multiplicity distribution.

There are two sources of our knowledge on β_2 of Ru and Zr: e-A scattering experiments [80] and comprehensive model deductions [81]. According to the first source, Ru is more deformed ($\beta_2^{\text{Ru}} = 0.158$) than Zr ($\beta_2^{\text{Zr}} = 0.08$), while the second source tells the opposite: $\beta_2^{\text{Ru}} = 0.053$ and $\beta_2^{\text{Zr}} = 0.217$. This systematic uncertainty has different impacts on the signal (via the initial magnetic field) and the background (via the initial eccentricity), to be discussed later.

The difference in the initial electric charge between Ru+Ru and Zr+Zr collisions provides a handle on the magnetic field, which is mostly produced by the spectator protons. **Error! Reference source not found.** presents the theoretical calculations of the initial magnetic field component that is relevant to the γ correlator, $(eB/m_\pi)^2 \cos[2(\Psi_B - \Psi_{\text{RP}})]$, for the two colliding systems at 200 GeV [82]. For the same centrality bin, Ru+Ru collisions produce a significantly stronger magnetic field than Zr+Zr. Some theoretical uncertainties come from the modeling of the nuclei, e.g., how to model the electric charge distribution of the proton: treating the proton as a point charge or as a uniformly charged ball or something else. But for the event averaged calculation, this type of uncertainty is small. Another uncertainty involves the Lienerd-Wichert potential used in this calculation, which contains no quantum corrections. At RHIC energies, including the QED correction makes little difference. The theoretical uncertainties are

greatly suppressed when we take the ratio between the two systems. The panel (b) of **Error! Reference source not found.** shows that the ratio of Ru+Ru over Zr+Zr is approaching 1.18 for peripheral events, and reduces to 1.14 for central events. The deformity of the nuclei does not affect $\langle B_y \rangle$, but $\langle B^2 \rangle$ is influenced by the position fluctuation of nucleons and thus by β_2 . The calculations with the two cases of Glauber inputs are shown with solid and dashed lines, and they are more different in more peripheral collisions.

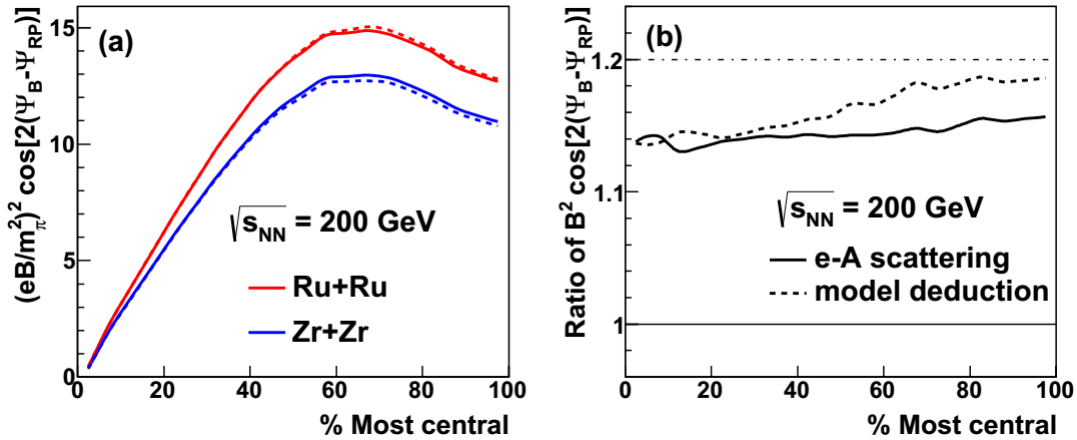


Figure 5-2: Theoretical calculations of the initial magnetic field for $^{96}_{44}\text{Ru}+^{96}_{44}\text{Ru}$ and $^{96}_{40}\text{Zr}+^{96}_{40}\text{Zr}$ at 200 GeV (a) and the ratio (b) vs centrality [82]. The solid lines represent calculations with Glauber parameters obtained from e-A scattering experiments, and the dashed lines from comprehensive model deductions.

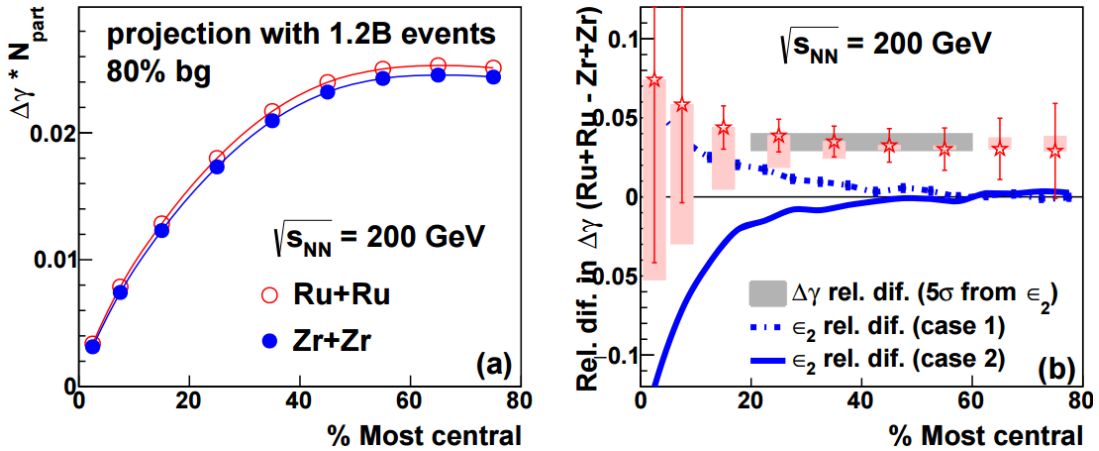


Figure 5-3: Projections of $\gamma * N_{\text{part}}$ for $^{96}_{44}\text{Ru}+^{96}_{44}\text{Ru}$ and $^{96}_{40}\text{Zr}+^{96}_{40}\text{Zr}$ at 200 GeV (a) and the relative difference (b) vs centrality, assuming the background level to be four-fifths. The central values are based on the Glauber parameters obtained from e-A scattering experiments (case 1), and the shaded systematic uncertainty box on each point in panel (b) reflects the Glauber parameters from comprehensive model deductions (case 2). The difference in the initial eccentricity from the Monte Carlo Glauber simulation is also shown in the panel (b).

If our observed charge separation really contains the CME contribution, $(\Delta\gamma \times N_{\text{part}})$ should be a function of $(eB/m_\pi^2)^2 \cos[2(\Psi_B - \Psi_{\text{RP}})]$. Based on the STAR measurements for Au+Au collisions at 200 GeV, we have the projections of $(\Delta\gamma \times N_{\text{part}})$ for 1.2 billion Ru+Ru and Zr+Zr collisions at 200 GeV as functions of centrality in Figure 5–3 (a), assuming that the background contributes two thirds of the observed signal. Since previous STAR results have revealed the charge separation in both Au+Au and Cu+Cu at both 200 GeV and 62.4 GeV, and ^{96}Ru (^{96}Zr) bridges ^{197}Au and ^{63}Cu , there should be no worry about the isobaric nuclei being too small to create the pertinent physics. The error bars in Figure 5–3 (a) reflect the statistics of 1.2×10^9 minimum bias events. The systematic uncertainties in the projections are largely canceled out with the relative difference in γ between Ru+Ru and Zr+Zr, shown in Figure 5–3 (b). When we combine the events of 20–60% collisions, the difference is 5σ above the relative difference in eccentricity for both cases of Glauber inputs, which are obtained from e-A scattering experiments (case 1) and comprehensive model deductions (case 2). On the other hand, if our charge-separation observable solely is driven by collective flow, the relative difference in γ should closely follow the relative v_2 (or eccentricity) difference, depicted by the blue curves in the panel (b). The relative difference in the initial eccentricity comes from the Monte Carlo Glauber simulation, and it is highly consistent with 0 for peripheral events, and goes above/below 0 in central collisions owing to the deformation of the Ru/Zr nucleus. For the centrality range of interest, 20–60%, the v_2 difference should be very close to zero, so that the related backgrounds stay almost the same for Ru+Ru and Zr+Zr. Therefore, the isobaric collisions provide a unique test to pin down the underlying physics mechanism for the observed charge separation. As a by-product, v_2 measurements in central collisions will discern which information source is more reliable regarding the deformity of the Zr and Ru nuclei.

The determination of the background level in the γ correlator can be effectively turned into the estimate of the value of κ as introduced in Eq.(1). The upper limit of κ is ~ 2 according to theoretical calculations [32] and the AMPT model calculations. For data analyses, in the " κ " unit, we can define a $\kappa^{\text{CME killer}} = \Delta\gamma/(v_2\Delta\delta)$, which is the κ value needed to kill all the CME signal. For Au+Au collisions with center-of-mass energy equal to or larger than 19.6 GeV, $\kappa^{\text{CME killer}}$ turns out to be always larger than 3 for the centrality range of 30-80%. That means the background level is lower than two thirds for those collisions. For 20-30% Au+Au collisions, $\kappa^{\text{CME killer}}$ decreases to 2.5, which provides an upper limit of four fifths (80%) for the background contribution. This is of course a very crude estimate, because we miss the details of the projection of the signal and the background separately from Au+Au to the isobaric collisions, and the realistic κ value may stay well below 2, e.g. between 1.3 and 1.4 as mentioned in Sec 2.3.1. All these can be further clarified when the isobaric collisions come into being.

When a different background level is assumed, the magnitude and significance of the projected difference in γ between Ru+Ru and Zr+Zr change accordingly, as shown in Figure 5–4. The future measurements of the isobaric collision data will determine whether there is a finite CME signal observed in the γ correlator, and if the answer is “yes”, will ascertain the background contribution, when compared with this figure.

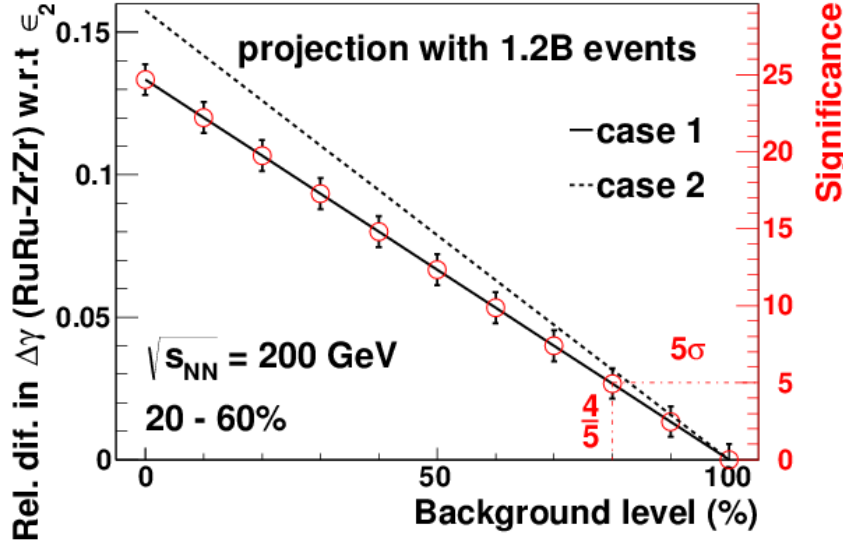


Figure 5-4: Magnitude (left axis) and significance (right axis) of the relative difference in the projected $\gamma \times N_{\text{part}}$ between ${}^{96}_{44}\text{Ru}+{}^{96}_{44}\text{Ru}$ and ${}^{96}_{40}\text{Zr}+{}^{96}_{40}\text{Zr}$ at 200 GeV. We use the relative difference in eccentricity as the baseline.

Table 5.1 lists the expected relationship between Ru+Ru and Zr+Zr in terms of experimental observables for elliptic flow, CME, CMW and CVE, assuming that the chiral effects are major physics mechanisms for the corresponding observables. With this assumption for the CMW observable, we have carried out a 700M-event projection for the slope parameter r , and found the r ratio of Ru+Ru over Zr+Zr to be 1.08 ± 0.08 for 20–60% collisions, which is only a 1σ effect. The CVE does not explicitly depend on the magnetic field, so to the 1st-order we expect the same amount of baryon-number separation for Ru+Ru and Zr+Zr.

Observable	${}^{96}_{44}\text{Ru}+{}^{96}_{44}\text{Ru}$ vs ${}^{96}_{40}\text{Zr}+{}^{96}_{40}\text{Zr}$
flow	\approx
CME	$>$
CMW	$>$
CVE	$=$

Table 5.1: The expected relationship between Ru+Ru and Zr+Zr in terms of experimental observables for elliptic flow, CME, CMW and CVE.

Assuming 80% data collection efficiency we estimate needing 3.5 weeks of RHIC operation per collision system to collect 1.2B events. An extra collision energy point will help understand the beam-energy dependence of the true CME signal. It is feasible to also have the isobaric collisions at 27 GeV. The observed charge separation at 27 GeV is very similar to, if not bigger than, that at 200 GeV. However for the same centrality bin, the multiplicity at 27 GeV is lower than that at 200 GeV by a factor of 1.6. Therefore, to reach the same significance level as 200 GeV, we need to increase the number of events by a factor of 4 (1.6^3 due to the two particles and the resolution of the event plane involved in the γ correlator).

We have also examined whether there are other isobar pairs better suited to the purpose of these studies than Ruthenium and Zirconium. There are three other stable sets of nuclear isobars with charge differences of 4. These include $^{124}\text{Sn}/^{124}\text{Xe}$, $^{130}\text{Te}/^{130}\text{Ba}$ and $^{136}\text{Xe}/^{136}\text{Ce}$. For the larger isobars, ratios of Z decrease from 44/40 for Ru/Zr to 58/54 for Ce/Xe. We find however that the improvement expected in the event plane resolution from the larger multiplicities in the larger nuclei compensates for the reduced ratio of charges, so that we expect very similar statistical significance on the measurement of the magnetic field dependent portion of the measured charge separation. For this reason, any of the four isobar pairs is similarly suited for the study and the deciding factor should be the practicality of using them in RHIC.

5.1.2 Dilepton Production in Isobaric Collisions

In peripheral 60-80% U+U collisions, we observe a significant enhancement in di-electron mass spectrum at $p_T < 0.15$ GeV/c compared to known hadronic contributions (cocktail simulations), as shown in Figure 5-5 [83]. In the low mass region 0.4-0.76 GeV/c², the ratio of data over cocktail is 16.4 ± 1.1 (stat.) ± 2.6 (syst.). In the J/ψ mass region 2.8-3.2 GeV/c², the ratio of data over cocktail is 20.4 ± 4.2 (stat.) ± 3.0 (syst.). Figure 5-6 shows the excess (data - cocktail) di-electron mass spectrum in the low-mass region compared to a broadened- ρ model calculation for $p_T < 0.15$ GeV/c in peripheral 60-80% U+U collisions [83]. The observed excess is a factor of ten larger than the thermal contribution from hot, dense medium, as indicated by the broadened- ρ model calculation.

There could be two sources contributing to the low- p_T di-electron enhancement in peripheral collisions: photonuclear [84] and two-photon processes [85]. In coherent vector meson photoproduction, a photon from the field of one nucleus fluctuates into a virtual quark-anti-quark pair which scatters elastically from the other nucleus, emerging as a real vector meson, which then decays into a di-electron pair. In a two-photon process, a photon from the field of one nucleus interacts from the other photon from the other nucleus, emerging as a di-electron pair. These two processes have a different dependence on the atomic number (Z) of the nucleus, with photonuclear cross section proportional to Z^2 and two-photon cross section proportional to Z^4 .

We also find that this large enhancement decreases with increasing p_T and/or in more central collisions. We note that a strong J/ψ excess for low p_T and peripheral heavy-ion collisions is also observed at ALICE [86]. The centrality and p_T dependences reported by ALICE are similar to what we observed at STAR [83].

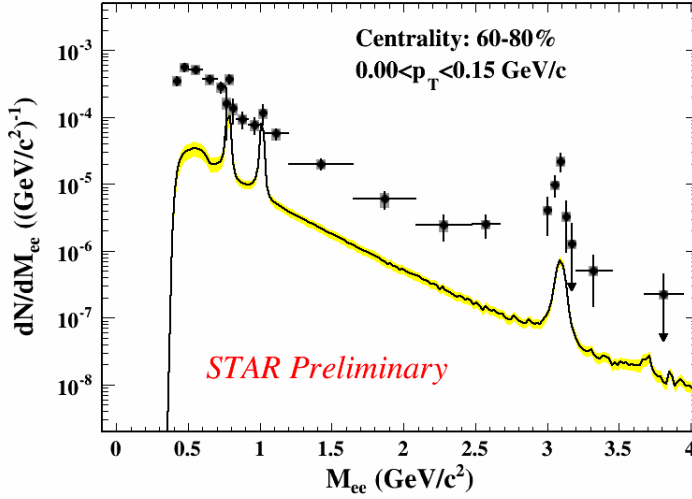


Figure 5–5: Di-electron invariant mass spectrum within STAR acceptance [$p_T(e) > 0.2$ GeV/c, $|\eta(e)| < 1$, and $|y_{ee}| < 1$] at very low p_T ($p_T < 0.15$ GeV/c) in U + U peripheral collisions (60–80%) at 193 GeV, compared with hadronic cocktail simulation (black solid line). Gray boxes depict the systematic uncertainties of the data. Yellow bands depict systematic uncertainties of the cocktail simulations.

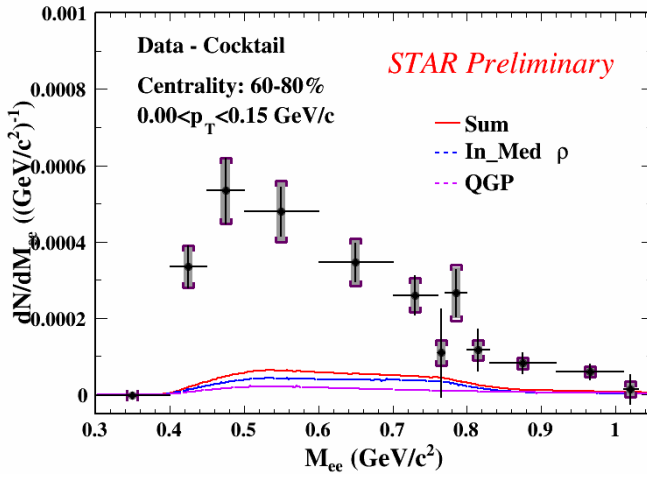


Figure 5–6: Mass spectra of the excess (data - cocktail) within STAR acceptance in LMR at very low p_T ($p_T < 0.15$ GeV/c) in U + U peripheral collisions (60–80%). Also shown is a broadened- ρ model calculation (red solid line). Gray boxes represent the systematic uncertainties of the data. Dark violet brackets represent the total systematic uncertainties including those from cocktail simulation.

5.1.3 Di-electron Measurements in Ru+Ru and Zr+Zr Collisions

The atomic number (Z) and atomic mass number of a Ru nucleus are 44 and 96, respectively. A Zr nucleus has the same atomic mass number as a Ru nucleus but has a different Z value, which is 40. The Zr+Zr and Ru+Ru collisions can therefore potentially distinguish the two processes mentioned above, namely, a Z^2 dependence for the photonuclear process and Z^4 dependence for the two-photon process. In a given heavy ion collision event the cross section of these processes actually depend on the magnitude of the magnetic field produced by the protons in the colliding nuclei. It must be noted that in addition to Z the produced magnetic field also depends on the distribution of the protons inside the colliding nuclei and the impact parameter of the collisions. For realistic estimations of the magnetic field one must take into account the event-by-event variation

of the impact parameter and the fluctuations of the position of the colliding proton inside the colliding nuclei. We therefore perform Glauber model simulation to do such estimations in different systems.

From the Glauber model calculations, we find that 60-80% U+U collisions will produce the same number of tracks as 47-75% Zr+Zr and Ru+Ru collisions [87]. Therefore, we expect the same cocktail contribution and hot, dense medium contribution to the di-electron production in 60-80% U+U collisions, 47-75% Zr+Zr and Ru+Ru collisions. We also find that the $\langle B^2 \rangle$ and $\langle B^4 \rangle$ value for these three collision cases are different. The ratios of $\langle B^2 \rangle$ in 47-75% Zr+Zr and Ru+Ru over that in 60-80% U+U are 0.85 and 0.98, respectively. The ratios of $\langle B^4 \rangle$ in 47-75% Zr+Zr and Ru+Ru over that in 60-80% U+U are 0.84 and 1.07, respectively [87]. The results obtained from the Glauber model calculations are summarized in Table 1.1.

Quantities	Systems		
	U+U	Ru+Ru	Zr+Zr
Centrality	60-80	47-75	47-75
Multiplicity ($ \eta < 0.5$)	12-52	12-52	12-52
N_{part}	21 ± 1	21 ± 1	21 ± 1
B^2 (fm^{-4})	30.8 ± 0.1	30.1 ± 0.1	26.2 ± 0.1
B^4 (fm^{-8})	1984 ± 4	2121 ± 4	1672 ± 4

Table 5.2: Results obtained from the Glauber model calculations [87] for different colliding systems. The estimations of the magnetic fields are done at the time of the collisions ($t=0$) and at the center of the participant zone. The multiplicity is obtained using two-component model that is tuned to fit Au+Au data.

With all the above information, we estimate with 1.2 billion good events for data analysis, the expected di-electron data over cocktail ratios in the isobar collisions and the projected differences for the two physics scenarios in Zr+Zr and Ru+Ru collisions. The results are shown in Table 5.3 and Table 5.4 for two different mass regions.

Physics process	47-75% Zr+Zr (data/cocktail)	47-75% Ru+Ru (data/cocktail)	Difference between Zr+Zr and Ru+Ru
Photonuclear	14.3 ± 0.4	16.1 ± 0.4	1.8 ± 0.6 (3.0σ)
Two-photon	14.2 ± 0.4	17.4 ± 0.4	3.2 ± 0.6 (5.3σ)

Table 5.3: The expected di-electron data over cocktail ratios in the mass region $0.4-0.76 \text{ GeV}/c^2$ for $p_T < 0.15 \text{ GeV}/c$ with 1.2 billion minimum-bias isobar collisions and the projected differences for the two physics scenarios in Zr+Zr and Ru+Ru collisions.

Physics process	47-75% Zr+Zr (data/cocktail)	47-75% Ru+Ru (data/cocktail)	Differences between Zr+Zr and Ru+Ru
Photonuclear	17.5 ± 1.7	20.0 ± 1.7	2.5 ± 2.4 (1.0σ)
Two-photon	17.3 ± 1.7	21.8 ± 1.7	4.5 ± 2.4 (1.9σ)

Table 5.4: The expected di-electron data over cocktail ratios in the mass region $3.0-3.2 \text{ GeV}/c^2$ for $p_T < 0.15 \text{ GeV}/c$ with 1.2 billion minimum-bias isobar collisions and the projected differences for the two physics scenarios in Zr+Zr and Ru+Ru collisions.

5.2 Au+Au Collisions at 27GeV

5.2.1 Global Polarization Measurements at 27GeV

To test the hypothesis of a magnetically-induced splitting between the Lambda and Anti-Lambda polarization, it is sufficient and it makes sense to focus on a single energy and obtain high statistics there. The primary theoretical uncertainty in our understanding of B-field effects [88] concerns its time evolution, which depends strongly on the electric conductivity of the plasma. Calculations with different conductivities differ by a few orders of magnitude [89]; the calculations with conductivity determined in the lattice QCD, yields fields (at the time of a few fm/c) eB or (a few) $\times 10^{-2} m_{\pi}^2$, similar to our equilibrium-based estimate using measured PM. In addition to being of fundamental interest on its own merits, the vorticity and magnetic field present during the evolution of a heavy ion collision are crucial inputs to the Chiral Vortical Effect (CVE) and Chiral Magnetic Effect (CME), respectively. These two effects are among the RHIC program's most exciting and visible topics today.

The discovery of chiral effects in these collisions deserves great attention and press if put on firm ground. Global hyperon polarization has nothing "chiral" about it. In a theoretically well-grounded way, it measures the average vorticity (ω) and field (B). A definitive statement about the B-field from GHP, however, requires reduced uncertainties preferably with statistics increase by at least an order of magnitude. Especially given the fact that BES-II will cover the lower energies, the numbers suggest running 27 GeV. The Event-Plane Detector (EPD) as discussed in section 7.2.2 would significantly improve the reaction plane resolution and greatly improve the signal strength. While similar high-statistics measurements of GHP will eventually be performed at lower energies in BES-II, the scientific impact of getting firm measures of vorticity and B much sooner is high, given the current intensity of research and attention on CME and CVE.

5.2.2 Dilepton Measurements at 27 GeV

In Figure 5–7, the preliminary acceptance-corrected excess spectrum for $\sqrt{s_{NN}} = 27$ GeV is shown. Super-imposed on the data points are projections of the improved uncertainties of our measurements for two scenarios. The uncertainties for each scenario are based on the measured preliminary uncertainties from the Run 11 run at 27 GeV. Furthermore, it includes the projected improvement of ~ 1.9 for the Au-beam luminosity in the Run 18 at 27 GeV, as well as an estimate of the performance envelope of the STAR DAQ rates based on Run 15's performance (saturate at 1.7~kHz). The scenarios involve two extreme cases: (i) running for 2 RHIC weeks at a data-taking efficiency comparable to what was previously achieved for the same energy during Run 11 and (ii) running for 3 full weeks. These scenarios yield approximately 400M and 700M events that pass the analyses criteria for both scenarios, respectively.

As a result, we expect the average uncertainties to reduce by a factor of 2.4 (2-week scenario) up to 3.2 (3-week scenario). Model calculations [4] show that for di-

electron masses above that of the ϕ meson the main contribution to the di-electron spectra arrives from the QGP component. The projected improvements in either scenario allow for a first measurement in this intermediate mass range, thus allowing a first potential measurement of the temperature of the hot medium at this energy.

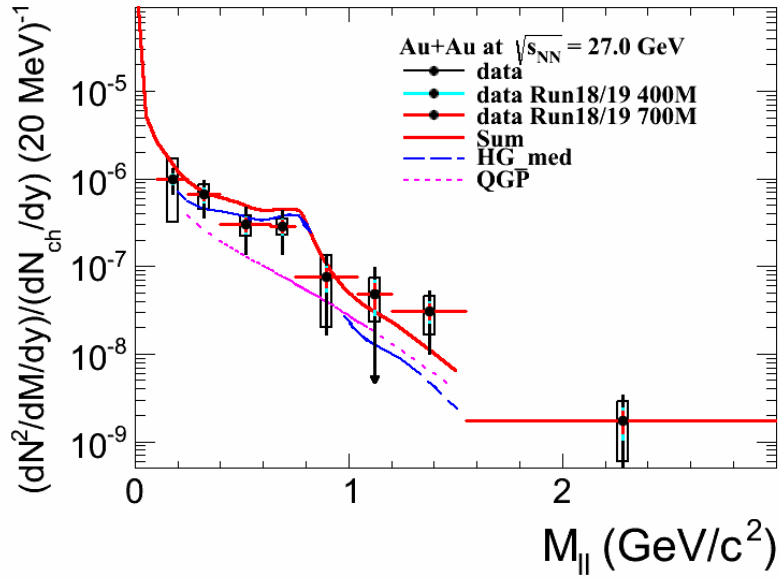


Figure 5–7: STAR preliminary measurement of the acceptance-corrected di-electron invariant mass spectrum for $\sqrt{s_{NN}} = 27$ GeV. The hadron cocktail has been subtracted. The dotted and striped curves depict calculations by Rapp et al. that include a hadron gas (HG) and quark-gluon plasma (QGP).

6 Calibration and Production Projections for run 17 and 18 requests

Producing the requested data for physics will involve significant use of data stores, considerable processing time, and time spent understanding and completing calibrations. When a dataset is a continuation of a collision species and energy from a previous year (with STAR's detector similarly set up), first-physics calibrations for the highest priority dataset typically require on the order of two months after the conclusion of data-taking for that year. Subsequent dataset calibrations for a given year need another month each. The proposed 500 GeV p+p and 27 GeV (and potentially 62 GeV) Au+Au datasets will be such continuations, adding to what were acquired in 2013 and 2011 (2010) respectively (repeating the environment of no HFT and no iTPC). Understanding features of new running conditions could extend calibrations of the isotope datasets to take a few months more, and it is important to keep in mind that unforeseen peculiarities of any given data set can further delay delivery.

Table 6.1 presents estimates of the DAQ and data summary ("MuDst") dataset sizes of expected totals of events to process for the proposed colliding species, along with projected single-pass production times on 100% of STAR's 2016 allocation of the RACF computing farm. These event totals may include impurity in the trigger (common at low collision energies), or other useful triggers we can fit without detriment into our bandwidth. It is critical to emphasize that these numbers are tied to the proposed event goals, and would scale with the actual events acquired. These productions will need to balance computing resource usage with prior-year datasets as well as ongoing calibrations and run support. STAR may choose, as an imaginable example, to produce Run 16 200 GeV Au+Au concurrently with the Run 17 500 GeV p+p in a 50%-50% apportionment, which would elongate the latter production to more than a year.

Storage space usage for physics analyses is an active and dynamic topic with the STAR Collaboration. Multi-year efforts overlap with delivering prompt results from recent data, such that data summaries have fully saturated existing storage resources immediately accessible to nodes on the RACF computing farm. Ongoing productions, as well as those listed in Table 6.1, will further stretch our needs. Relaxation of this resource constraint would likely benefit the efficiency of completing analyses.

Table 6.1 Computing resource estimates for production of the proposed Runs 17 and 18 datasets (see text for details)

Dataset	Expected events	DAQ size [PB]	MuDst size [PB]	Production time [months]
500 GeV p+p	5.0B	4.85	2.65	7.5
62 GeV Au+Au	2.7B	1.46	0.97	1.5
27 GeV Au+Au	2.5B	1.20	0.60	1.0
200 GeV Ru+Ru	1.4B	1.02	0.76	1.5
200 GeV Zr+Zr	1.4B	1.02	0.76	1.5
<i>totals</i>		<i>9.65</i>	<i>5.74</i>	<i>13.0</i>

7 Detector Upgrades for Run-17

7.1 Upgrades Critical to Measure Drell-Yan A_N

7.1.1 PreShower (FPS) Performance in Run-15

A preshower detector to distinguish photons, electrons/positrons and charged hadrons, was installed in front of the FMS at the beginning of the RHIC run 15. This detector is comprised of two layers of perpendicularly arranged scintillator slats (PS1 and PS2), followed by a lead converter and a subsequent third layer of scintillator slats (PS3). PS1 and PS2 are used to identify neutral particles (photons) from charged particles (hadrons and electrons), while PS3 after the converter is separating electromagnetic showers (photons and electrons) from charged hadrons. The preshower detector is located in front of the FMS at a little less than 7 m downstream of the nominal interaction point in STAR and covers a transverse area of about $2 \times 2 \text{ m}^2$ with a $40 \times 40 \text{ cm}^2$ cutout in the center for the beam pipe. The preshower layers are divided into quadrants. The detector is segmented to ~ 80 scintillator slats per layer, and the granularity of the array is matching that of the FMS. Due to up to 400 gauss of magnetic field from the STAR solenoid magnet, SiPMs (MPPC) were chosen for the readout instead of conventional PMT. The scintillation light from a scintillator slat was read out by two $3 \times 3 \text{ mm}$ Hamamatsu S12572-050P (PS1 & PS2) and S12572-025P (PS3) MPPC (SiPM), which are mounted on a FEE board and attached to light guides at the end of the scintillator slat.

Commissioning was finished before the start of proton-proton collisions with transverse polarization in late February. The detector was operated successfully through the remainder of the run until early July. Before data taking, we performed a gain matching for the channels in each layer (layers 1 and 2 are essentially the same, layer 3 used SiPMs with a different dynamic range). The performance of the detector was monitored throughout the operation in addition to daily scans of the dark current between RHIC fills. The dark current is a measure of the radiation damage to the SiPMs, mainly from secondary high energy neutrons in the surrounding material and the calorimeter. Figure 7–1 shows the increase of the dark current over time for one quadrants in layer 1 (similar for the other quadrants and layers). There is a clear correlation between beam operation and the deterioration of the dark current. The significant step between late April and early May is due to the commissioning of p+Au collisions in RHIC for the first time.

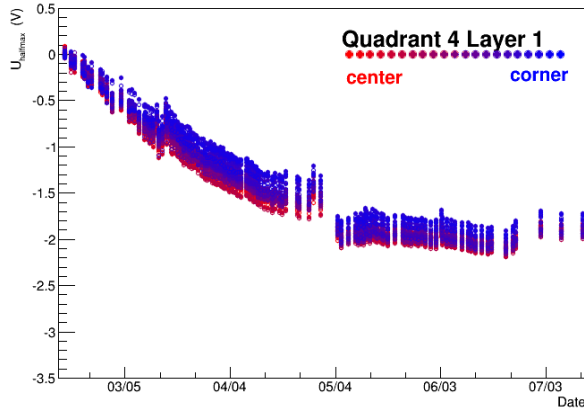


Figure 7-1: Example of dark currents from daily I-V-scans during run 15 operations. The deterioration is mainly from radiation damage of high energy neutrons on the SiPM. The central (red) channels show a slightly larger increase compared to the corner (blue) location. This is due to the relative distance from the beam pipe and the surrounding material (calorimeter).

Figure 7-2 shows the preshower response after calibration to minimum ionizing hits for each channel in the preshower (grouped by quadrant and layer; the white vertical lines are unused and not dead). There is a distinct peak for minimum ionizing particles with a tail towards multiple hits. This shows the capability of the preshower to differentiate between charged particles and photons, when combined with the cluster information from the FMS.

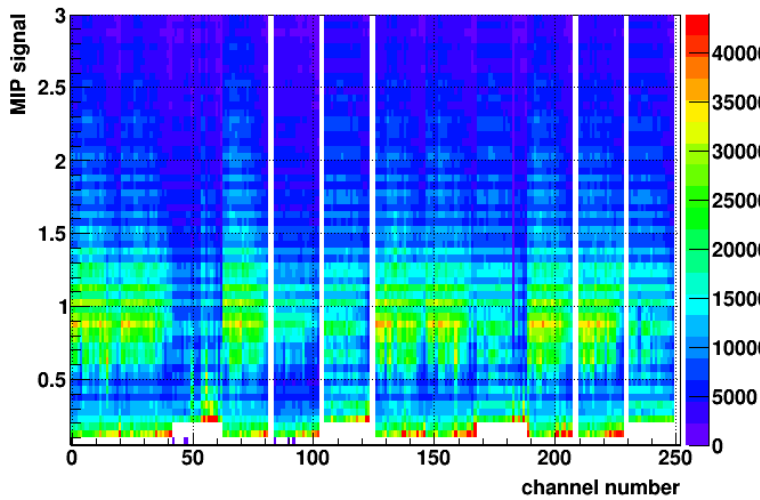


Figure 7-2: Response of the preshower detector per channel in groups of quadrants and layers (21 channels per quadrant in each layer). Layers 1 and 2 are very similar, layer 3 uses different SiPM with a slightly higher dynamic range for larger light yields.

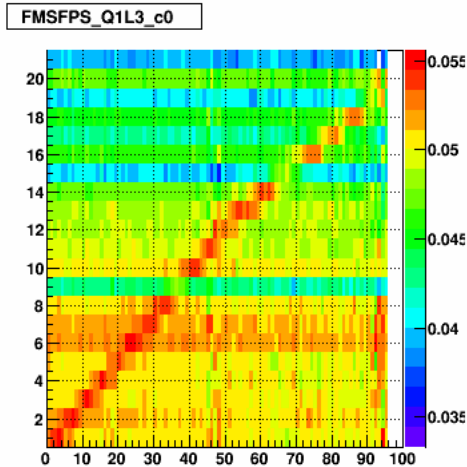


Figure 7–3: Correlation of a high tower in the FMS with individual scintillator strips in quadrant 1 of layer-3 in the preshower. A clear correlation is observed.

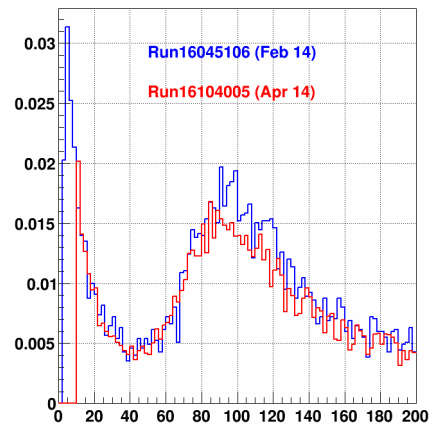


Figure 7–4: MIP peak in scintillator strip 4 in quadrant 1 layer-1 at the beginning of Run 15 (blue) and close to the end of the polarized p+p run (red). An excellent separation to the pedestal is seen.

Figure 7–3 shows first correlations of a high tower in the FMS with individual scintillator strips in quadrant 1 of layer-3 in the preshower. Figure 7–4 shows a MIP peak for one scintillator strip 4 in quadrant 1 layer-1 at the beginning of Run 15 (blue) and close to the end of the polarized p+p run (red). The separation between the pedestal and the MIP peak is excellent.

The main purpose of the preshower detector was the identification of direct photons in the FMS. While the analysis is still in its early steps, the performance of the preshower has been demonstrated in the reconstruction of photonic decays of light mesons, mainly pions. Figure 7–5 shows an example of the invariant mass distribution with typical pion selection cuts with and without the inclusion of information from the first two layers of the preshower. While the efficiency is dropping significantly for all masses, one can clearly see an improved signal over the background for neutral pions. This study is so far only based on simple cuts on the matching between each of the FMS clusters and the preshower layers in front. Next steps in the analysis will combine the available information into a multivariate analysis.

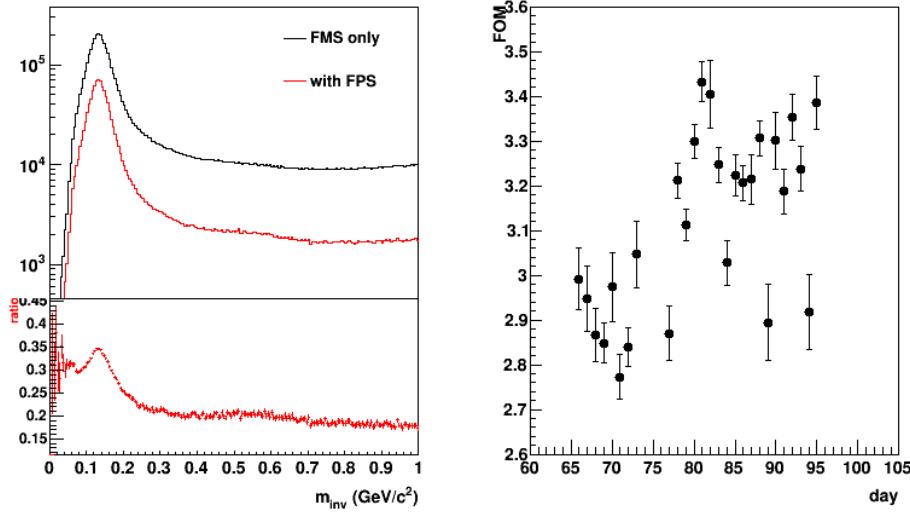


Figure 7-5: Invariant mass distributions of two clusters in the FMS with and without additional information from the preshower detector (left) and day-by-day improved figure of merit (right).

7.1.2 A PostShower (FPost) for the FMS in Run 17

The difficult task of DY measurements is the suppression of the overwhelming hadronic background which is on the order of $10^7 \sim 10^5$ larger than the total DY cross-section. The probability of mis-identifying a hadron track as e^+e^- has to be suppressed down to the order of 0.01% while maintaining reasonable electron detection efficiencies. Due to the rarity of Drell-Yan events, the simulation of the both the Drell Yan process and the large QCD background are crucial to understanding how well we can distinguish the signal from the background. We have studied the combined electron/hadron discriminating power of the proposed FMS postshower and current calorimeter systems. We found that by applying multivariate analysis techniques to the features of EM/hadronic shower we can achieve hadron rejection powers of 800 to 14,000 for hadrons of 15 GeV to 60 GeV with 90% electron detection efficiency. The hadron rejection power has been parameterized as a function of hadron energy and has been used in a fast simulation to estimate DY signal-to-background ratios.

The rapidity of interest is $2.5 < \eta < 4.0$. The current STAR detectors in this rapidity are the Forward Meson Spectrometer (FMS), a Pb-glass electromagnetic detector with photomultiplier tubes, and the preShower, three layers of scintillator with silicon photomultipliers. The FMS is primarily sensitive to electrons and photons while hadrons will leave as minimum ionizing particles. The preShower, which consists of three layers of scintillator, provides photon and charged particle separation. The first two layers provide x and y positioning. A lead converter precedes the third scintillator causing photons to shower in lead and deposit significant energy in the third scintillator. To suppress photons, the signal should have energy deposition in each layer of the preshower. The three detector (preShower, FMS and proposed postShower) setup provides photon/particle separation and electron/hadron discrimination.

We have simulated the response of the calorimeter to single electrons and π^- . To discriminate EM shower against hadronic shower we have used the total energy sums in layer 1, 2 and 3 of the preshower, total energy of the EMCAL (FMS) and total energy of the

postshower (see Figure 7–6). 5 million single particle events were run through the STAR geometry at intervals of 5 GeV ranging from 15 to 60 GeV. For lower energies, 100,000 provided efficient information to parameterize the rejection of the signal. For higher energies, from 45 to 60 GeV, 1 million events were necessary to parameterize. A parameterized rejection function was established at 90% electron efficiency.

These energy observables from the three detectors have been used as inputs to a Boosted Decision Trees (BDT) algorithm. The BDT contains 1000 binary decision trees each has a depth of 4 and corresponds to a particular partition of the 4-dimensional feature space into signal (electron) and background (hadron) regions. They are trained sequentially using half of the electron/ π^- samples generated. Mis-identified tracks from the previous decision trees were given a higher weight in training the subsequent trees. In the end each decision tree was given an index representing its performance during the training. In the validation stage the decision on each track identification was made based on the collective response of all of the decision trees, with each of their responses weighted by the performance index. The boosting algorithm takes advantage of using not only the discriminating power of each single observable but also the correlations among them.

To estimate the DY signal to background ratio the e/h discriminating power has been parameterized as a function of the track energy (see Figure 7–7). We have generated 600 million PYTHIA $p+p$ events at 500 GeV with $CKIN(3) = 3$ GeV and a forward filter requiring a total $p_T > 3$ GeV in any of the four jet-patch-like regions in $2.7 < \eta < 3.8$. All basic QCD $2 \rightarrow 2$ scatterings as well as heavy flavor channels were enabled. Events were smeared using the simulated detector resolutions of the Forward Meson Spectrometer.

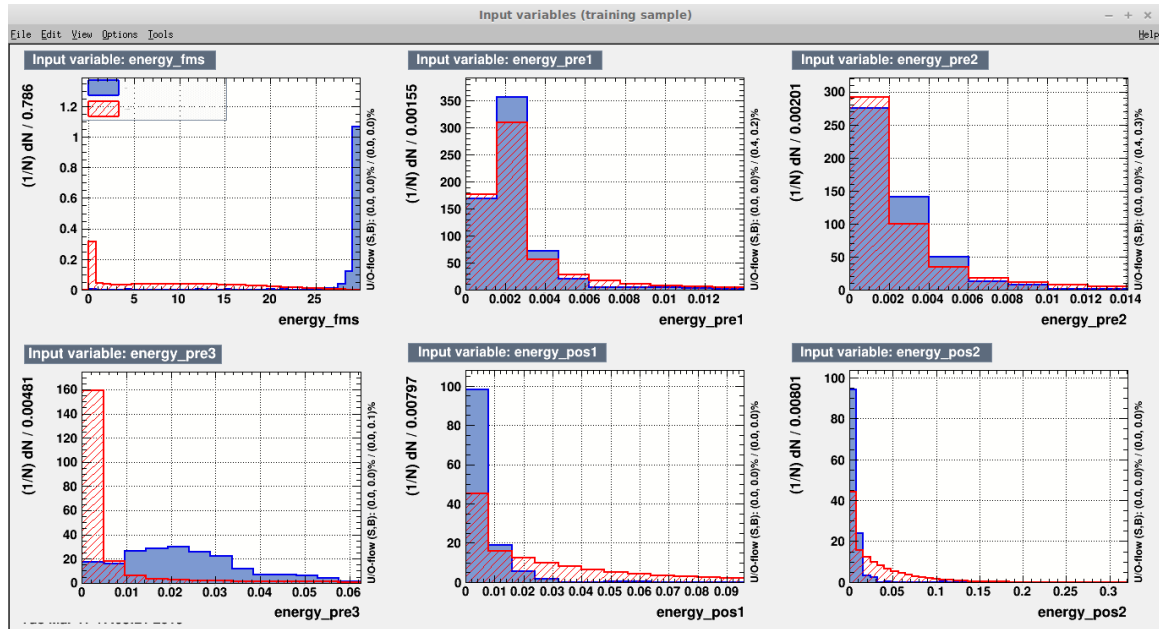


Figure 7–6: Energy from GEANT4 single particle simulations in the STAR geometry. The blue and red are signal and background, respectively, for the FMS, PreShower and PostShower from left to right and top to bottom.

The DY productions through $q\bar{q}$ annihilation and qg scattering processes were separately generated and scaled to the same luminosity. The final background yields as a

function of pair masses were then fit by an exponential function and rescaled to a total luminosity of 400 pb^{-1} , the results is shown in Figure 7–8.

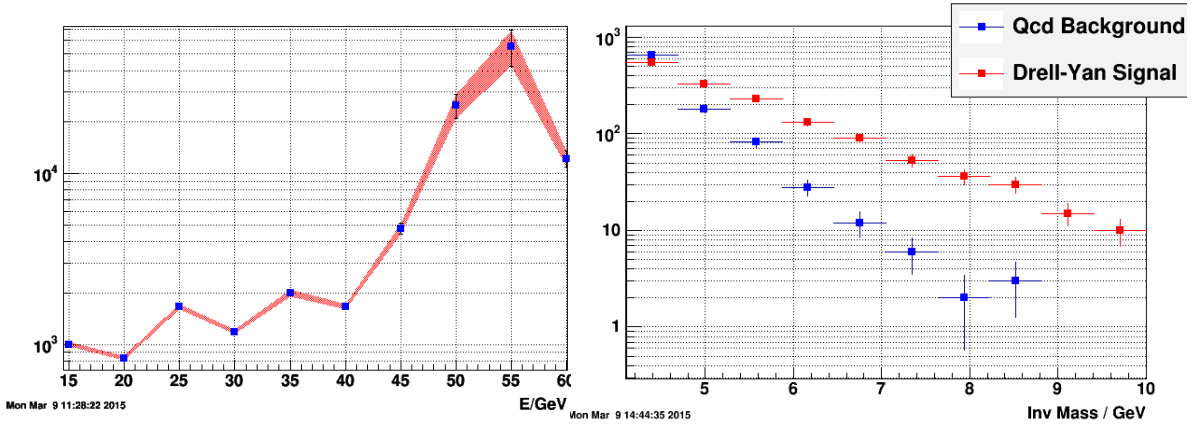


Figure 7–7: Rejection power as a function of energy with connected error bars. A smooth polynomial was fit to the rejection curve.

Figure 7–8: Plotting the background after BDT rejection (blue) along with a normalized Drell-Yan signal (red).

PostShower Design Details:

For the PostShower we propose to have 3 layers of scintillators, with the scintillator slats in PS1 oriented vertically, in PS2 horizontally and in PS3 under 45° degree. For PS1 and PS2 the inner 12 channels have a width of 4 cm, followed by 9 channels with a width of 5.8 cm. We are currently also looking in having all slats 4 cm wide. The length of the scintillators is 100 cm, or 80 cm where they touch the inner cutout region. For PS3 the slats have all a width of 4 cm., the main purpose of the third layer is to resolve ambiguities of hits in layer one and two and therefore allow for a better association with clusters in the FMS and hits in the three PreShower layers. All three layers will be divided in halves placed from left and right around the beam pipe behind the FMS. The readout will be identical to the one for the PreShower, based on the SiPMs from Hamamatsu, FEE boards by Gerard Visser and the STAR QT-boards, so no new development is needed.

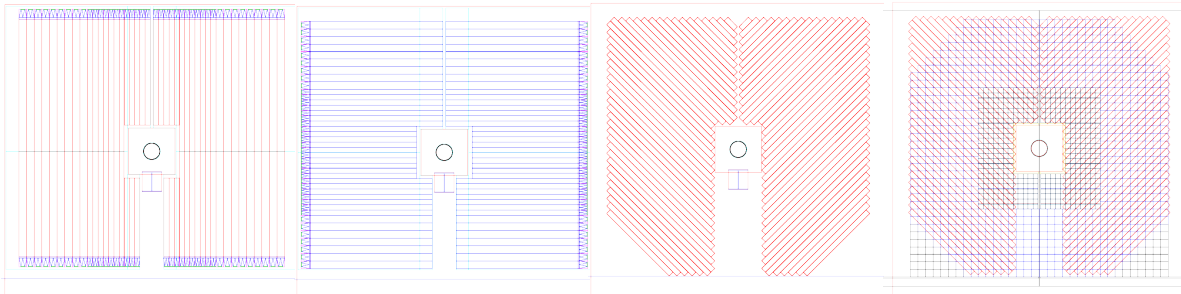


Figure 7–9: Geometry of the layers of a proposed PostShower detector behind the F1 electromagnetic calorimeter in STAR. **Left-to-Right:** The individual layers PS1, PS2 and PS3 and layered setup of scintillators with SiPM and FEE board (green).

7.1.3 FMS Performance in Run15 and Further Upgrades for Run17

Immediately after the run in 2013, the FMS lead glass was unstacked and the detector refurbished. Examination of the lead glass blocks revealed extensive damage by the beam, with a severe loss of light transmission in the glass. All lead glass cells were exposed to more than 40 hours of sunlight to “cure” the f-centers and bleach the glass to its original condition. Additionally, the phototube bases for 684 of the 788 large cells were experiencing gain jumps due to short circuits in a set of zener diodes in the last three stages of the amplification chain. Since these bases were integral with the PMTs themselves, this necessitated the removal of the original large cell PMTs, magnetic shields and mounting fixtures. These were replaced with new mounting fixtures and bases/PMTs (type EMI 9954) recovered from the decommissioned CDF barrel calorimeter at Fermilab. This work was completed in time for the polarized proton run in 2015.

Figure 7–10 shows the loss of gain in the FMS lead glass, as monitored by the LED system, as a function of pseudorapidity for three different integrated luminosity values. One can clearly see the effect of damage increasing for cells closer to the beamline. The expected damage due to all running in 2015 would correspond to approximately 200 pb^{-1} of delivered luminosity, which would give about 4 times the damage of the curve at 47 pb^{-1} . However, this method greatly overestimates the effect of the damage due to the fact that it integrates the loss of signal over the entire length of the lead glass bar, whereas photons from electromagnetic showers are generated most likely at positions closer to the shower maximum, which is 10-20 cm closer to the PMT. Again, the damage itself is distributed along the length of the lead glass according to the longitudinal shower profile; a fact verified by visual inspection of the damage from previous years.

At the end of the longitudinal p+p running, but before the beginning of the pAu running, it was determined that the effective loss of trigger rate in the FMS (for fixed energy thresholds) was approximately 50-70% in the worse areas, closest to the beamline. This corresponded to a change of gain in these cells of about 10-20%. For the p-Au running, this we increased the voltages in this region by approximately 1-2% in order to correct for the change in gain and the reduction in trigger rate. All indications are that the trigger rate/gain has been completely restored and that there is only a small effect (thus far) on the resolution of the pion mass peak, estimated at an increase of about 5% (absolute). Overall, we find that the loss of gain for real photon events is only about half of the gain loss seen for the LEDs.

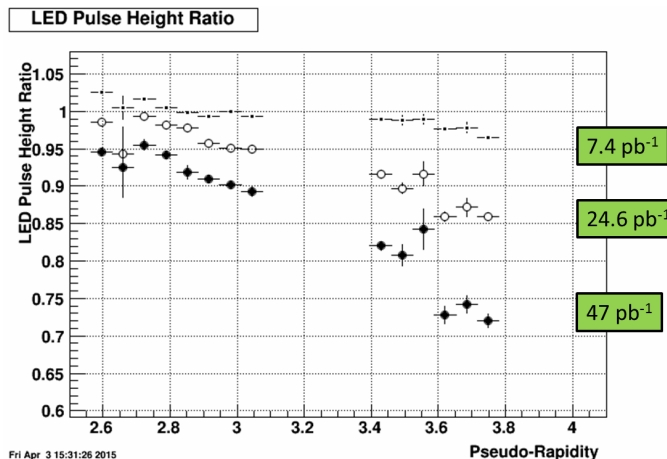


Figure 7–10: loss of gain in the FMS lead glass, as monitored by the LED system, as a function of pseudorapidity for three different integrated luminosity values.

We are currently developing a method to cure the radiation damage due to the beam on the FMS *in situ* using a bank of high intensity LEDs. We have studied the cure rate as a function of LED wavelength, which is complicated by the fact that the transmission coefficient or transparency of the glass is a strong function of wavelength, especially in the region of the photo-multiplier tube response maximum (~380-420 nm).

Figure 7-11 shows spectroscopic measurements of transmission through the glass for the small cells, as an example, both heavily damaged by radiation and at several doses of a UV cure using sunlight. We see, then that the glass is essentially opaque to wavelengths below approximately 350 nm. Three further considerations are the expense, optical efficiency of LEDs and curing efficiency in this region. General, the cost of LEDs rises dramatically below 390 nm, while the optical efficiency falls strongly below about 410 nm. Although the optical efficiency is lower for shorter wavelengths, this means that the waste heat is generated in the LED itself and can be removed by a suitably designed heat exchanger, rather than be dumped in the Lead Glass. We find experimentally that the efficiency of curing rises strongly with shorter and shorter wavelengths. We have performed tests in which we clear radiation damaged lead glass cells by shining light in one end of the (mylar-wrapped) cell and measure the transmission intensity at the other end. In

Figure 7-12 we show the relative transmission of UV light for 3 different wavelengths in the region of interest as a function of time for a family of LEDs with similar characteristics and a nominal power of 40 Watts. We see that the shorter the wavelength, the more rapidly we clear the glass. In Figure 7-13, we give photos of a typically damaged small lead glass cell both before and after curing by means of UV LEDs. The final decision on the exact wavelength LED to use will be based on calculations of the cost, availability and design of the power supply system.

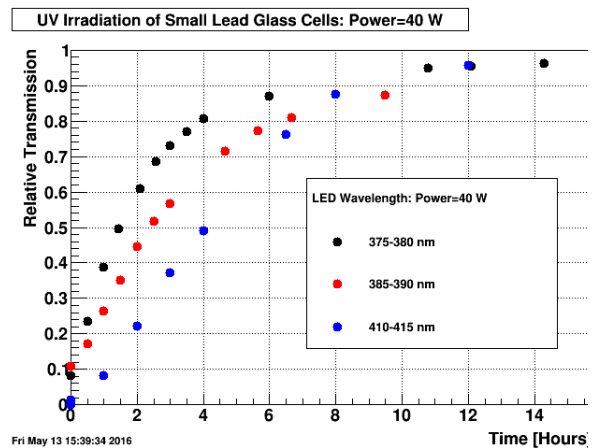
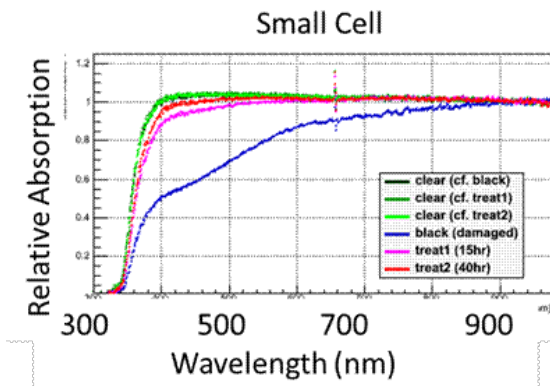


Figure 7-11: Spectroscopic measurements of transmission through the glass for the small cells, as an example, both heavily damaged by radiation and at several doses of a UV cure using sunlight.

Figure 7-12: Relative transmission of UV light for 3 different wavelengths in the region of interest as a function of time for a family of LEDs with similar characteristics and a nominal power of 40 Watts.



Figure 7–13: Photos of a typically damaged small lead glass cell both before and after curing by means of UV LEDs

The final design will require approximately 1000-3000, 10W LEDs in a water-cooled array which tapers in intensity to match the observed radiation damage as a function of distance from the beamline as described above. Much of the physical construction and testing will be performed by undergraduate students at Penn State University (Steve Heppelmann’s Group). The PSU group has volunteered engineering student labor to help in the design and construction of the water-cooled plate, and operation of the remote power supplies. We would also require some investment and manpower from CAD in installing an extra ~ 30 kW of power to supply the LEDs. It is estimated that the current Modified Chilled Water system would be sufficient to remove the waste heat. This installation commissioning would be performed during the summer shutdown in 2016 and be operational in the Fall of 2016.

7.2 Upgrades critical to BES-II

7.2.1 STAR Inner TPC Sector Upgrade (iTPC)

We propose to upgrade the inner sectors of the STAR TPC to increase the segmentation on the inner padplane and to renew the inner sector wire chambers. These two improvements will extend the capabilities of the TPC in many ways. Most significantly, the enhanced tracking at small angles relative to the beamline will expand the TPC’s acceptance out to pseudo-rapidity $|\eta| \leq 1.5$, compared to the current limitation of $|\eta| \leq 1$. Furthermore, the detector will have better acceptance for tracks with low momentum, as well as better resolution in both momentum and dE/dx for tracks of all momenta. These changes will enable the collection of data that is critical to the physics mission for Phase-II of the Beam Energy Scan (BES-II). In addition, the improved dE/dx and momentum resolution, as well as tracking at higher pseudorapidity, provide the foundation for another proposed upgrade - the endcap time of flight project (endcap-TOF) by the STAR/CBM collaboration.

The enhanced performance resulting from the iTPC project will be critical for making the measurements needed to fully address the physics questions which form the basis for the BES-II program. This brief summary will discuss only two topics: (i) using net-proton kurtosis measurements in the search for a critical point in the QCD phase diagram, and (ii) using low mass dielectron pairs to explore the modification of vector mesons in connection with the approach to chiral symmetry restoration in a dense medium. The critical point, if it exists, will provide a landmark in the phase diagram of nuclear matter and guide further experimental and theoretical studies of QCD over a wide range of conditions. The discovery of a QCD critical point would constitute a significant scientific achievement in heavy ion

physics. In addition, characterization of how the system approaches chiral symmetry restoration in dense systems will greatly enhance our understanding of QCD in these environments. As detailed in the STAR BES-II White Paper, the QCD Town Meeting Summary Report, and the Hot QCD White Paper, results from Phase-I of the beam energy scan show provocative results calling for further investigation with greater statistics and increased rapidity coverage.

While the increased data sample provided by BES-II will improve on the quality of current measurements, only the enhanced capabilities provided by the iTPC upgrade will allow a full study of observables which are sensitive to changes in correlation length near the critical point. For example, in the vicinity of a critical point, the net-proton kurtosis is expected to rise as the fourth power of the size of the rapidity window but then saturate as the window becomes comparable to, or larger than, the correlation length in the system. Existing BES-I data exhibit interesting energy trends that suffer from limited statistics and the signal only appears near the edge of the current STAR rapidity acceptance (Δy). The iTPC improvements will allow the fullest possible coverage of the collision region to establish the existence of a rapid rise in the kurtosis signal and, if found, to more fully map out its properties.

In the area of low mass dielectron measurements, the iTPC upgrade improves the acceptance of the detector but also reduces the hadron contamination which is responsible for and is the dominant source of systematic uncertainties in previous measurements. The reduction in uncertainty made possible by the iTPC project will allow the full exploitation of the increased statistics to be collected during BES-II. Full characterization of any meson broadening, and distinguishing between competing theoretical interpretations for a quantitative assessment of how the system approaches chiral symmetry restoration, will only be possible with these improvements.

The costs for the upgrade project will be shared by the US DOE and the Chinese NSF. The DOE project costs are mainly for the design and fabrication of the new sectors, for the design and fabrication of compatible electronics, and for the design and fabrication of the installation tooling. The in-kind contributions from China will focus on the construction of the MWPCs which will be mated to the sector strongbacks in China. The iTPC project proposes to do conceptual design studies in FY2015, sector and MWPC production in FY2016-FY2018, with final installation in FY2018. Following this schedule, the iTPC would be ready to take data during RHIC Run-19. Current RHIC long-range planning calls for the STAR BES II program to take measurements during Run 19 and Run 20.

7.2.2 Event Plane Detector

We propose [90] to construct a new, dedicated Event Plane, centrality, and trigger Detector (EPD) in the forward direction of STAR for the Beam Energy Scan (BES) phase II, anticipated for years 2018-2020. The new detector will cover the pseudo-rapidity range between 2.1 and 5.1, with high radial and azimuthal segmentation. The EPD will allow the centrality and the event plane to be measured in the forward region, reducing the systematics due to autocorrelations from mid-rapidity analyses. The baseline detector design utilizes scintillator plastic, wavelength-shifting fibers and silicon photomultipliers (SiPMs).

The construction budget request is \$242k plus \$45k for new QT boards. These figures include overhead. There have been several prototypes already built and tested for the EPD. The "pre-prototype" was installed for run 15, with the goal of insuring that we could integrate

with the STAR electronics and to test the basic design principals. This test was very successful. Our "prototype" is currently in STAR, taking data during run 16. The goal of the prototype was to build one sector of the EPD and to test it, in order to insure we have the performance necessary to meet the detector requirements. The details of the procedure for the construction of the prototype were also tested, and this informed many of the decisions made that are outlined in this proposal.

The EPD consists of two disks that will be placed on either side of the STAR interaction region, in the current location of the Beam-Beam Counter (BBC). We will install 1/4 of one of the disks for run 17 for detector commissioning. The remaining 7/8 of the detector will be built and installed for run 18.

7.2.3 Endcap TOF (CBM TOF)

The STAR Collaboration and institutions from the CBM Collaboration: Heidelberg, Darmstadt, Tsinghua, CCNU, and USTC propose to install an endcap time-of-flight upgrade (eTOF) to the STAR detector for the BES-II program in 2019 and 2020. The BES-II program will cover collision energies ranging from 3.0 to 19.6 GeV. This is the region of interest in the search for a critical point and first-order phase transition, identified by the results from BES-I and by model calculations. For the collider-mode program (energies above 7.7 GeV), eTOF will extend particle identification (PID) for pions, kaons, and protons to a rapidity of 1.2 compared to the current rapidity coverage extending only 0.8. As such the eTOF will complement the iTPC upgrade. The eTOF upgrade will enable precision studies of key bulk property observables, essential to the BES-II search. For the internal fixed-target program, eTOF will extend the range of collision energies from 7.7 down to 4.5 GeV, without which there would be a large energy gap in the BES-II program.

8 References

- 1 STAR Beam Energy Scan II: Studying the Phase Diagram of QCD Matter at RHIC
<https://drupal.star.bnl.gov/STAR/starnotes/public/sn0598>
- 2 B. Trzeciak for the STAR Collaboration, QM2015, e-Print Archives (1512.07405)
- 3 J.P. Lansberg, J.Phys. G 38 (2011) 124110
- 4 N. Brambilla et al., Eur. Phys. J. C 71 (2011) 1534
- 5 Shuai Yang (for the STAR Collaboration), Quark Matter 2015
- 6 B. Ling and M. Stephanov, Phys.Rev. C 93 (2016) 034915
- 7 G. Bunce *et al.*, Phys. Rev. Lett. 36. 1113 (1976)
- 8 K. J. Heller *et al.*, Phys. Rev. Lett. 51, 2025 (1983)
- 9 Z.-T. Liang and X.-N. Wang, Phys. Rev. Lett. 94, 102301 (2005), [Erratum: Phys. Rev. Lett.96,039901(2006)].
- 10 S. A. Voloshin, (2004), arXiv:nucl-th/0410089
- 11 J.-H. Gao, S.-W. Chen, W.-t. Deng, Z.-T. Liang, Q. Wang, and X.-N. Wang, Phys. Rev. C77, 044902 (2008), arXiv:0710.2943 [nucl-th]
- 12 L. P. Csernai, D. D. Strottman, and C. Anderlik, Phys. Rev. C85, 054901 (2012), arXiv:1112.4287 [nucl-th]
- 13 L. P. Csernai, D. D. Strottman, and C. Anderlik, Phys. Rev. C85, 054901 (2012), arXiv:1112.4287 [nucl-th]
- 14 L. P. Csernai, D. D. Strottman, and C. Anderlik, Phys. Rev. C85, 054901 (2012), arXiv:1112.4287 [nucl-th]
- 15 Y. Jiang, Z.-W. Lin, and J. Liao, (2016), arXiv:1602.06580 [hep-ph]
- 16 L. D. Landau and E. M. Lifshits, Statistical Physics (Pergamon Press, 1969); A. Vilenkin, Phys. Rev. D21, 2260 (1980); F. Becattini and F. Piccinini, Annals Phys. 323, 2452 (2008), arXiv:0710.5694 [nucl-th]
- 17 STAR Collaboration, L. Adamczyk et al., Phys.Rev.Lett. 116 (2016) no.13, 132301.
- 18 Z.-B. Kang and J.-W. Qiu, Phys. Rev. Lett. 103 (2009) 172001.
- 19 STAR Collaboration, L. Adamczyk *et al.*, Phys. Rev. Lett. 115 (2015) 242501.
- 20 D. Boer, A. Dumitru, A. Hayashigaki, Phys. Rev. D74(2006) 074018
D. Boer and A. Dumitru, Phys. Lett. B556 (2003) 33.
D. Boer, A. Utermann, and E. Wessels Phys. Lett. B671(2009) 91.
Z.-B. Kang and F. Yuan, Phys. Rev. D84 (2011) 034019.
Y.V. Kovchegov and M.D. Sievert, Phys. Rev. D86 (2012) 034028.
- 21 J.-W. Qiu, talk at “Forward Physics at RHIC” workshop, RIKEN BNL Research Center, BNL, 2012.
- 22 STAR Collaboration, L. Adamczyk *et al.*, Phys. Rev. Lett. 115 (2015) 092002.
- 23 D. Kharzeev, Phys. Lett. B 633, 260 (2006) [hep-ph/0406125].
- 24 D. Kharzeev and A. Zhitnitsky, Nucl. Phys. A 797,67 (2007).
- 25 D. E. Kharzeev, L. D. McLerran and H. J. Warringa, Nucl. Phys. A 803, 227 (2008) [arXiv:0711.0950 [hep-ph]].
- 26 S. A. Voloshin, Phys. Rev. C 70, 057901 (2004) [hep-ph/0406311].
- 27 STAR Collaboration, B. I. Abelev *et al.*, Phys. Rev. Lett. 103, 251601 (2009).
- 28 STAR Collaboration, B. I. Abelev *et al.*, Phys. Rev. C 81, 54908 (2010).
- 29 STAR Collaboration, L. Adamczyk *et al.*, Phys. Rev. C 88 (2013) 064911.
- 30 STAR Collaboration, L. Adamczyk *et al.*, Phys. Rev. Lett. 113 (2014) 052302.

-
- 31 ALICE Collaboration, B. I. Abelev *et al.*, Phys. Rev. Lett. 110 021301 (2013).
- 32 A. Bzdak, V. Koch and J. Liao, Lect. Notes Phys. 871 503 (2013) [arXiv:1207.7327 [nucl-th]].
- 33 STAR Collaboration, L. Adamczyk *et al.*, Phys. Rev. Lett. 115, (2015), 222301.
- 34 P. Tribedy, Workshop on Chirality, Vorticity and Magnetic Field in Heavy Ion Collisions, 2016;
http://starmeeetings.physics.ucla.edu/sites/default/files/pritwish_tribedy.pdf.
- 35 D. T. Son and A. R. Zhitnitsky, Phys. Rev. D 70, 074018 (2004).
- 36 M. A. Metlitski and A. R. Zhitnitsky, Phys. Rev. D 72, 045011 (2005).
- 37 Y. Burnier, D. Kharzeev, J. Liao and H. Yee, Phys. Rev. Lett. 107 (2011) 052303.
- 38 S.A. Bass *et al.*, Prog. Part. Nucl. Phys. 41, 225 (1998); M. Bleicher *et al.*, J. Phys. G: Nucl. Part. Phys. 25, 1859 (1999).
- 39 Z.W. Lin and C.M. Ko, Phys. Rev. C 65, 034904 (2002); L.-W. Chen, C.-M. Ko, J. Phys. G 31, S49 (2005).
- 40 Y. Burnier, D.E. Kharzeev, J. Liao, H.-U. Yee, arXiv: 1208.2537 (2012); private communication.
- 41 Q.-Y. Shou, Nucl. Phys. A 931 (2014) 758.
- 42 D. E. Kharzeev and D. T. Son, Phys. Rev. Lett. 106 (2011) 062301.
- 43 Feng Zhao, Nucl. Phys. A 931 (2014) 746.
- 44 H1 Collaboration, F. Aaron *et al.*. JHEP, 01:109, 2010. arXiv:0911.0884.
- 45 A. V. Efremov and O. V. Teryaev, Sov. J. Nucl. Phys. 36, 140 (1982) [Yad. Fiz. 36, 242 (1982)];
Phys. Lett. B 150, 383 (1985).
J.-W. Qiu and G. F. Sterman, Phys. Rev. Lett. 67, 2264 (1991); Nucl. Phys. B 378, 52 (1992);
Phys. Rev. D 59, 014004 (1999)
- 46 L. Gamberg, Z.-B. Kang, and A. Prokudin, Phys. Rev. Lett. 110 (2013) 232301.
- 47 L. Gamberg, Z.-B. Kang, and A. Prokudin, Phys. Rev. Lett. 110 (2013) 232301.
- 48 J.C. Collins, arXiv:1409.5408.
- 49 J.C. Collins and T. Rogers, Phys.Rev. D91 (2015) 074020.
- 50 P. Sun and F. Yuan, Phys. Rev. D88 (2013) 114012.
- 51 P. Sun, J. Isaacson, C.-P. Yuan and F. Yuan arXiv:1406.3073.
- 52 M.G. Echevarria, A. Idilbi, Z.-B. Kang and I. Vitev, Phys. Rev. D89 (2014) 074013.
- 53 Z.-B. Kang, A. Prokudin, F. Ringer, F. Yuan, et.al., to be submitted for publication, 2016
- 54 M. Anselmino, M. Boglione, U. D'Alesio, J.O. Gonzalez Hernandez, S. Melis, F. Murgia
and A. Prokudin, Phys. Rev. D 92 (2015) 114023.
- 55 E.A. Hawker et al., Phys. Rev. Lett. 80, 3715 (1998)
- 56 Z.-B. Kang and J.-W. Qiu, Phys.Rev.D81:054020,2010, arXiv:0912.1319
- 57 L. Gamberg, Z.-B. Kang, and A. Prokudin, Phys. Rev. Lett. 110 (2013) 232301.
- 58 H. Beppu, K. Kanazawa, Y.Koike and S.Yoshida, Phys. Rev. D89 (2014) 034029;
D. Boer, C. Lorcé, C. Pisano and J. Zhou, Adv. High Energy Phys. 2015 (2015) 371396.
- 59 L.C. Bland et al. [AnDY Collaboration], Phys.Lett. B750 (2015) 660.

-
- 60 D. Mueller, D. Robaschik, B. Geyer, F.-M. Dittes and J. Hoeji, Fortschr. Phys. 42 (1994) 101;
X.-D. Ji, Phys. Rev. Lett. 78 (1997) 610; J. Phys. G24 (1998) 1181;
A.V. Radyushkin, Phys.Lett. B380 (1996) 417;
M. Burkardt, Phys.Rev. D62 (2000) 071503; Erratum-ibid. D66 (2002) 119903.
- 61 S. Klein and J. Nystrand, hep-ph/0310223.
- 62 T. Toll and T. Ullrich, Phys.Rev. C 87 (2013) 024913.
- 63 S. Kretzer, Phys. Rev. D 62, 054001 (2000);
B.A. Kniehl, G. Kramer, and B. Potter, Nucl. Phys. B582, 514 (2000);
S. Albino, B.A. Kniehl, and G. Kramer, Nucl. Phys. B725, 181 (2005);
M. Hirai, S. Kumano, T.-H. Nagai, and K. Sudoh, Phys. Rev. D 75, 094009 (2007).
- 64 D. de Florian, R. Sassot, and M. Stratmann, Phys. Rev. D 75, 114010 (2007);
D. de Florian, R. Sassot, and M. Stratmann, Phys. Rev. D 76, 074033 (2007).
- 65 T. Kaufmann, A. Mukherjee, and W. Vogelsang, Phys. Rev. D 92, 054015 (2015).
- 66 D. de Florian, R. Sassot, M. Epele, R.J. Hernandez-Pinto, and M. Stratmann, Phys. Rev. D 91, 014035 (2015).
- 67 STAR Collaboration L. Adamczyk et al. Phys. Rev. D85 092010 (2012).
- 68 UKQCD Collaboration, Phys. Rev. D82 034501 (2010)
- 69 W. Ochs, J. Phys. G40 043001 (2013).
- 70 F. Close and A. Kirk, Phys. Lett. B333 (1997)
- 71 K. Burke et al, [JET Collaboration], Phys. Rev. C 90 1 (2014) 014909.
- 72 Phys. Rev. Lett. 98:172301 (2007)
- 73 PHENIX 62 GeV NPE results
- 74 Min He, Rainer J. Fries, and Ralf Rapp. Phys. Rev. C 91 (2015) 024904.
- 75 M. M. Aggarwal et al. Phys. Rev. C 83, (2011) 024901
- 76 Phys. Rev. D 79, 034009 (2009); arXiv:1410.3959
- 77 H.van Hees, M. He, Ra. Rapp, Nuclear Physics A 933 (2015) 256.
- 78 S. Voloshin, Phys. Rev. Lett. 105 (2010) 172301.
- 79 B.B. Back et al., Phys. Rev. C 65, 031901(R) (2002); K. Adcox et al., Phys. Rev. Lett 86, 3500 (2001); I.G. Bearden et al., Phys. Lett. B 523, 227 (2001); J. Adams et al. (STAR Collaboration), nucl-ex/0311017.
- 80 B. Pritychenko, M. Birch, B. Singh, and M. Horoi, arXiv:1312.5975 [nucl-Th] (2013); S. Raman, C. W. Nestor Jr., and P. Tikkanen, Atomic Data and Nuclear Data Tables 78, 1 (2001).
- 81 P. Moller, J.R. Nix, W.D. Myers and W.J Swiatechi, Atomic Data and Nuclear Data Tables 59, 185 (1995).
- 82 W. -T. Deng and X. -G. Huang, Phys. Rev. C 85 (2012) 044907; W. -T. Deng and X. -G. Huang, Phys. Lett. B 742 (2015) 296; private communication.
- 83 S. Yang, Ph.D. thesis, University of Science and Technology of China, 2016.
- 84 STAR Collaboration, B. I. Abelev et al., Phys. Rev. Lett. 102, 1122301 (2009).
- 85 STAR Collaboration, J. Adams et al., Phys. Rev. C 70, 031902 (R) (2004).
- 86 ALICE Collaboration, J. Adams et al., arXiv:1509.08802.
- 87 P. Tribedy, private communications, S. Chatterjee and P. Tribedy, Phys. Rev. C 92, 1, 011902 (2015)
- 88 D. E. Kharzeev, L. D. McLerran, and H. J. Warringa, Nucl. Phys. A803, 227 (2008), arXiv:0711.0950 [hep-ph];

V. Skokov, A. Yu. Illarionov, and V. Toneev, *Int. J. Mod. Phys. A*24, 5925 (2009),
arXiv:0907.1396 [nucl-th];
V. Voronyuk, V. D. Toneev, W. Cassing, E. L. Bratkovskaya, V. P. Konchakovski, and S. A.
Voloshin, *Phys. Rev. C*83, 054911 (2011), arXiv:1103.4239 [nucl-th];
U. Gursoy, D. Kharzeev, and K. Rajagopal, *Phys. Rev. C*89, 054905 (2014), arXiv:1401.3805
[hep-ph];
K. Tuchin, *Int. J. Mod. Phys. E*23, 1430001 (2014)
89 L. McLerran and V. Skokov, *Nucl. Phys. A*929, 184 (2014), arXiv:1305.0774 [hep-ph]
90 Proposal for an Event-Plane Detector
https://drupal.star.bnl.gov/STAR/system/files/EPD_Construction_Proposal.pdf